Part III

Detectors

Chapter 9

Detector overview

Chapter 10

Interaction Region

10.1 Introduction

In this chapter we examine various aspects of experimentation that directly interacts with the accelerator design. Of particular concern in this area is the background to the physics experiments that are caused by the beams passing through the detector.

The characteristics of background events at JLC will be very different from those at typical e^+e^- colliders, except the SLC. The features of the background strongly depend on numerous operational parameters of the accelerator, such as the beam aspect ratio (typically $\sigma_x^*/\sigma_y^* = 0(100)$), a high beam intensity (10^{10}particles/bunch) and possible tails in the particle distribution that deviates from a Gaussian distribution. The population of low energy $e^{\pm}$ pairs that are created during collisions are directly related to the beam aspect ratio, while the tail is mostly responsible for synchrotron radiation and muon background. The optimization of the machine operational parameters must be considered by taking this "interaction" between the experimentation and the machine into account. The highest-priority goal here is, of course, to maximize the luminosity while minimizing the background. With such a motivation in mind, the effects of $e^{\pm}$ pairs have been estimated by detailed Monte Carlo simulations with the proposed JLC-1 detector[1], in addition to simulations of masking of synchrotron radiation and the attenuation of the muon flux that are produced by interactions of the beams with upstream collimator materials.

the "beamstrahlung" phenomenon. Therefore, the effective luminosity at $\sqrt{s} = 2 \times E_{beam}$ is always smaller than the nominal value that does not take beamstrahlung into account. The luminosity spectrum as a function of the center-of-mass energy depends on the magnitude of beamstrahlung. Knowledge on such issues is very important for conducting precision measurements, especially for studies of toponium physics[2] and detailed investigations of SUSY physics[3], which are research opportunities unique to linear colliders. A method based on the measurement of acollinearity angles in Bhabha scattering events is examined as a possible technique to measure the luminosity spectrum.

10.2 Backgrounds

To illustrate where the background particles can originate, the beam line from the exit of the main linear accelerator (linac) to the interaction point (IP) is schematically shown in Figure 10.1. A +7 mrad bending magnet section (200 m long) downstream of the collimation section is needed in order to create a sufficient amount of separation for two experimental halls and to prevent the background from the upstream linac from directly hitting the detector. In the final focus system, beams are gradually deflected so as to have a horizontal beam crossing angle of ± 4 mrad at the interaction point (IP).

There are two major sections for beam collimation (1200 m long) and a final focus system (1800m long) in the beam line to handle beam energies up to 0.75 TeV. While their main purposes are to clip the beam tails, secondary particles are inevitably produced, namely: (1) muons and (2) synchrotron radiation photons, respectively. In addition at the IP, (3) e^+e^- pairs and (4) mini-jet are created through beam-beam interactions. They all cause background hits in the detector facility.

In subsequent sections the first three kinds of background are discussed together with a possible design of the interaction region.

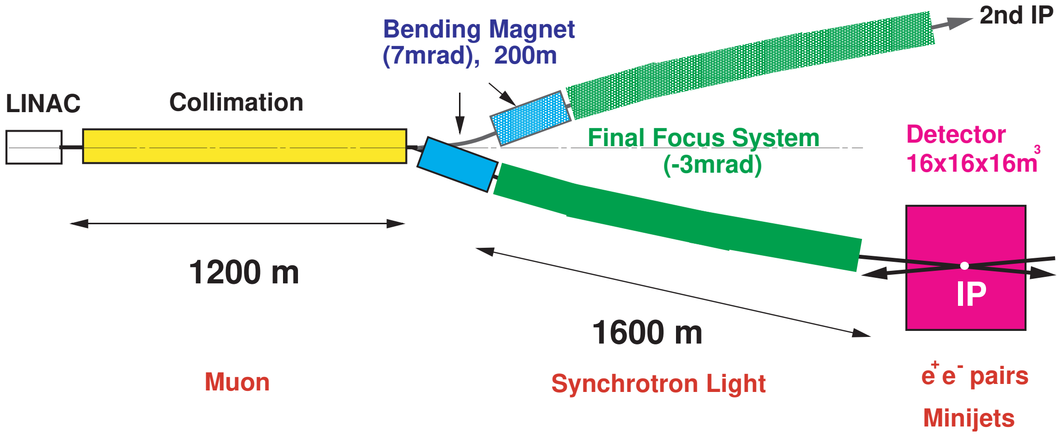

Figure 10.1: Top view of the beam line from the exit of the main linac to the interaction point (IP) at $E_{cm} = 0.5 - 1.5$ TeV.

10.2.1 Collimation and Muons

In this section we discuss the production of muons through the interaction of particles in the beam tails when they are collimated at the upstream collimation sections.

Generally, the transverse profile of the beam does not exactly follow a Gaussian distribution at linear colliders. The beams can be accompanied by long tails according to experience from experiments at SLC [7]. While the origin of these tails is not thoroughly understood at present, we shall conservatively assume that the beam has a flat tail beyond $\pm 3\sigma_{x(y)}$ in both the horizontal(x) and vertical(y) directions with a relative intensity of $0.1 \sim 1\%$.

The beam must be collimated within $\pm 6\sigma_x$ and $\pm 40\sigma_y$ in order to keep the background due to synchrotron radiation at a manageable level. Since the typical size of the beam core is on the order of a few μm, collimating such beams is a seriously non-trivial task. A work-around is to expand only the tail part sufficiently by using a non-linear collimation technique, as discussed in Chapter 13. This is part of the reason why a 1200 m-long collimator section is required for collimating a 0.75 TeV beam.

One RF pulse will accelerate a bunch train which contains up to 95 bunches separated by 2.8 nsec at a repetition rate of 150Hz. Since each bunch consists of 7.5×10^9 electrons (or positrons) at the IP, about 10^8(1%tail)$\times 10^2$(bunches) electrons may hit collimators at 150 Hz. In the interactions of the beam tails with the collimators a large number of muons are produced through the Bethe-Heitler process, $e^{\pm}N \rightarrow e^{\pm}\mu^+\mu^-N$. Without suitable measures these muons would traverse through the tunnel and create a large amount energy deposit within the detector facility. They would cause serious background problems for conducting high-energy physics experiments.

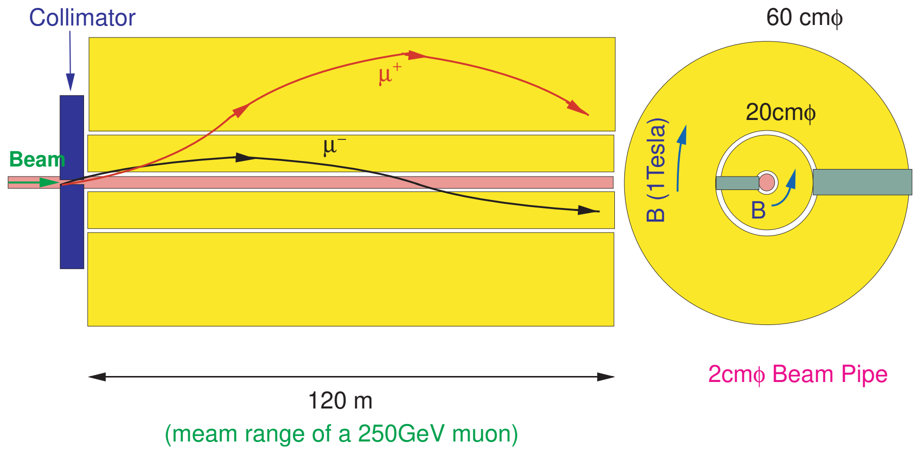

Figure 10.2: Original idea of a muon attenuator. Two iron pipes are magnetized axially in opposite directions for both charged muons, which can be trapped, where the 120m length of the iron pipe corresponds to a mean range of 250GeV muons.

There are eight collimators upstream of the big bend, which are located at 1840.3 $\sim$ 2855.6 m from IP as shown in Fig.10.3 (a). Two of them (col.-1 and -2) are set in the linac. They doubly collimate the beams in momentum space($\Delta p/p < \pm 2\%$) and phase space of transverse profile and divergence ($6\sigma_x^{(\prime)} \times 40\sigma_y^{(\prime)}$). During the collimation, a lot of secondary particles would be produced. Among them high energy muons would create the most severe backgrounds. A rate of muons depends on a population in a tail of beam. For the conservative estimation, we assume that the tail is 0.1 $\sim$ 1% of the bunch population for this simulation study.

In the simulation muons were tracked down to the detector of $16 \times 16 \times 16\mathrm{m}^3$ with various configurations of muon attenuation in a tunnel. The present simulation does not take account of optical elements except for bending magnets (Fig.10.3(a)) at the beam line. The muon attenuator is a magnetized iron cylinder of $1 < r < 30$cm, which actually comprizes two cylinders of $1 < r < 10$cm (inner) and $10 < r < 30$cm (outer) as shown in Fig. 10.2. The axis of cylinders corresponds to the beam line. The two cylinders are magnetized circularly in opposite directions to confine positive and negative muons in each. The muon attenuator is assumed to cover from the big bend through the whole collimation system, which is 1510 to 2856m from IP. Figure 10.3(b) shows the number of electrons (e/μ) at 8 collimators to produce one muon in the detector [9]. Open arrows indicate the lower limits since no muon was observed within the simulation statistics. The best configuration (solid triangles) was the muon attenuator magnetized at 10KG to confine positive muons (10 KG, μ^+ inside) in the inner cylinder, where the beam particles were 250GeV electrons. It attenuates muons by 4 order of magnitudes more than a case with no muon-shield (open circles). The oppositely magnetized attenuator(open triangles, 10 KG, μ^- inside) has less shielding power than the best case for col.6-8 since the negative muons can be transported to the detector in the same way as the beam. The magnetization effect is clearly seen by comparing them with the no magnetized attenuator (solid circles, 0 KG). With the best configuration and the $0.1 \sim 1\%$ beam tail, a few muons would hit the detectors per pulse for the pulse population of $(0.71 \sim 1.33) \times 10^{12}$ corresponding to A∼Y in Table ??. In this case the muons should not be a serious background.

(a)

element	distance from IP:m	function
bend1	90	-3.28mrad
bend2 (big bend)	1600	7 mrad
col.-8	1840.3	x',y' 2nd col.
col.-7	1966.7	x',y' 1st col.
col.-6	2093,1	x,y 2nd col.
col.-5	2219.5	x,y 1st col.
col.-4	2357.4	p 2nd col.
col.-3	2483.9	p 1st col.
col.-2	2725.4	(in the linac)
col.-1	2855.6	(in the linac)

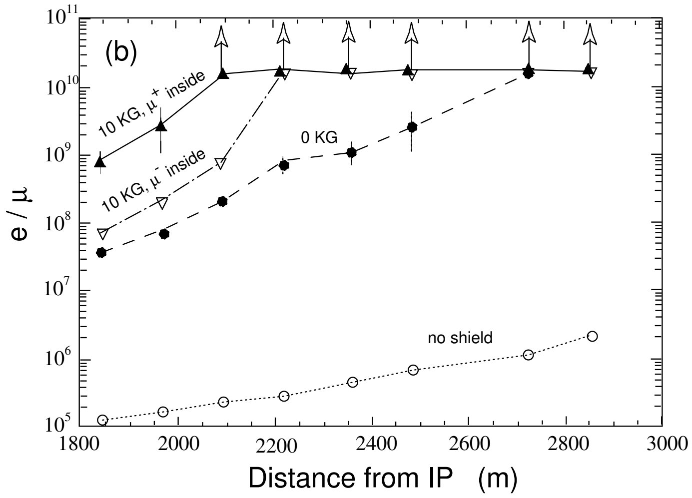

Figure 10.3: (a) Locations of bending magnets and collimators in the beam delivery system. (b) The number of collimated electrons (positrons), which give one muon in a detector of $16 \times 16 \times 16\mathrm{m}^3$, at eight collimators. Open circles are simulation results with no muon shield, and the others are those with muon attenuators at 1510∼2856m from IP (Y. Namito, Jan.1999).

10.2.2 Synchrotron Radiation

Since the intensity of synchrotron radiation is on the same order as the intensity of the beam, itself, it would be very harmful to the experimentation if they are scattered at the pole tips of the nearest quadrupole magnet QC1. It is also very difficult to shield them near to the IP. The amount of synchrotron radiation is determined by the maximum size and angular divergence of the beam profile. Both the maximum beam size (x, y) and the divergence (x', y') shall be well defined and controlled by the collimators.

The divergences can be expressed by $\sigma_{\theta_{x(y)}} = \sqrt{\epsilon_{x(y)}/\beta_{x(y)}}$, where $\beta_{x(y)}$ is a (optical) beta function in the final focus system and $\epsilon_{x(y)}$ is an emittance of beams. The beam size and the divergence are related by $\epsilon_{x(y)} = \sigma_{\theta_{x(y)}} \cdot \sigma_{x(y)}$. If we can not control them by some means, we must change the optics to enlarge $\beta_{x(y)}$ so that $\sigma_{\theta_{x(y)}}$ decreases. We may thus even have to sacrifice the luminosity because of $\sigma_{x(y)} = \sqrt{\epsilon_{x(y)} \cdot \beta_{x(y)}}$. A similar situation would likely occur at the beginning of operation with a larger emittance than the expected one, as happened in the SLC experiments.

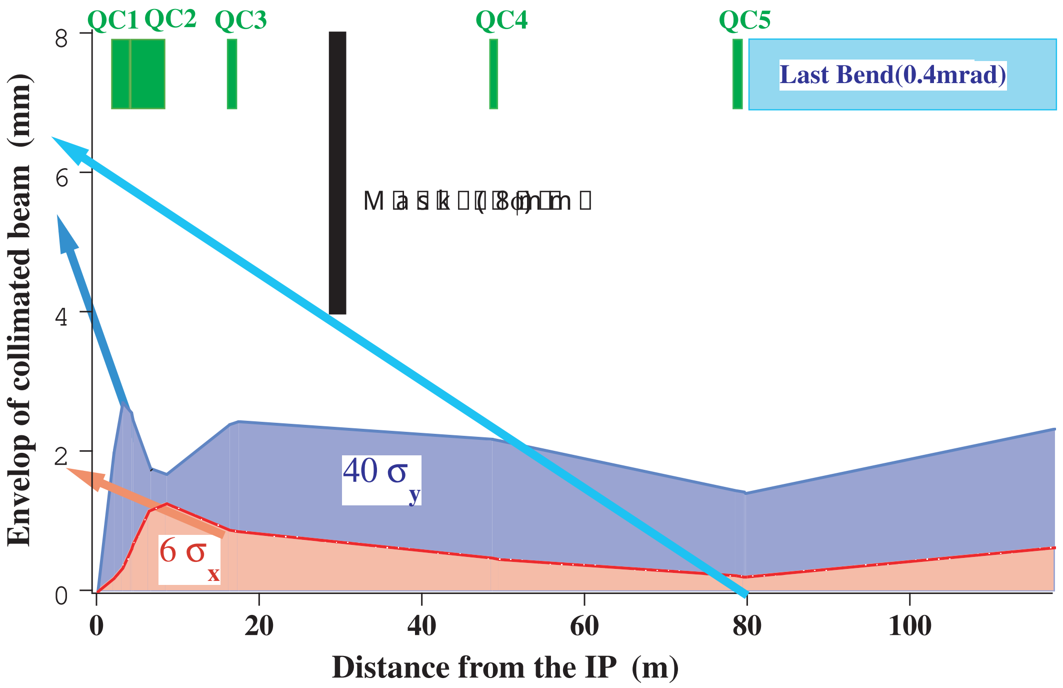

Figure 10.4: Horizontal($6\sigma_x$) and vertical($40\sigma_y$) beam envelopes through the last bending magnet and five final focus quadrupole magnets(QC1,QC2,QC3,QC4 and QC5). The maximum divergences of the synchrotron radiation are also drawn by arrows.

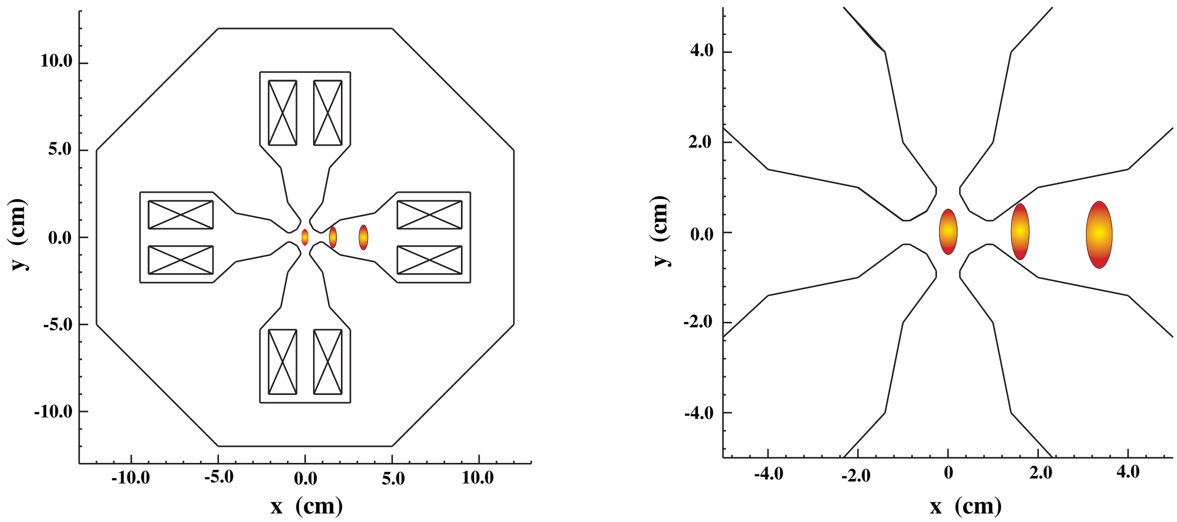

Figure 10.5: Profiles of the synchrotron radiation at QC1;right figure shows the magnified view around the center of QC1. The profile at the center accompanies the in-coming beam. The two right-hand side ones are passing through QC1 of 2.2m long after a collision with a 8mrad horizontal crossing.

Figure 10.4 shows the development of transverse beam envelops that correspond to $6\sigma_x \times 40\sigma_y$. Figure 10.4 covers the region from the IP up to the nearest dipole bend magnet. Here the smearing effect due to collimation is not taken into account, since it was estimated to be very small(10^{-8}) as mentioned earlier.

With a mask of 8 mmϕ radial aperture that is located at 30 m from the IP, synchrotron radiation from upstream magnets beyond the last bending magnet can be completely masked. Any synchrotron radiation that passes through the aperture of 8 mmϕ mask would pass through the final quadrupole magnet (QC1) without scattering. The half aperture of QC1 is chosen to be 6.85 mm. As can be clearly seen in Figure 10.4, the radiation from QC3 and QC2 provides the maximum divergence at the IP in the horizontal and vertical directions, respectively. The profiles of the radiation at the QC1 are shown in Figure 10.2.2. The length and inner aperture of QC1 are 2. 2m and 13.7 mmϕ, respectively. The front face of QC1 is located 2.0 m from the IP. The in-coming radiation passes through the central axis of QC1. After colliding with the opposing beam at a horizontal crossing angle of 8 mrad, the out-going radiation passes off-axis through the QC1 magnet on the other side. The location of the out-going radiation is depicted as two elliptic profiles on the right-hand side of Figure 10.2.2.

As described above, it is expected that there should be no background problems due to the synchrotron radiation if we carefully optimize the collimation and the optics simultaneously.

10.2.3 e^+e^- pairs

An enormous amount of e^+e^- pairs will be created during collisions, for instance a few times 10^5 pairs per bunch crossing. While their vast majority are scattered into extremely forward angles, some can be greatly deflected by the strong magnetic field that is produced by the on-coming beam. In such cases they can enter the detector region and can create background noise to the detector facility. Figure 10.2.3 shows the angular distributions of pair-produced electrons and positrons after the beam-beam interaction. The calculation was made using ABEL[11]. Many particles (electrons or positrons) are scattered at large angles exceeding 200 mrad. We can also clearly see an asymmetry in their azimuthal distribution. More particles are deflected in the vertical direction than in the horizontal because of a very flat transverse beam profile ($\sigma_x^*/\sigma_y^* = 260\text{nm}/3.0\text{nm}$). Since the energies of the particles are relatively small, and are at a few hundreds MeV, most of these particles are confined near to the beam axis due to the detector solenoid magnetic field of 2 T. However, when they hit QC1 in the out-going side, many secondary photons are backscattered uniformly into the detector region. They can become serious background.

10.3 Layout

IP layout is shown in Fig.10.7. Nearest final quadrupole magnet (QC1) is located at 2m from IP, where the QC1 is shielded against a solenoid field of 2 Tesla by a superconducting compensation magnet. A huge number of X rays, which are created in electromagnetic showers of $e^\pm$ pairs at QC1, are absorbed in conical and cylindrical tungsten masks. Angular coverage of the conical mask ranges from 0.15 to 0.2 radian, leaving a small dead cone angle, but the front part of the conical mask could be instrumented as a calorimeter.

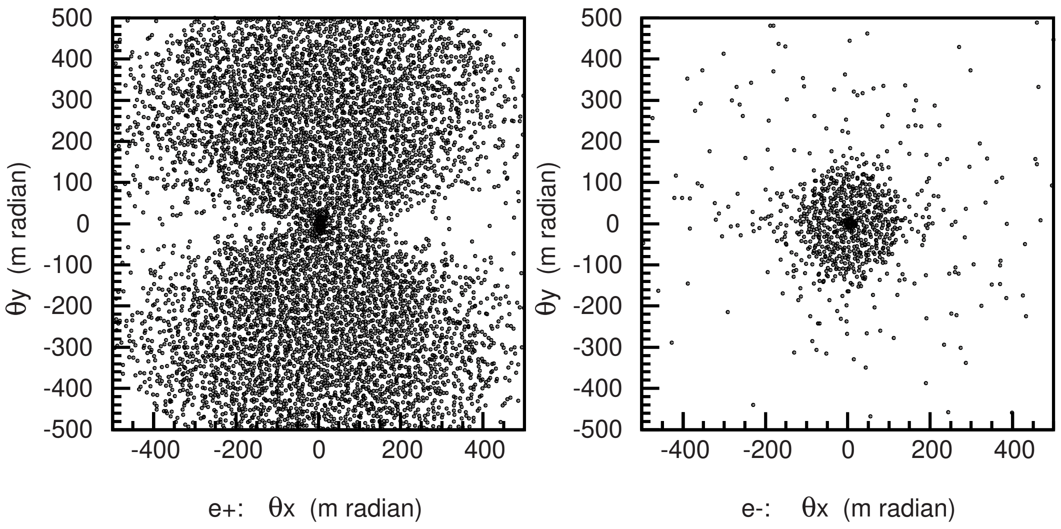

Figure 10.6: Electrons and positrons scattered by beam-beam interaction at IP. The vertical and horizontal axes denote the scattering angles in the vertical and horizontal directions, respectively. The left- and right-hand figures show the distributions of the positrons and electrons, respectively, downstream of the electron beam. Since the positrons have the same sign charge as the in-coming (positron) beam, they are scattered by larger angles than the electrons.

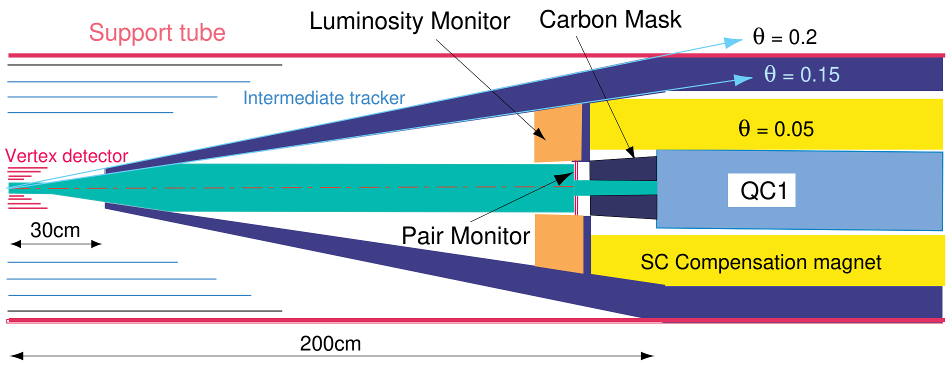

Figure 10.7: Interaction region.

There is the luminosity monitor covering an angular region between 0.05 and 0.15 radian inside the mask. The carbon mask in front of the QC1 is very effective to absorb low energy back-scattered electrons. The 4-layer vertex detector (VTX) is located at radial distance from 2.4 to 6.0cm, followed by an intermediate tracker to link charged tracks between the CDC and the VTX. All these instruments are installed in a support tube of 80cm diameter[12].

The interaction region has been updated since the 1st ACFA-LC (Beijing) workshop[13] in order to further reduce $e^{\pm}$ pair backgrounds in the vertex detector(VTX) and the central drift chamber (CDC), especially X-rays in the CDC. The major changes are in the beam pipes and the locations of the carbon mask and the pair monitor. The beam pipe inside the VTX is made of 0.5mm thick beryllium, 4cm in diameter, while the major part is a 15cm diameter beam pipe of 2mm thick aluminum in the mask. These two beam pipes are connected with a conical beryllium pipe of 2mm thickness. The 15 cm diameter is large enough for $e^{\pm}$ pair particles to curl inside the beam pipe without interactions. The pair monitors consisting of active pixel device are now located at 176cm from IP, i.e. inside of luminosity monitor(50 - 150 mrad). In the previous design, they were closer to IP and were one of the sources of X rays.

10.4 Estimation of background hits

10.4.1 e^+e^- pairs

There is a desire to increase the detector magnetic field (B) from 2 to 3 Tesla. The motivations are to reduce backgrounds and to place a vertex detector closer to beam line as well as to reduce the overall detector size. We study a case of B=3Tesla in terms of backgrounds in two major detectors, which are a central drift chamber (CDC) filled with 1atm CO_2/isobutane (90%/10%) and a CCD vertex detector (VTX) of $25 \times 25\mu\text{m}^2$ pixels. Inner and outer radii of the CDC are 0.45 and 2.3m, respectively, and the length is $\pm$2.3m. The VTX is assumed to be consisted of three layers (r=2.5, 5.0, 7.5 cm and z=$\pm 7.5, 15.0, 22.5$cm, respectively) in this study. Background hits were also simulated with detailed geometries by JIM, where photons and electrons(positrons) are tracked down to their energies of 10keV and 200keV, respectively.

The major backgrounds are secondary photons in the CDC although the CDC is shielded against them by the masks. For an estimation of the photons entering the CDC, we counted the number of photons traversing a surface of 60cmϕ $\times$ $\pm$1m long cylinder. Figure 10.9 shows the results at B=2 and 3 Tesla for 10 bunch crossings. Most of the photons are created by low energy electrons (or positrons) hitting the 4cmϕ beam pipe very near IP . We can see an apparent advantage of higher magnetic field in Fig.10.9 because of stronger confinement of the electrons(positrons) around the beam line at B=3 Tesla. On the other hand, the main backgrounds to VTX are primary electrons(positrons).

Rates of background hits are summarized both at B=2 and 3 Tesla in Table 10.4.1. As mentioned above, the backgrounds hits in CDC are proportional to the numbers of photons, which are one order of magnitude less at B=3 Tesla than those at B=2 Tesla. The CDC hit rates were estimated to be 1210 and 120 hits per a train crossing at B=2 and 3 Tesla, respectively. Assuming that the total number of CDC readout channels is 10000, corresponding occupancy rates are 12 and 1.2 % at B=2 and 3 Tesla, respectively. In the

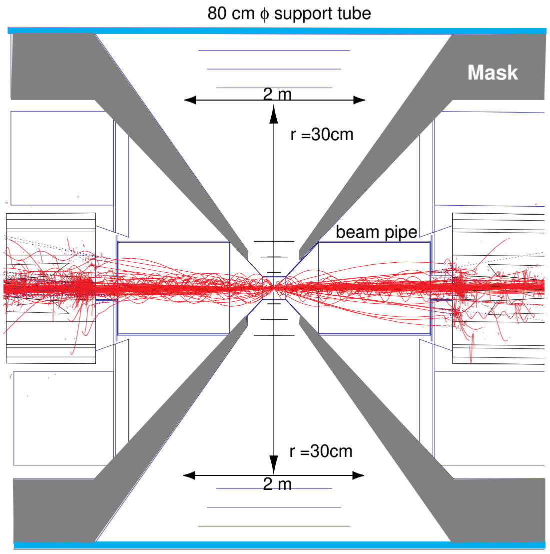

Figure 10.8: Pair samples in the support tube at B=2 Tesla by JIM simulation, where photons of > 100MeV and electrons(positrons) of > 10MeV are only shown for display purpose.

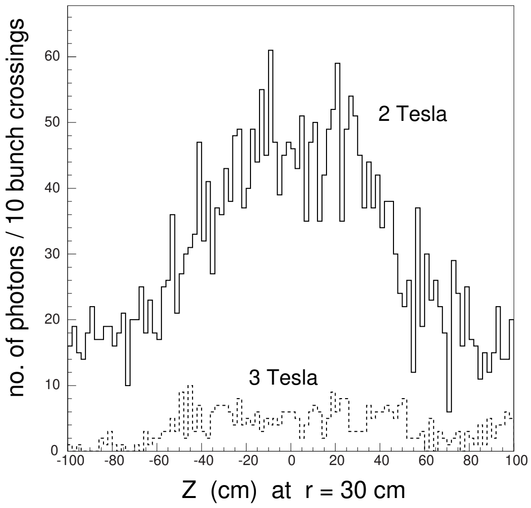

Figure 10.9: Number of photons traversing a cylinder of 60cm$\phi \times \pm$ 100cm long as a function of z at B=2 and 3 Tesla for the CDC background estimation.

VTX the most severe backgrounds were observed at the innermost layer, where the hit densities are estimated to be 0.9 and 0.4 /mm^2/train at B=2 and 3 Tesla, respectively. We also simulated backgrounds for the case of the high luminosity option specified as JLC-Y. The results are also listed in Table 10.4.1. For the JLC-Y, the background rates per bunch crossing increase by 1.3$\sim$3 times because of smaller beam sizes as seen in Table **??**. Doubling the number of bunches per train crossing at the JLC-Y, the CDC occupancy and the VTX hit density can be estimated to be 47 (7.4)% and 2.8(1.0)/mm^2/train, respectively, at B=2 (3) Tesla.

Setting background tolerances for 10% occupancy and 1/mm^2/train hit density in the CDC and VTX, respectively, the backgrounds with B=2 Tesla are marginal at the JLC-A and they may overwhelm the detectors at the luminosity-upgraded JLC-Y. For the case of B=3 Tesla, there seems to be a possibility of placing the VTX closer to the beam line at least for the JLC-A. Therefore two configurations of the VTX and beam pipe have been studied by the JIM simulation. The first comprizes the VTX of 1.5cm minimum radius (r_{vtx1}) and 2cmϕ beam pipe, while the second comprizes the VTX of r_{vtx1}=1.8cm and 3cmϕ beam pipe. Radii of the second and third layer of the VTX are 2.5cm and 5.0cm, respectively, for both configurations. The simulation results are summarized in Table 10.4.1. From the point view of the background tolerances, the second configuration is only allowed for the CDC occupancy of 7.2% and the VTX hit density of 1.6/mm^2/train. At the JLC-Y, a more elaborate study shall be needed on a detailed geometry of beam pipe as well as a tracking algorithm in the CDC with the "exceeded" occupancy even if the innermost layer of the VTX may be overwhelmed by backgrounds.

Table 10.1: Pair backgrounds for 4cm$^{\phi}$ beam pipe at B=2 and 3 Tesla for beam parameters of the basic JLC-A(95 bunches/train) and the high luminosity option of JLC-Y(190 bunches/train), where numbers are for 10 bunch crossings if there is no specification.

	r	z	B = 2 Tesla		B = 3 Tesla	
	cm	cm	JLC-A	JLC-Y	JLC-A	JLC-Y
photons	30	±100	3076	6082	371	946
vtx-1:hits	2.5	±7.5	2186	3279	900	1205
/mm^2/train			0.9	2.8	0.4	1.0
vtx-2:hits	5.0	±15.0	720	920	104	306
vtx-3:hits	7.5	±22.5	406	545	34	138
CDC:hits(tracks)	45∼230	±230	121(101)	235(194)	12(9)	37(28)

Table 10.2: Pair backgrounds for 2 and 3 cmϕ beam pipes at B= 3 Tesla for the JLC-A, where numbers correspond to 10 bunch crossings if there is no specification.

	r	z	B = 3 Tesla	
	cm	cm	2cmϕ	3cmϕ
photons	30	±100	5857	1626
vtx-1:hits	1.5	±4.5	3065	-
/mm^2/train			3.6	-
	1.8	±5.4	-	1906
/mm^2/train			-	1.6
vtx-2:hits	2.5	±7.5	680	804
vtx-3:hits	5.0	±15.0	402	208
CDC:hits(tracks)	45∼230	±230	259(217)	72(63)

10.4.2 Neutrons

We estimated the neutron background produced through photo-nuclear reaction. The pair background particles hit the QC1 and make theEM shower, and the photons in the shower cause the photo-nuclear reaction. The neutrons produced here can spread over the entire detector inside the iron structure.

The pair background particles which can go through the QC1 cannot be transported along the same line as the main extracted beam and will hit the components of the extraction beam line resulting the EM shower. The beamstrahlung photons have the very small angular divergence but eventually hit the beamdump and also produce neutrons. These neutrons can come back to the IP region through the hole for the beam pipe.

In order to study the neutron background produced at the QC1, we used a computer code written by T.Maruyama at SLAC for the neutron generation built into GEANT3. For the neutron transportation in GEANT3, FLUKA(for $E_n > 20$ MeV) or MICAP(for $E_n < 20$ MeV) was used. The cut-off energy for neutral hadrons was 1 keV. We counted the number of neutrons passing the z = 0 plane in the simulation. We found 66 neutrons passing the plane in r < 10 cm area for 1000 bunch crossing. This number corresponds to $3 \times 10^7/\mathrm{cm}^2\mathrm{y}$ near interaction point. As the main tracker the central drift chamber (CDC) with gas mixture of CO_2:Isobuthane(C_4H_{10})=90:10 is being considered. Since this gas mixture contains hydrogen atoms, neutrons can make background hits by elastic scattering. The number of the background hits in the CDC we obtained by the simulation is 800 hits/train.

We have also estimated neutron backgrounds using Fluka98 program. In this calculation, we used the magnetc field consisted of the detector solenoid of 2 Tesla, the QCS magnets, and the compensation magnets to cancel out the solenoid field in QCS region. In this configuration, the magnetic field vector which points along beam direction at IP region changes the direction to perpendicular to the beam axis. Since the Z components of the magnetic field which could trap soft $e^{\pm}$ was reduced, more $e^{\pm}$ hited the inner surface of QCS. However, neutrons which returned to IP were produced mostly at the front surface of QC1, the large increase of neutron yield by this effect was not observed.

In FLUKA simulation, the cut off energy for neutron transport was 1 KeV while those for e^+/e^- and photons were 10.511 MeV an 4 MeV, respectively. As seen in Fig. 10.10, the only few neutron had energy less than 10 KeV.

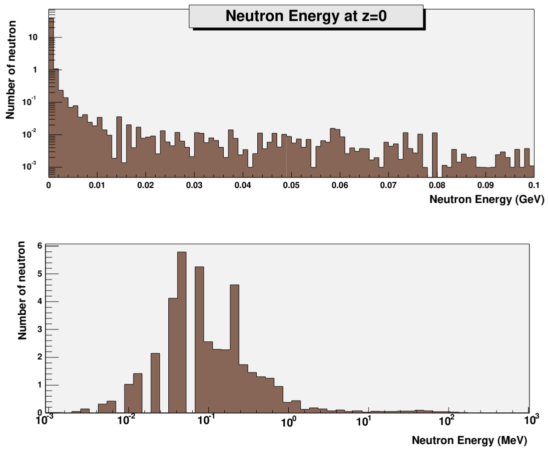

Figure 10.10: The energy spectrum of neutron which return to at IP. Note that the scaling of upper anad lower figure is differenct: Upper figure is log Y scaling, and lower figure is log X scaling.

From the Fluka simulation, we obtained the number of neutron distribution at Z=0 as shown in Fig. 10.11. From this figure we got the total number of neutron within the radius of 10 cm is 292 for 1000 bunch crossing (BX) (entries in the figures are doubled to count backgrounds by e^- and e^+). If uniform neutron distribution is assumed the average neutron flux is $0.93 \times 10^{-3}\ n/\mathrm{cm}^2/BX$. For 1 year (10^7sec), we get 13×10^7 neutrons $/cm^2/y$ at IP. The result is consistent with the Geant3 simulation within a factor of 4, if we neglect a difference of magnetic field distribution used for the simulations.

At present it is diffcult to make a reliable estimation on the neutron background from the downstream because we don't have the design of the beam extraction line of the JLC yet. So we made a very rough estimation on it. By the detector simulation it was found that among the total energy of 100 TeV of the pair background particles in one bunch

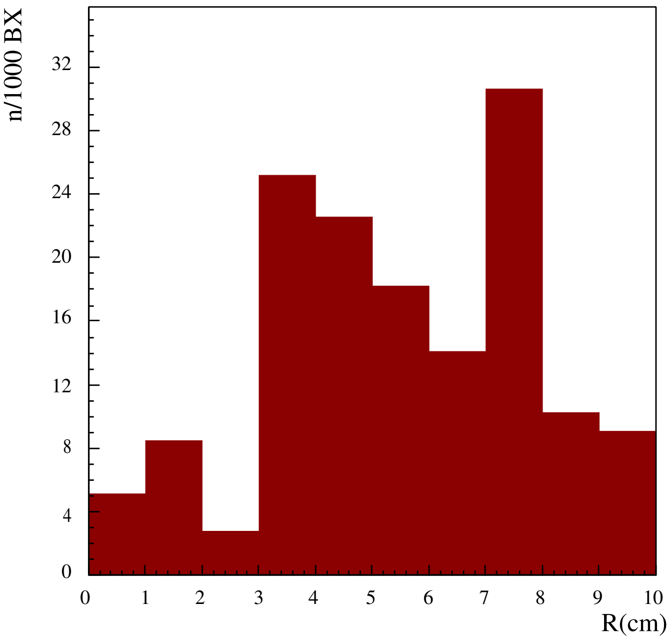

Figure 10.11: The number of neutrons as a function of radius at Z=0 (IP). The vertical axis is scaled so that it gives the number of neutron for 1000 bunch crossing.

crossing, 13 TeV is absorbed in the QC1 and 87 TeV goes downstream. By scaling the neutron background from the QC1 with the deposited energy, we get the upper limit of the neutron background produced by pair background particles at the QC1 and other beam line components downstream of the QC1 as $1.5 \times 10^7 \times 100\text{TeV}/13\text{TeV} \sim 1 \times 10^8/\text{cm}^2\text{y}$.

For the estimation of the neutron background from the beamstrahlung photons, we assumed all photons lose their energy in the water beam dump located at 300 m from the IP. The electron/positron beam was assumed to be bent before the water beam dump and dumped elsewhere so that the neutrons from the $e^{\pm}$ dump can be shielded sufficiently.

Using the GEANT3 simulation with the neutron generation code we found that 6×10^{20} neutrons are produced in one year which is reduced to 1×10^{17} at the surface of the beam dump on the IP side owing to the self shielding by the water. If the solid angle acceptance at the IP is simply multiplied, the resulting neutron yield at the IP is $2 \times 10^7/\text{cm}^2\text{y}$.

According to the Fluka98 simulation, the neutron yields at the surface of water dump is 2.8×10^{17} neutron per year which corresponds to $5 \times 10^7 n/cm^2/y$ at IP if we take into account the acceptance of solid angle and contribution from two water dumps are added.

10.5 Background hits in different detector models

So far the final focus quadrupole magnets(QC1) are assumed to be located 2 m away from the interaction point(l^*=2 m). Recently a new idea of final focus optics is proposed [14] which makes longer l^* of 4.3 m possible. With this optics, the background particles (γ, $e^{\pm}$, neutron) due to back-scattering from QC1 would be reduced. In this article, we present the results of simulation studies on the pair-background in several detector models which have different magnetic field, mask design, and l^*.

Background hit rate has been studied for four detector models (table 10.5), in partic-

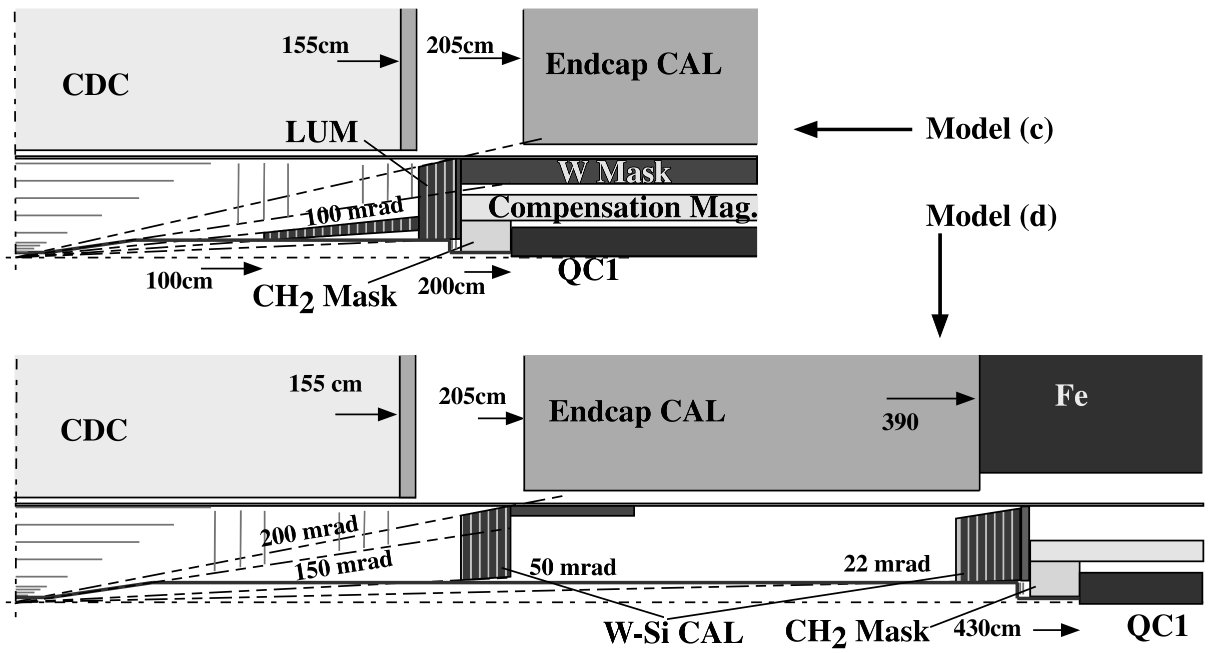

Figure 10.12: Schematic views of model c) and d) detectors in the 3 T model.

ularly, the layout and background estimations in the previous sections are based on 2 T model [1]. Compared with the 2 T model, the outer radius of the central drift chamber (CDC) and inner radius of the barrel calorimeter of the 3 T models are reduced in order to keep the minimum p_t of charged particles which reach the barrel calorimeter constant. The length in z direction of the CDC and the z position of the endcap calorimeter are also reduced in 3 T models. In models a) and b), large conical tungsten masks are placed to shield the back-scattered particles produced by the pair-background particles hitting the QC1 as shown in Fig.10.7. In stead, smaller conical masks are used for the model c). Model d) is for the case of l^*=4.3 m. Two sets of forward calorimeters work as active masks in this model. Schematic views of model c) and d) are shown in Fig. 10.12. The pair-background particles were generated using a program code CAIN [15] for the JLC-A. These particles were put into a full detector simulation program JIM which is based on GEANT3. Magnetic fields of the QC1 and the compensation magnets were taken into account. The cut-off energy was set to 10 keV for γ's and 1 keV for neutrons.

Table 10.3: Detector models and expected background hits per beam crossing: track density at the innermost layer (r=24 mm) of vertex detector(VTX), a number of hits in the central tracker(CDC) by γ and neutron, and an energy deposit in calorimeter(CAL), where models a) and b) are called as 2 T model and models c) and d) are called as 3 T model.

	B(T)	l^*(m)	Mask	VTX(/cm^2)	CDC(γ)	CDC(n)	CAL(MeV)
Model a)	2	2	150 – 200 mrad	0.7	2	30	600
Model b)	3	2	150 – 200 mrad	0.4	1	2	900
Model c)	3	2	70 – 100 mrad	0.4	2	2	900
Model d)	3	4.3	–	0.4	1	0.1	30

The results of the simulation are given in table 10.5. Background hit rate of CDC by neutrons in the 2 T model is quite high because 10 cm thick tungsten mask is not enough to stop neutrons. In the 3 T models, the CDC hit rate by neutrons is reduced because the neutron source (QC1) is surrounded by the endcap calorimeter which works as a neutron shield. With l^*=4.3 m optics, the background source is located farther from the detector components and the background hit rate of the detectors get still less. The simulation was also performed with the JLC-Y. The result shows about two times more background, while the luminosity is 3 times more than that of the JLC-A.

10.6 Pair monitor

10.6.1 Design:3D pixel device

10.6.2 Performances

The disk-shaped pair monitor comprizes double layers of active pixel sensors whose pixel size and thickness are $100 \times 100\mu\text{m}^2$ and 300μm of silicon, respectively. The inner and outer radii are 2 and 8.5cm, respectively. The pair monitor should measure positions and energy deposits of electrons or positrons and secondary photons. Figure 10.13 shows the energy deposits simulated with detailed geometries by JIM, where the pairs have been generated with beam parameters of JLC-A by CAIN21d[15]. Many of them hit only one cell and, as clearly seen in this figure, a very sharp peak appears around 100keV. Therefore, they can be effectively discriminated from the secondary backgrounds simply by a 70 keV threshold in energy deposits.

In order to see how we can measure the beam sizes, pairs have been generated with five different vertical beam sizes at IP by CAIN[15], *i.e.* $\sigma_y = \sigma_y^o$(basic), $2 \times \sigma_y^o$, $3 \times \sigma_y^o$, $4 \times \sigma_y^o$ and $10 \times \sigma_y^o$ for the statistics of 20, 40, 60 50 and 110 bunch crossings, respectively, while the other beam parameters are the same as the basic ones. The minimum energy of the pair particles was 3 MeV.

Radial distributions of the pairs are shown in Fig.10.14, where the number of hits are normalized at 20 bunch crossings for realistic statistical comparisons. All five histograms have sharp shoulders, while negligibly small tails are due to those scattered inherently at large angles. As clearly seen in this figure, positions of the shoulders do not depend on the vertical beam size(σ_y) indeed as described in [16]. Since they depend on the horizontal beam size(σ_x) as well as well-known beam intensities, the horizontal beam size can be estimated by the radial distribution.

The most interesting observable is the distribution of azimuthal angles, since the angles carry an information of the vertical beam size as a function of aspect ratio,$A \equiv \sigma_x/\sigma_y$. Among the pair particles, particles of the same charge as the oncoming beam must be deflected with large angles because of repulsive Coulomb forces. When the oncoming beam has a large aspect ratio, the particles are scattered asymmetrically due to the asymmetric Coulomb potential, that is, more vertically than horizontally. Figure 10.15 shows a scatter plot of hits in the pair monitor on a plane of azimuthal angle and radial position. Two dense bands can be seen, which are made of particles deflected upward or downward and swum helically in the 2 Tesla solenoid field. In order to quantify the asymmetry, we set four regions (H_2, L_1, H_1, L_2) as shown in Fig.10.15. Area of H_2 and L_2 is larger than that of H_1 and L_1 because of left-right asymmetry with 8 mrad crossing angle. Then, we

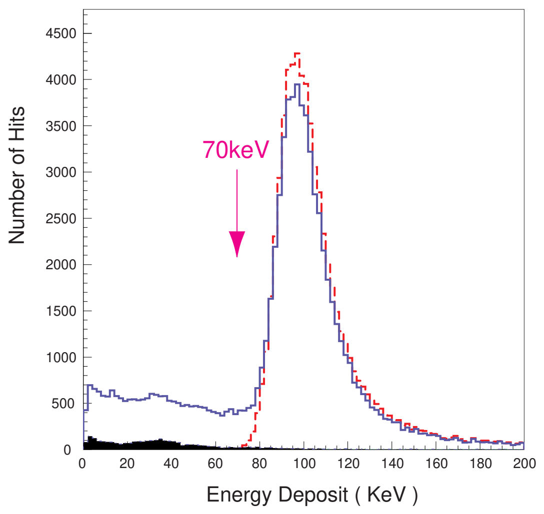

Figure 10.13: Energy deposits in the pair monitor. The solid and dashed histograms show energy deposits in each cell and those by a track, respectively. The black one show those of secondary backgrounds in each cell.

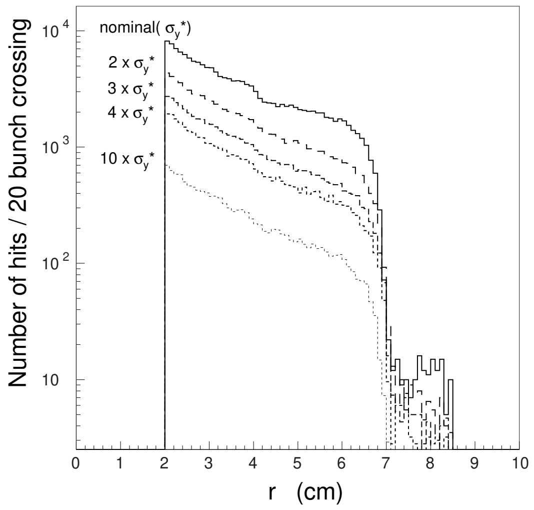

Figure 10.14: Hit distributions normalized at 20 bunch crossings as a function of r for energy deposits of >70keV, where histograms correspond to 5 vertical beam sizes at IP; i.e. basic (σ_y^o), $2\times, 3\times, 4\times$ and $10 \times \sigma_y^o$
.

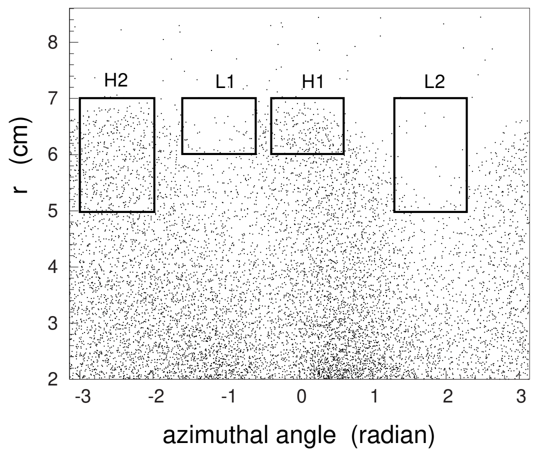

Figure 10.15: Scatter plot of hits with >70 keV energy deposits in the pair monitor on a plane of azimuthal angle(x) and radial position (y), where four sensitive areas are also depicted in order to calculate a ratio of $(L_1 + L_2)/(H_1 + H_2)$
.

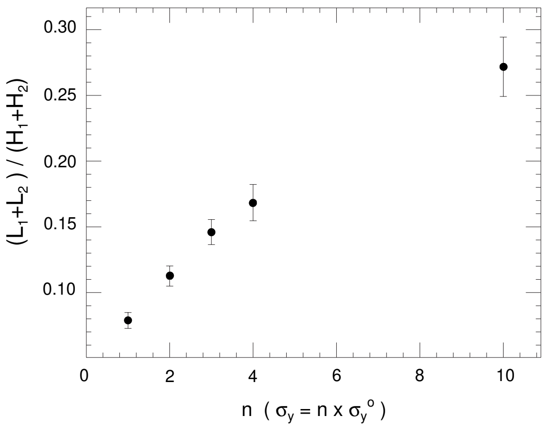

Figure 10.16: Ratio of $(L_1 + L_2)/(H_1 + H_2)$ as a function of vertical beam size ($\sigma_y = n \times \sigma_y^o$) at IP, where error bars are statistical corresponding to 20, 40, 60, 50 and 110 bunch crossings for n=1,2,3,4 and 10, respectively.

defined a ratio, $R \equiv (L_1 + L_2)/(H_1 + H_2)$ as proposed[16], where L_1, L_2, H_1, H_2 represent the number of hits in each region. It is expected that R becomes smaller as A increases while $R = 1$ for round beams. The simulation results are shown for beams with five different σ_y's in Fig.10.16. Up to $4 \times \sigma_y^o$, we observed a linear relation between R and the vertical beam size. Under the basic beam condition, the vertical beam size could be measured for 100 bunch collisions with $< 10\%$ statistical accuracy. Since this method, *i.e.* counting hit numbers in specific regions with energy deposits of greater than 70 keV, is very simple, the pair monitor can be a feedback device for beam tuning in realtime. With the fast gate, the pair monitor should detect the pairs in specific bunches in order to investigate a variance of beam size in a bunch-train.

10.7 Luminosity Monitor and Active mask

Luminosity monitor is located at 163cm from the interaction point (IP), which is made of tungsten (W) of 15cm thickness ($42.86X_o$) and the (polar) angular coverage ranges from 0.05 to 0.15 radian. It is segmented into 32, 16 and 128 divisions in radius (r), azimuthal angle (ϕ) and longitudinal coordinate (z), respectively. The physical dimensions are 5mm, 3.2-9.7cm and 1.17mm in r, ϕ and z, respectively. At present, all the tungsten segments are treated as sensitive detectors; that is, energy deposits in all segments are calculated in simulations. A real detector must have some sensitive layers made of active material such as scintillator, silicon pad, or crystal (e.g. BGO) instead of tungsten.

A front part of the conical mask is instrumented to measure energy deposits in electromagnetic showers. The mask is made of tungsten. The longitudinal position is 30cm from IP and the angular coverage is from 0.15 to 0.2 radian. The active mask consists of 8 layers of silicon pads (Si(200μm) + G10(300μm)), where the first W layer is 5mm thick and the other W layers are 1cm thick. In simulations, energy deposits in silicon pads are calculated. The active mask is segmented into 8-10 and 32 divisions in r and ϕ, respectively. The physical dimensions are 2mm and 0.9-1.2cm in r and ϕ, respectively.

The e^+e^- pairs were generated with a statistics corresponding to 100 bunch crossings (~1 train crossing) by cain21d, where the nominal JLC-A machine parameters at $\sqrt{s}$=500GeV were used. They should always overlap on any physics event at JLC. For the signals, electrons of 50 or 250GeV were generated into the front center of the luminosity monitor and the active mask. Their energy deposits were calculated by the JIM simulation, and they are listed in Tab.10.7 ,where energy deposits due to 250GeV muons are also listed. As clearly seen, energy deposits of e^+e^- pairs decreases at higher magnetic field (B=3T). The luminosity monitor contains all electromagnetic shower while the active mask has shower leakage of ~10% in radial direction for a 250GeV electron compared with a 50GeV electron. The longitudinal leakage in the active mask with $21.4X_o$ was estimated to be ~1% even for a 250GeV electron.

Although the total energy deposits of e^+e^- pairs are very large, the spatial distributions are very different from those of electrons as seen in Fig. 10.7 and 10.7 for LM and AM, respectively. The simulations show that most of the pairs are absorbed near the surfaces of $\sim 1X_o$ depth because of their low energies while the 50GeV and 250GeV electrons have shower maxima at $5X_o$ and $8X_o$, respectively.

Among the total energy deposit of 152 (46.7) GeV/train in LM due to e^+e^- pairs, only 54*(14*) GeV comes from the front at B=2(3)T, while most comes from the inner-back.

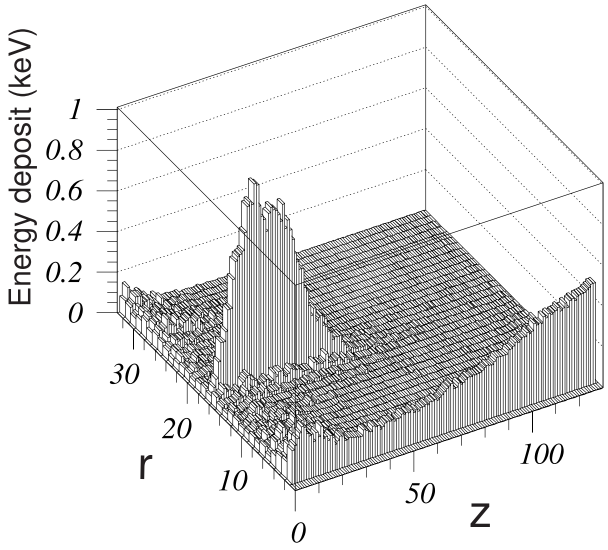

Figure 10.17: Energy deposit of a 50 GeV electron together with e^+e^- pairs whose statistics corresponds to 100 bunch crossings in LM. Left and right figures are plotted in r-z and ϕ-z planes, respectively.

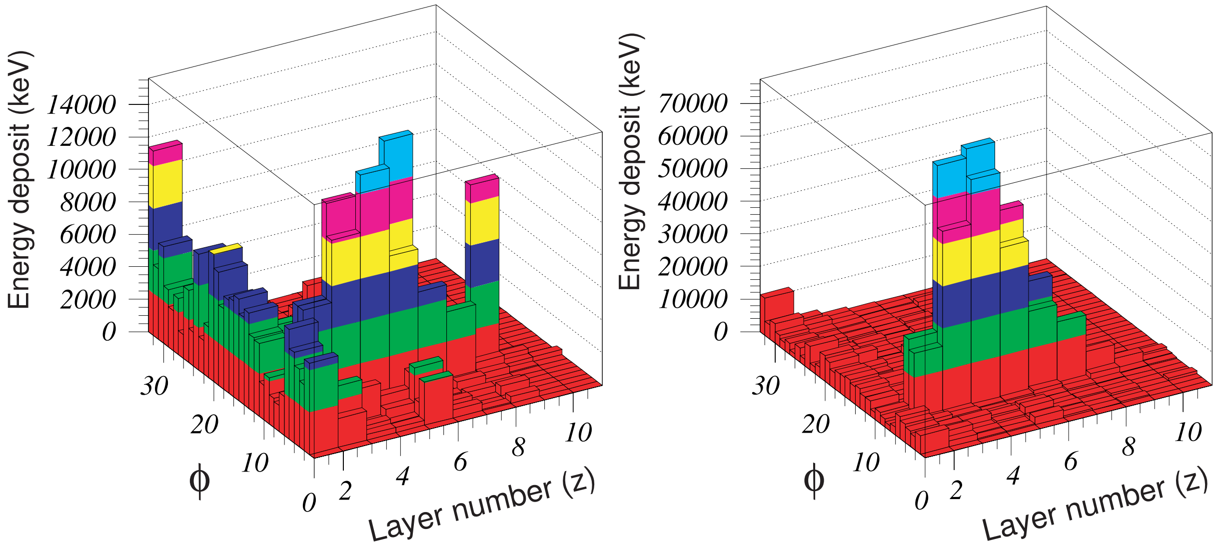

Figure 10.18: Energy deposit of a high energy electron together with e^+e^- pairs whose statistics corresponds to 100 bunch crossings in AM. The electron energies are 50 and 250 GeV in left and right figures, respectively.

Table 10.4: Energy deposits in the luminosity monitor (LM) and active mask (AM) per 100 bunch crossings.

B=2T	e^+e^- pairs	50GeV e	250GeV e	250GeV μ
AM	264MeV	120.4MeV	541.0MeV	0.48MeV
LM	152GeV	49.9GeV	249.5GeV	1.67GeV
B=3T	e^+e^- pairs			
AM	29.3MeV			
LM	46.7GeV			

(* sum of incoming energies). The ϕ-segmentation (16 div.) is important for angular resolution, and the r-segmentation (32 div.) is desired to determine polar angle with an accuracy of a few milli-radian. So, a fine-segmented W/Silicon calorimeter seems to be ideal. The thickness of tungsten layers must be optimized for energy-resolution.

For AM, first layer (5mm thick W) has $\sim$50% energy deposit for e^+e^- pairs. Again, ϕ segmentation (32 div.) is important for angular resolution. 8 layers of W/Si-pad calorimeter ($21.4X_o$) works very well for vetoing high energy electrons.

10.8 Support system

To support the components at the interaction region, 80 cm diameter with 10mm thick of support tube made of CFRP was proposed. The support tube is usually acted on self-weight of the components and vibrations from the ground. One of the important requirements is that relative displacement between QC1 separated by 4 m has to be kept less than 1 nm. Therefore, to optimize the support tube configuration, static analysis and dynamic analysis were carried out. And to realize these analyses, the excitation test using prototype model is being done.

At the initial concept of support tube, 12 m long single CFRP tube is provided and it is supported on the both of iron end yokes. Analysis in terms of this configuration was studied and reported at the 2nd ACFA-LC workshop in Seoul. It showed that relative displacement to be excited by ground motions were completely negligible between QC1. Since then, a new analysis has been executed on a system, where the two final focus doublets are independently supported by two identical cantilevers. If the system is stable in terms of ground motions, it is experimentally more preferable because of less material in detectors as well as easier assembling of the doublets and more straightforward installation.

In the calculations for the support tube, stiffness of the support tube was ignored. The bending stiffness can be defined to D=EI, where D is the bending stiffness, E is Young's modulus and I is moment of inertia. Moment of inertia is proportional to 10^4 of the thickness. Thus, compared to the bending stiffness between 10mm thick of CFRP support tube and tungsten mask, stiffness of the tungsten mask is to be 25 times larger. So, only the stiffness of the 10 cm thick tungsten mask was taken into account. The tungsten mask consists of 4 pieces in the longitudinal direction and 2 pieces in the circumferential direction as shown in Fig. 10.19. Overall length after assembling is 8 m and load conditions are self-weight of 32 tons for tungsten mask and other components of 9 tons, respectively. The mechanical properties of tungsten are, Young's modulus is 415 GPa, density is 19.3 and tensile strength is 900 MPa, respectively.

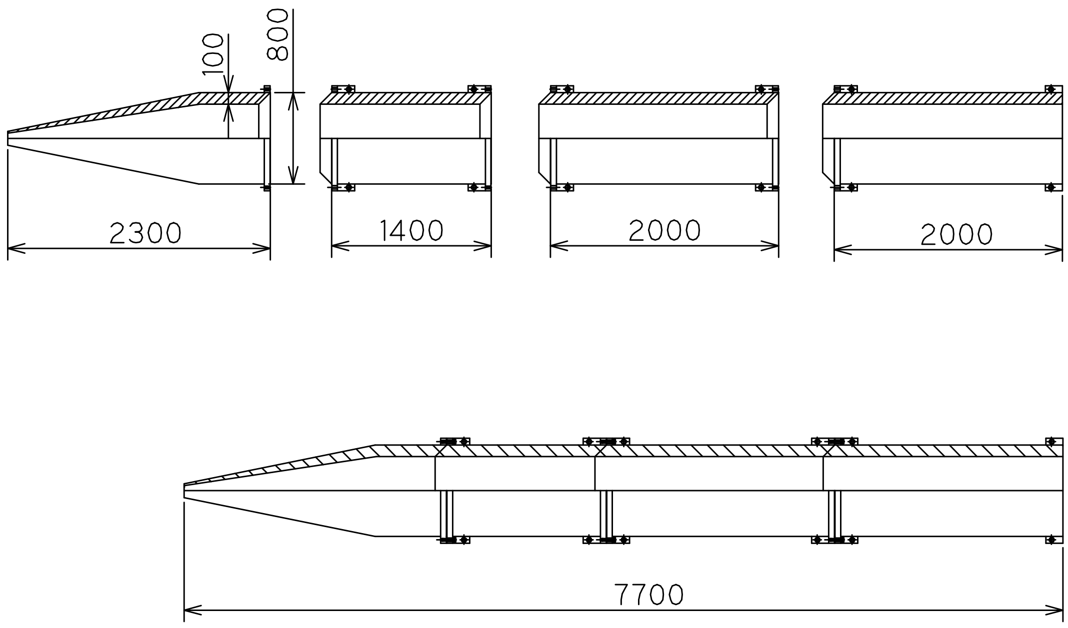

Figure 10.19: Configuration of the tungsten mask.

Figure 10.20 shows the results of static analysis. The gravitational sag due to load of 41 tons was calculated to be 1.6 mm at the top of tungsten mask when it assumed that the tungsten mask is fixed to two points where 7 m far and 8 m far from the interaction point. Stress level was to be 23 MPa that is sufficient low against the tensile strength. This deformation is not accepted. If the mask is additionally fixed at 3.85 m far from the interaction point, the gravitational sag can be improved to 0.09 mm. This indicates that the mask is supported at the back end and the iron yoke.

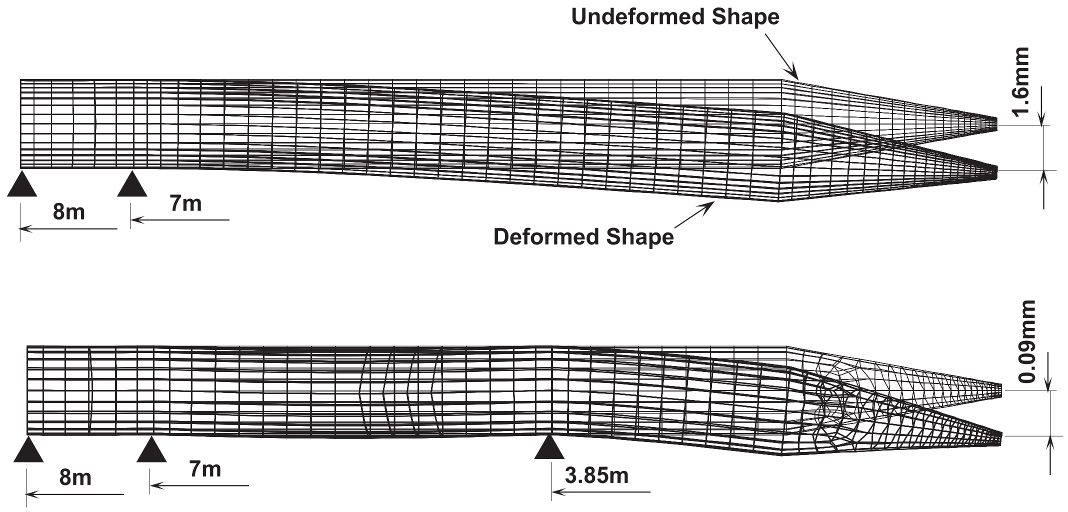

Figure 10.20: Deformation of the tungsten mask due to a load of 41 tons.

To know the behavior against vibration such as ground motion, dynamic analysis was carried out. Kinds of dynamic analysis are modal analysis to know the natural frequency and mode shape of structure, harmonic response analysis to know the amplitude at the resonant frequency and spectrum analysis to know the amplitude by input the combined different vibration characteristics. In the dynamic analysis, two analysis models were assumed. One is the support is fixed to the rigid base so called "rigid case". And the other is the support is fixed to the soft base whose natural frequency is 15 Hz, "soft case". Usually, natural frequency of large structure is supposed to be relatively low, and from the viewpoint of the seismic design, natural frequency of large structure is to be around 15 Hz. Constraint points are 3 points where 3.85m, 7 m and 8 m from the interaction point, respectively.

As shown in Fig. 10.8, the result of modal analysis on the rigid case is calculated to natural frequency of 71 Hz at first mode, 179 Hz at second mode and 202 Hz at third mode, respectively. In the soft case, natural frequencies are calculated to be 15 Hz at first mode, 54 Hz at second mode and 93 Hz at third mode, respectively.

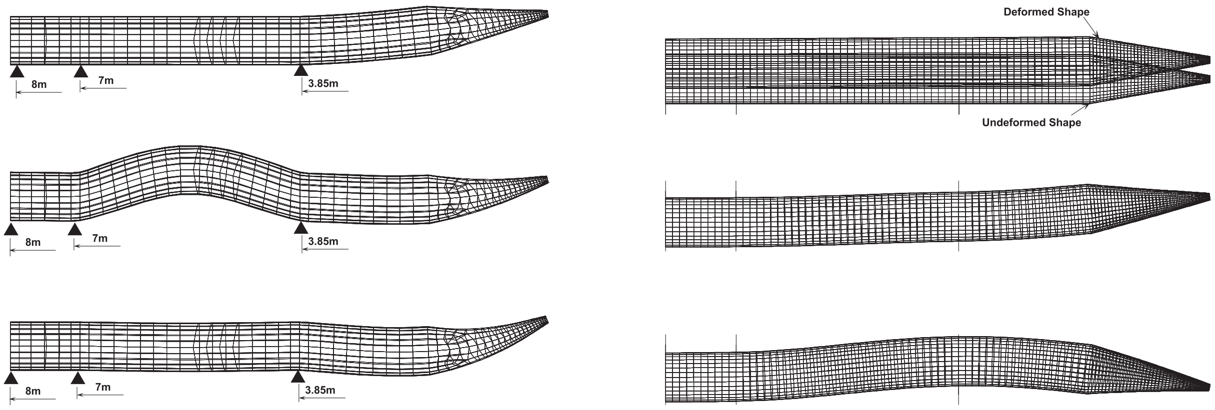

Figure 10.21: Mode shapes by the modal analysis at the first, second and third natural frequencies. Left and right figures show rigid and soft cases, respectively.

As the next step of dynamic analysis, harmonic response analysis was done. This calculation is a technique used to determine the steady-state response of structure to loads that vary harmonically with time. Applied acceleration was determined from data of grand motion measured in the TRISTAN tunnel. Correlation of amplitude and frequencies are 3 μm at 3 mHz, 1 μm at 0.1 Hz, 10 nm at 1 Hz and 5 Hz, respectively. From these data, acceleration forces can be converted to $1 \times 10^{-7}, 4 \times 10{-}^{4}, 4 \times 10^{-5}$ gal and 2×10^{-4} gal, respectively. So acceleration force of 2×10^{-4} gal was chosen because of the largest value. Dumping ratio was set to 2 %. The calculation results of the rigid case is about 0.2 nm as shown in Fig. 10.8. Responded deformation at the soft case is to be 6 nm.

At the spectrum analysis, three kinds of measured amplitude are input to the constraint points, and then vertical deformations at each resonant frequency are calculated. Figure 10.8 shows the calculation results. The deformation of rigid case at each mode is calculated to be from 3 nm to 8 nm. The soft case was turned out to be more stable then the rigid case since the structure was so rigid that it would not be deformed locally. For the soft case, the largest movement was smooth shift by 2.5 ± 0.2 nm at the first mode of 15Hz. Good coherencies of ground motions have been observed at such short distance between two points in many places. Therefore, the results are encouraging.

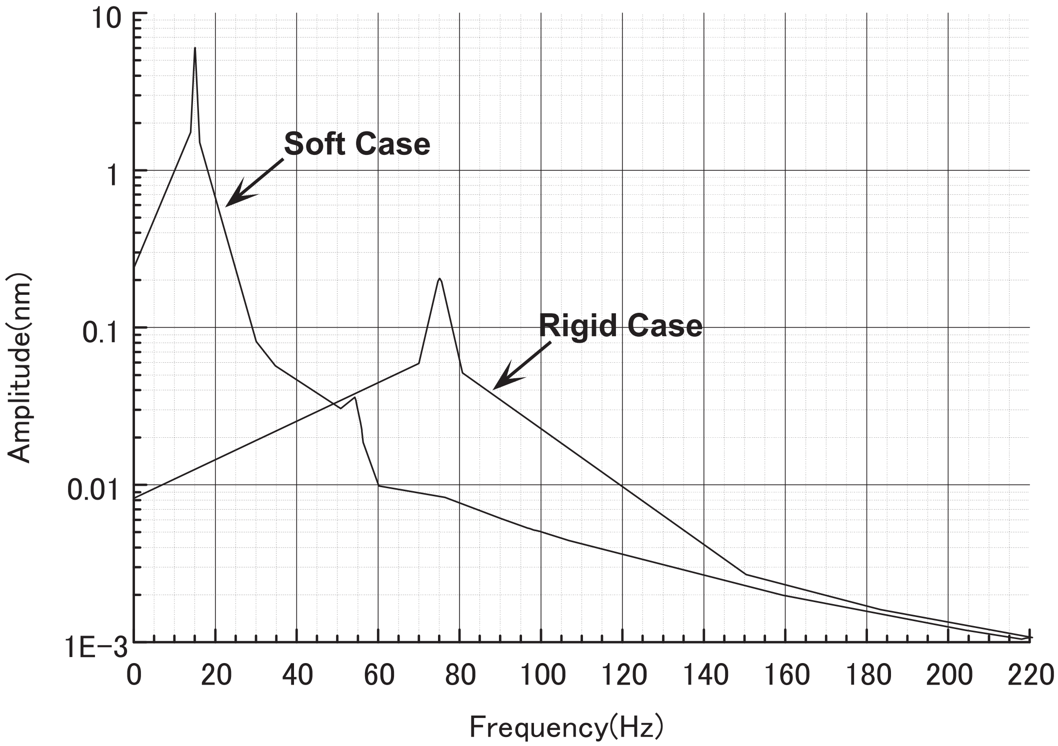

Figure 10.22: Results of the harmonic response analysis , where peaks are at the first natural frequencies.

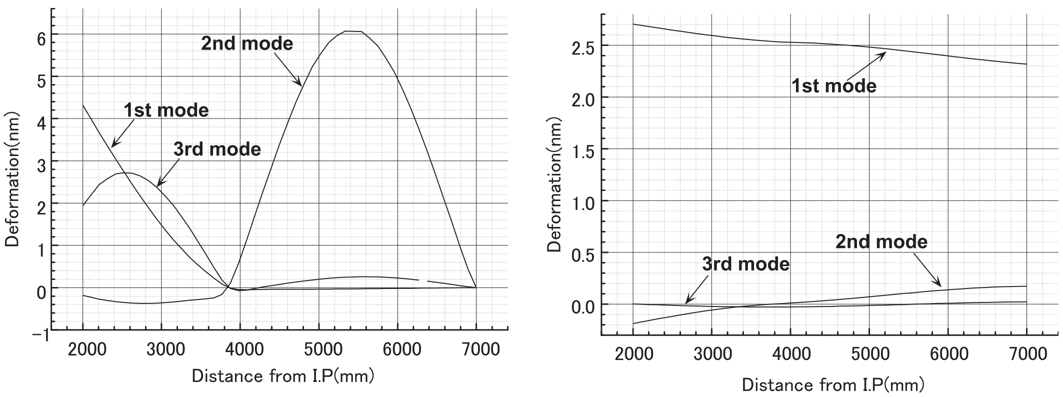

Figure 10.23: Deformations of the tungsten mask between 2 and 7 m from IP by the spectrum analysis. Left and right figures show rigid and soft cases, respectively. Mode shapes are similar to those of the modal analysis.

Vibration test using prototype model is just in process. The main purpose is to evaluate a validity of calculations by measuring oscillation properties of the prototype model. In the prototype model design, natural frequency resembles to the real support tube as possible. Two kinds of prototype models are provided those are cantilever type and both ends fixed type. Size of the prototype model is 800mm long and square aluminum bar(100 mm wide and 20 mm thick). They are excited by maximum strength of 10kg long stroke shakers. Input signals are provided by manual sine controller. In the test, some study items are planed; (a) measurement of natural frequencies and amplitudes of the oscillations, (b) measurement of amplitudes with different phases at both ends, (c) comparison between both-ends and cantilever support cases, (d) effects of supporting methods, that is, number of bolts and its sizes (e) measurement of dumping coefficients. Configuration of the data taking as shown in Fig. 10.8 is two laser position meters are set to the fixed end and free end of the bar, and velocity sensor (Geophone) and G-sensor are placed on the fixed end. Then those data is taken by the data logger and they are sent to the PC computer. Data from Geophone is also able to analyzed by FFT.

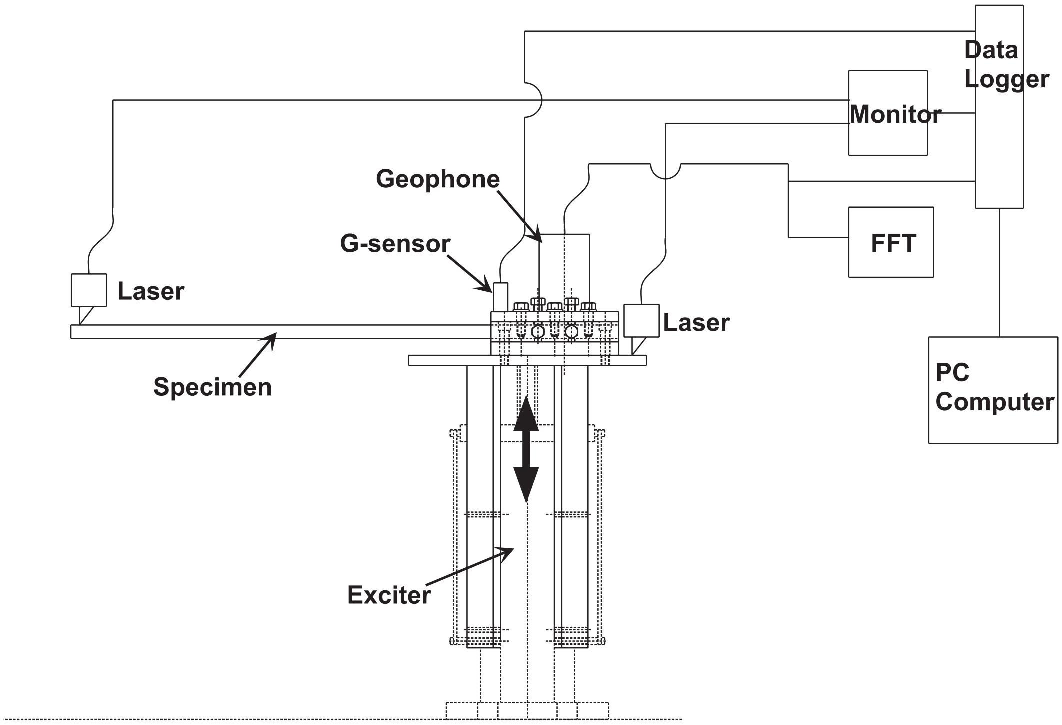

Figure 10.24: Test configulation of the prototype in a cantilever case.

10.9 Dump line

Preliminary design of the dump line, beam line after the interaction point, was studied. SAD [17] was used for this design. In the beam line, energy distribution of the beam after the collision should be measured with resolution less than 0.1% for $\delta E/E > -1\%$ where $\delta E/E$ is the relative energy deviation from the nominal energy. On the other hand, beam loss in the line should be as little as possible to reduce background for the detector. In order to measure beam energy distribution, beam is focused again at the second focal point, FP2. And vertical bending is introduced to make vertical dispersion at FP2. The optics of the beam line is shown in Fig. 10.25. Four quadrupole magnets, two sets of doublet, are used for re-focusing. Two vertical bending magnets are used for introducing dispersion. Magnetic fields of the two final quadrupole magnets of the opposite main (incoming) beam line were also considered. Transverse distribution of monochromatic beams at FP2 are shown in Fig. 10.26. Each cluster of the distribution represents a distribution of electrons in a monochromatic beam of $-\delta E/E^o_{beam}$=0, 0.2, 0.4, 0.6, 0.8 or 1.0%, where the beam energy (E^o_{beam}) is 250GeV. Here, we assume the transverse beam parameters after collision as follows; normalized emittances $\epsilon_{x/y}$=1600/20($\times 10^{-8}$ m) and beta function $\beta_{x/y}$=4/0.15(mm), which have been estimated for the JLC-C parameters by CAIN. Energy distribution will be measured, for example, scanning a horizontal laser beam with small vertical size, detecting gamma rays produced by Compton scattering. And, roughly speaking, the resolution would be less than 0.1% for $\delta E/E > -1\%$.

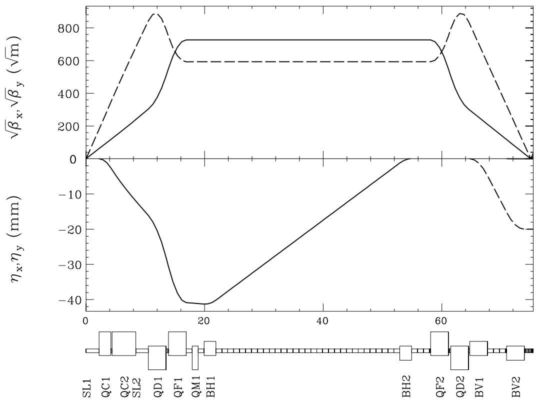

Figure 10.25: Optics of the beam extraction line.

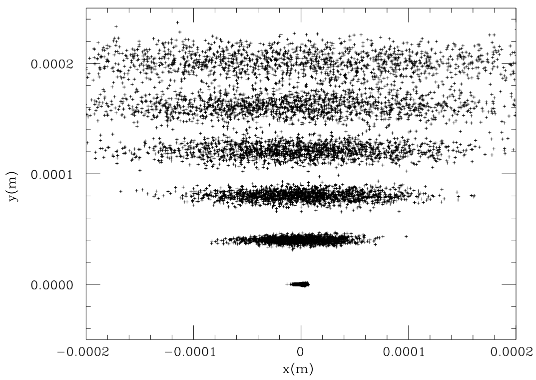

Figure 10.26: Transverse distribution of monochromatic beams at FP2.

To study beam loss, a tracking was performed using SAD, where 40000 macro particles were used. The initial conditions of the macro particles were also calculated using the CAIN. Some simple aperture at each magnet was assumed and particles went out of it was assigned to be lost at the position. Figure 10.27 shows the energy distribution of survived particles (solid) and that of lost particles (dashed). About 0.9% of the total particles (which had low energy) were lost. Figure 10.28 shows the rate of neutron dose at the interaction point. We assumed that one neutron would be created per 10 GeV beam loss. The neutron dose was calculated considering the distance between the IP and the lost position assuming no shielding between them. In total, $4 \times 10^{11}/\mathrm{cm}^2$ neutron dose is expected in one year. This result may not be acceptable. But it should be noted that the self-shielding effect or additional shield is not included in this study. In addition, more realistic (and complicated) assumption of the aperture may reduce the beam loss. If we loosen the requirement for the resolution of the energy distribution measurement, the beam line optics may be modified to reduce the beam loss.

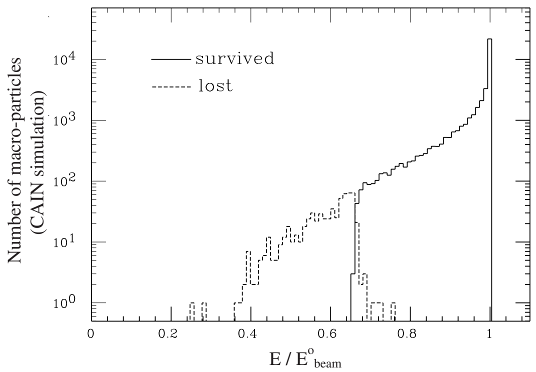

Figure 10.27: Energy distribution of survived particles (solid) and lost particles (dashed).

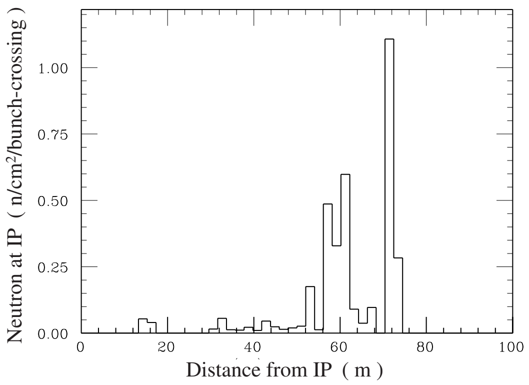

Figure 10.28: Rate of neutron dose at the interaction point (/cm^2/bunch crossing).

Bibliography

[1] JLC-I, KEK Report 92-16, December, 1992.

[2] K.Fujii, T.Matsui and Y.Sumino,*Phys. Rev.* D **50**, 4341 (1994).

[3] M.M.Nojiri, K.Fujii and T.Tsukamoto, *Phys. Rev.* D **54**, 6756 (1996).

[4] K. Yokoya, talk presented at ACFA-LC working group meeting at KEK, March 17, 1999.

[5] JLC Design Study Group: *JLC Design Study*, KEK Report 97-1, April 1997, see also ftp://lcdev.kek.jp/pub/DesignStudy/.

[6] V. Telnov, *Phys. Rev. Lett.* **78**, 4757 (1997).

[7] D.Burke, proceedings of Workshop on *Physics and Experiments with Linear e^+e^- Colliders*, eds. R.Orava, P.Eerola and M.Nordberg (World Scientific, Singapore, 1992) p51, and references therein.

[8] E.A.Kushnirenko,proceedings of *The International Workshop on Final Focus and Interaction Regions of Next Generation Linear Colliders*, May 2-6,1992, *SLAC report* SLAC-405,p225.

[9] Y. Namito, talk presented at ISG3 meeting at SLAC, Jan. 25-28,1999.

[10] Zeroth-Order Design Report for the Next Linear Collider, LBNL-PUB-5424, also SLAC Report 474 or UCRL-ID-124161, May 1996.

[11] T.Tauchi, K.Yokoya and P.Chen, *Part. Accel.* **41**, 29 (1993).

[12] H.Yamaoka, *Design of solenoid magnet and support tube*, talk at the 2nd ACFA Workshop.

[13] T.Tauchi, proceedings of the 1st ACFA workshop on physics and detector at the linear collider (the Beijing workshop), Beijing, China, November 26-27, 1999, edited by T.Matsui and Y.Kuang, p.109, KEK Proceedings 99-12, September 1999.

[14] Raimondi, P., and Seryi, A., SLAC-PUB-8612 (2000).

[15] K.Yokoya, CAIN version 2.1d. The detailed informations can be obtained from the CAIN home page of URL = http://www-acc-theory.kek.jp/members/cain/ .

[16] T. Tauchi and K. Yokoya, *Phys. Rev.* E **51**, 6119 (1995).

[17] SAD is a computer program complex for accelerator design.
http://acc-physics.kek.jp/SAD/sad.html.

Chapter 11

Tracking

11.1 Vertex Detector

11.1.1 Overview

Design Criteria

The primary role of the vertex detector is to reconstruct the secondary and tertiary decay vertices of B and D meson decays and tag bottom(b) and charm(c) quark jets. Distinguishing heavy flavor (b and c) jets from light flavor(u, d, abd s) jets is relatively easy. It can be achieved by looking for tracks which have impact parameters significantly greater than zero. In precision measurements of some physics processes at the linear collider, discrimination between b and c quark jets is required. In this case reconstruction of secondary and tertiary vertices is necessary for efficient discrimination of b jets from c jets. Better spatial resolution and tracking efficiency are required for the vertex detector to obtain better tagging efficiency of the jet flavor.

The vertex detector consists of several layers of sensors surrounding the interaction point concentricaly. Vertex reconstruction is performed by extrapolating tracks measured by several layers of the sensors. In order to get better vertex resolution and better flavor tagging efficiency, the vertex detector should have the following features:

- The length of the extrapolation should be as short as possible, i.e., the innermost layer should be as close to the interaction point as possible.
- To minimize the effect of multiple scattering, the thickness (in radiation length) of the sensors and supporting ladders, particularly that of the inner most layer, should be as thin as possible.
- The sensors shoud be two-dimensional (pixel type) sensors with high granularity in order to separate near-by tracks in a collimated jet. Of course better spatial resolution is desirable.

When we try to satisfy these requirements, we are faced with several difficulties. As discussed in section *.*, the track density of the pair background particles increases near the interaction point. High background hit rate causes the problems of wrong tracking due to fake hits leading to poor vertex resolution, and radiation damage of the sensors. Therefore there is a limit on the minimum radius of the inner most layer. The existence of the beam background gives rise to another requirement for the vertex detector:

- The sensors used for the vertex detector should have enough radiation immunity so that the first layer can be located in the vicinity of the interaction point.

Possible Options

The vertex detector has to consist of pixel type sensors not only for the separation of tracks in a collimated jet but also for the detection of tracks in the environment where a large number of the beam background hits exist. The following technologies can be candidates for the sensors used for the vertex detector.

- **CCD:** CCD (Charge Coupled Device) is an established technology widely used also in commercial products. The thickness of the sensitive region is about 20 μm. The wafer thickness can be thinned down to 20 μm provided that the mechanical strength is assured with an adequate method. Large size chips (1.6×8 cm^2 for SLD [1]) can be made. Relatively sensitive to radiation damage.
- **CMOS pixel sensor:** In CMOS pixels sensors, each pixel has a sensor diode and a read-out amplifier. Signals from the pixels are read out by x-y addressing. The thickness of the sensitive region is about 20 μm. The radiation immunity is better than that of CCDs.
- **Hybrid pixel sensor:** Hybrid pixel sensors have a sensor diode wafer and a readout wafer connected by bump bonding technique. This structure inevitably makes them thicker than CCDs or CMOS sensors. The radiation hardness is excellent.

Among the options listed above, we regard the CCD as a primary candidate for the sensor used for the vertex detector at JLC. We have been studying on the properties of CCD sensors extensively in order to demonstrate the feasibility for the vertex detector at the linear collider experiment. The detail will be described in subsections 11.1.2 and 11.1.3.

Detector Configuration

One possible schematic design of the CCD vertex detector, which is put in the JLC detector full simulator (JIM), is shown in fig. 11.1. Main parameters of the detector are:

- Four layers of CCDs placate at r =24, 36, 48, and 60 mm.
- Each layer has an angular coverage of $|\cos\theta| < 0.9$.
- The thickness of each layer is 300 μm.
- The pixel size of the CCD is 25 μm square.

Hit density of the vertex detector is quite high due to collimated jets and the pair-background hits. In such a situation, at least four layers are necessary for local track finding and self calibration using the vertex detector alone.

In a simple model of the vertex detector which has two layers at r_{in} and r_{out} with the spatial resolution of σ_{in} and σ_{out}, respectively, the impact parameter resolution σ_b can be expressed as

$$\sigma_b = \frac{\sigma_{in} r_{out}}{r_{out} - r_{in}} \oplus \frac{\sigma_{out} r_{in}}{r_{out} - r_{in}} \oplus \frac{0.014 r_{in}}{p\beta}\sqrt{\frac{X_r}{\sin^3\theta}}, \tag{11.1}$$

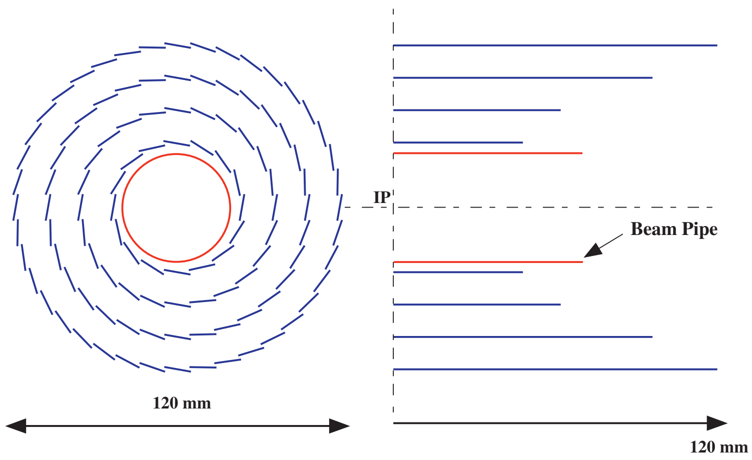

Figure 11.1: Schematic design of the CCD vertex detector for JLC.

where X_r is the thickness of the inner layer in radiation length, p, β, and θ are momentum, velosity, and polar angle of the charged particle, respectively. Outer radius of the vertex detector has less importance on the impact parameter resolution as long as $r_{out} \gg r_{in}$ is satisfied. In the case of the JLC detector model, the impact parameter resolution for high momentum particles better than the expression 11.1 is achieved by combining the vertex detector and the CDC. The reason of this fact is that taking four layers of the vertex detector together as the "in" layer and the CDC as the "out" layer in the expression 11.1 gives smaller value for the first two terms in equation 11.1. Then important parameters for the vertex detector are r_{in}(radius of the innermost layer), σ_{in}(spatial resolution), and X_r(detector thickness).

The innermost layer of the vertex detector is conservatively located at $r = 24$ mm in the present design. With this configuration, a $e^{\pm}$ dose of $\sim 1.5 \times 10^{11}/\mathrm{cm}^2$ is expected in one year at the innermost layer with the solenoid magnetic field of 2 Tesla and with the accelerator parameter set of "A" described in section *.*. As will be shown in subsection 11.1.3, the CCDs of the innermost layer would stand operation of more than 3 years under this rate of radiation dose. If stronger magnetic field is employed, the pair-background particles are confined in the region of smaller radius and the first layer of the vertex detector can be placed closer to the interaction point. The same background rate is expected at $r = 20$ mm with $B = 3$ Tesla. If still smaller radius is required, or if the luminosity of the machine is increased (the machine parameter set "Y" in section *.*, for example), more frequent replacement of the damaged CCDs, still stronger magnetic field, or devices more radiation hard are required.

One of the advantages of the CCD as a tracking device is its excellent spacial resolution. Structure of a CCD sensor is schematically shown in Fig. 11.2. The epitaxial layer of ~ 20 μm thick is the sensitive region. Since most of the epitaxial layer is not depleted, the signal charge (electrons of e/h pairs) difuses thermally in the epitaxial layer and spreads over several pixels even for the normal incident particles. Consequently, high precision position measurement can be achieved by the charge sharing.

As shown in Fig. 11.2, normal CCDs have thick insensitive substrate. When used for the vertex detector, this part shoud de thinned as much as possible to reduce the multiple scattering of charged particles. On the other hand, it becomes more difficult to keep thin silicon wafers flat, particularly operated at low temperature [1]. As an example, we

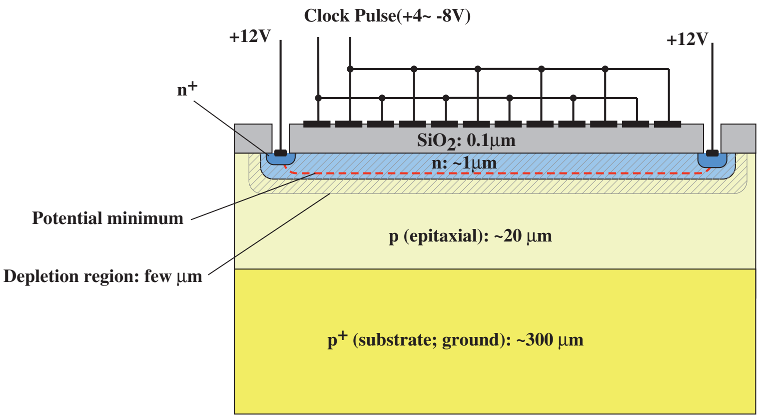

Figure 11.2: Structure of a CCD sensor.

show in Fig. 11.3 a result of flatness measurement of a commercially available CCD which has thinned sensitive area for the purpose of the back-illumination. A sizable bowing presumably due to the temperature difference between at the fabrication process and at the room temperature can be seen. From this point of view, operation of the vertex detector at near room temperature is desireble to minimize the distortion of the CCD wafers. The mechanical structure which can keep the thin CCD wafers flat has to be studied.

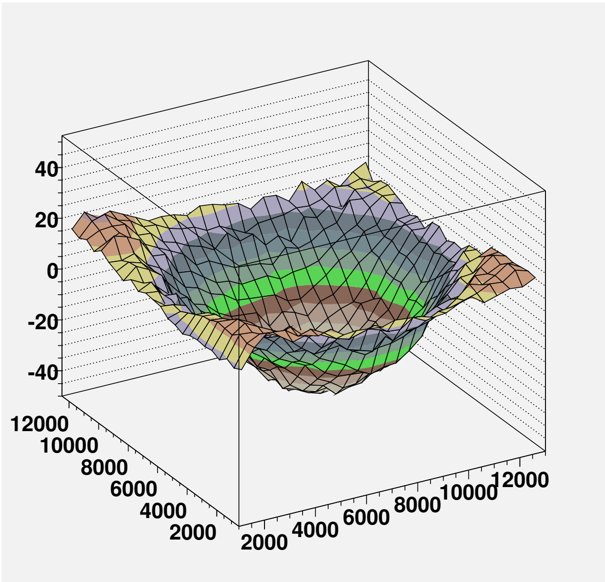

Figure 11.3: Measured surface flatness of a back-thinned CCD sensor. (units in μm)

Each CCD wafers will have multiple readout nodes so that all pixels can be read out during the train crossing interval of 6.7 msec. If we conservatively assume the readout frequency of 10 MHz, each readout channel can read out the area of about 0.4 cm^2 between the train crossings. Since the total area of the CCDs in the vertex detector is about 2000 cm^2, about 5000 readout channels are needed. Higher readout frequency or longer readout period by vetoing next collision(s) can reduce the number of the readout channels.

R& D status

So far, our R&D effort has been devoted mainly to the study of the spatial resolution and the radiation hardness of CCD sensors. In the following subsections, we will describe results of the study in detail and demonstrate the feasibility of the CCD vertex detector. In particular, with the conservative design described above (machine parameter set "A" and r_{min} = 24 mm), it will be shown that the operation of CCD vertex detector near room temperature ($\sim 0°C$) is feasible.

11.1.2 Study of spatial resolution

Factors affecting the spatial resolution

The most important parameter for the vertex detectors is the spatial resolution. Quit a number of factors can affect the spatial resolution. The most obvious is the pixel pitch, but other intrinsic effects can be very important. In the case of an analogue readout system, the spatial resolution of CCD detectors depends on the following parameters,

1. Signal to Noise ratio (S/N),
2. Charge sharing due to carrier diffusion.
3. Digitization resolution in readout system.

We have carried out test beam to measure the spatial resolution in CCD detector. The influence of those parameters to the spatial resolution are presented here.

Test beam

We have tested three types of CCD detectors in Multi Pinned Phase(MPP) operation [2]. In the MPP mode, the array clocks are biased sufficiently negative to invert all phases and the surface potential is "pinned" to substrate potential. As a result, the thermal excitation of electrons is extremely suppressed. It reduces the dark current by a factor of 20 compared with normal non-inverted operation mode. Table 11.1 is a list of the test samples with important parameters. Two of the three CCDs were S5466 [3] fabricated by Hamamatsu Photonics K.K. (HPK) , but with different depth of epitaxial layers, 10μm (HPK10) and 50μm (HPK50), respectively. HPK10 is a commercially available, but HPK50 is specially fabricated for this experiment. Those consists of 512 $\times$ 512 pixels and the pixel size is 24 μm $\times$ 24 μm. Another one was CCD02-06SIS [4] fabricated by EEV Company and is also commercially available. The CCD02-06SIS consists of 385 $\times$ 578 pixels and the pixel size is 22 μm $\times$ 22 μm. It has epitaxial depth of 20μm (EEV). HPK devices are two-phase CCD, while EEV device is a three-phase CCD.

A CCD tracker was set up at the T1 test beam line of the 12-GeV proton synchrotron (PS) at High Energy Accelerator Research Organization (KEK) as shown in Fig. 11.1.2. The negative pion beam was used in the experiment. The momentum of the beam was chosen to be 2.0 GeV/c, 1.0 GeV/c, 0.7 GeV/c, and 0.5 GeV/c. The normal axis of the CCD tracker was aligned to the beam. The tracker consisted of four layers of CCDs as shown in the figure. First and second layers of CCDs are reference detectors for precise reconstruction of a particle track. The CCD in third layer is the sensor under test in this experiment. Another reference CCD was located at the end of the tracker for the reduction

Table 11.1: Test Samples.

Test sample	CCD type	Image area [mm]	Pixel pitch [μm]	Pixel format (H$\times$V)	Epitaxial layer [μm]	Amplifier sensitivity [μV/e]
HPK10	S5466	12.29$\times$12.29	24$\times$24	512$\times$512	10	2.0
HPK50	S5466(Special)	12.29$\times$12.29	24$\times$24	512$\times$512	50	2.0
EEV	CCD02-06	8.5$\times$12.7	22$\times$22	385$\times$578	20	1.0

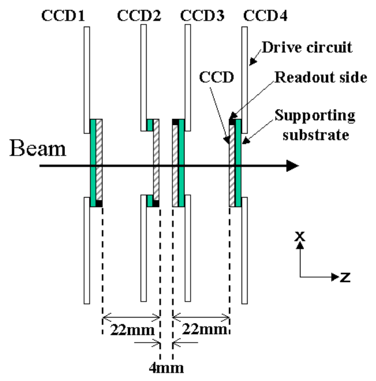

Figure 11.4: Schematic view of the setup. Both CCD1 and CCD2 were reference CCDs for tracking. CCD3 was the test sample. CCD4 was used for reduction of the accidental tracks, and the measurement of the efficiency.

of accidental tracks. The reference CCDs were HPK/S5466 with epitaxial depth of 10μm and were same type with HPK10. All of the CCDs were driven at a rate of 250 kpixels/s, and operated in a full-frame readout mode. The CCD's were read out every three seconds to synchronize with the PS cycle using 12-bit analog-to-digital converter(ADC). The sensitivities of the test samples including the gain of amplifier are 61.7$\pm$0.03μV/electron, 23.99$\pm$0.03μV/electron, and 34.63$\pm$0.02μV/electron, for HPK10, HPK50, and EEV, respectively. The details of this experiment is described in elsewhere [5].

Signal to Noise ratio

The charge created by a penetrating particle is collected generally by several consecutive pixels, which form a cluster. In order to find the cluster, we first look for a leading pixel whose charge is higher than the threshold and is highest in the adjacent 6$\times$6 pixel region. The threshold was defined as 13, 7, and 15 times of the noise level, for EEV, HPK10, and HPK50, respectively, in order to reduce the noise contribution with keeping the efficiency good.

Total charge of the cluster is sum of the charges of the leading pixel and neighboring pixels. Fig.11.1.2 shows a typical event of a minimum ionizing particle which was detected in HPK10.

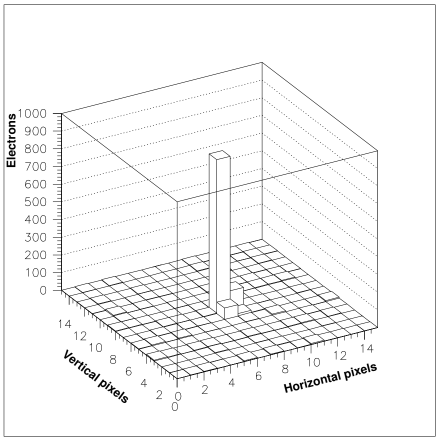

Figure 11.5: Typical event by a minimum ionizing particle detected in HPK10, where the height is a collected charge in the unit of electrons after the correction of the sensitivity of the detector including the gain of the amplifier.

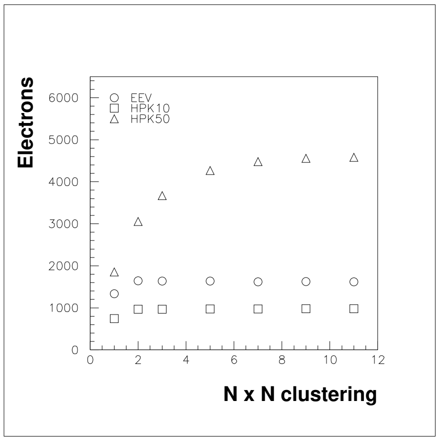

Figure 11.6: Collected charge for a minimum ionizing particle as a function of clustering size, where clustering size was defined as N×N pixels. The horizontal axis represents a number of N and vertical axis is a collected charge in the unit of electrons after the correction of the sensitivity of the detector including the gain of the amplifier.

Fig.11.1.2 shows clustering size dependence of the total charge at $-15°$C, where clustering size is defined as N×N pixels. As shown in the figure, almost all the deposited charges are collected in the cluster size of 2×2 pixels for HPK10 and EEV. For HPK50, however, more than 5×5 pixels are necessary to collect all of the deposited charges. Approximately 920 electrons/10μm [6] is expected to be produced by a minimum ionizing particle in silicon, which is consistent with the observed charge by taking into account the depth of epitaxial layers.

Fig.11.1.2 shows the temperature dependence of S/N for 2×2 pixel clustering. The S/N is defined as the most probable value of the collected signal charge distribution

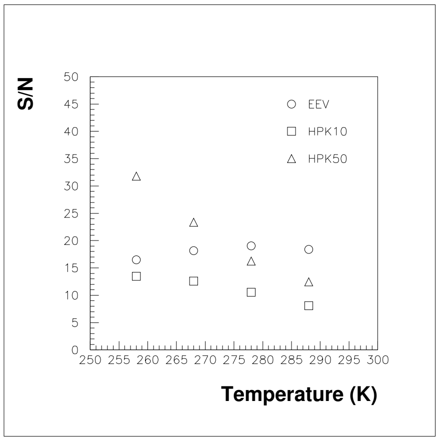

Figure 11.7: Signal-to-Noise ratio as a function of temperature, where clustering size was chosen to be 2×2 pixels. In this experiment, the CCD's were read out every three seconds to synchronize with the PS cycle. In the JLC project, however, the read out cycle of 6.7ms is planned. It is consequence of operating faster read out cycle that the noise due to dark current is suppressed and the S/N values are expected to improve significantly.

divided by the r.m.s of the noise charge distribution. As temperature is raised, the S/N for HPK CCDs significantly degraded due to the increase of the dark current, while the S/N of EEV has very small temperature dependence in the range from −15°C to +15°C. This is because the noise caused by the dark current is not a dominant source in the total noise for EEV. The main source is considered to be an external noise which comes from a cooling system. The degradation of the S/N for HPK50 in this range was larger than that for HPK10, since the dark current for HPK50 increases more rapidly than that for HPK10 as temperature rises. In the previous paper [7], the operational condition at higher temperature was discussed with the dependence of dark current on temperature and readout drive frequency. When CCD is driven at faster rate, the noise due to dark current is suppressed. Then, the S/N values are expected to improve.

Charge sharing and position determination

Since the charge sharing among adjacent pixels depends on the the hit position of the particle passing through the detector, it is possible to obtain better resolution by taking into account a charge sharing characterization which is the effect of the lateral charge diffusion. The position of the cluster was determined using the 2×2 pixels. In this report, we adopted two ways of determination for comparison.

- The Analog-Centroid method

  In the Analog-Centroid-Method (AC-method)[8], the hit position is reconstructed as the charge weighted average of the 2×2 pixels as

$$x = \frac{\Sigma Q_i X_i}{\Sigma Q_i}, \tag{11.2}$$

  where Q_i and X_i represent a charge deposit and pixel position defined at the center of i-th pixel, respectively. This method assumes a linear relation of charge deposit to the pixel position.

- The Ratio location mapping method

  In the Ratio-Location-Mapping method(RLM-method), the relation between the position x of the cluster and the charge ratio R_x of adjacent pixel was derived from the data, where x was calculated by extrapolating the track from the upstream reference CCDs and normalized by the pixel pitch. The R_x is defined using the charge deposit of adjacent two pixels as

$$R_x = \frac{Q_x}{Q_{max}}, \tag{11.3}$$

  where Q_{max} and Q_x are a charge deposited in the leading pixel and in the adjacent pixel to x-direction, respectively.

  Since the particle distribution within a pixel is uniform, we can assume dN/dx is constant, where N is a number of incoming particles. From this assumption, we can get the relation of x with R_x as $dx/dlog(R_x) \propto dN/dlog(R_x)$. Taking initial conditions as $x \to 0.0$ at $log(R_x) \to \infty$ and $x = 0.5$ at $log(R_x) = 1.0$, we obtain following formula,

$$x(log(R_x)) = \frac{0.5}{N} \int_{-\infty}^{log(R_x)} \frac{dN}{dlog(r)} dlog(r), \tag{11.4}$$

  where $dN/dlog(r)$ is a R_x distribution which is obtained from the data. The initial conditions correspond to the center of leading pixel, and the middle point of the gap between two pixels, respectively.

  Fig. 11.1.2(a) shows are data points derived by Eq.11.4 and RLM function obtained by fitting to the data with six order polinomial function. Fig. 11.1.2(b) shows a linear relation which is defined as $x = 0.5R_x$ and allowed region of the AC-method with 2×2 clustering which is obtained from Monte Carlo simulation.

  The position of the cluster was then calculated from the measured charge ratio by using the RLM function. The RLM function represents a spread of charges produced by incident particle. For example, if a particle hits the position x=0.3, the charge sharing to the adjacent pixel is about 8%, 13%, and 25% of the leading pixel, for EEV, HPK10, and HPK50, respectively. HPK50 has more spread signal than HPK10, since the epitaxial depth of HPK50 is larger than that of HPK10. The charge sharing of EEV is smallest among all samples. This reason is considered to be that the EEV has different structure from HPK type of CCDs.

  In the AC-method, the linear relation between the position of the cluster and the charge ratio of the four pixels is assumed. However, the relation between R_x and x is not linear as shown in Fig. 11.1.2. Therefore, we can expect to obtain the better position resolution by using the RLM-method.

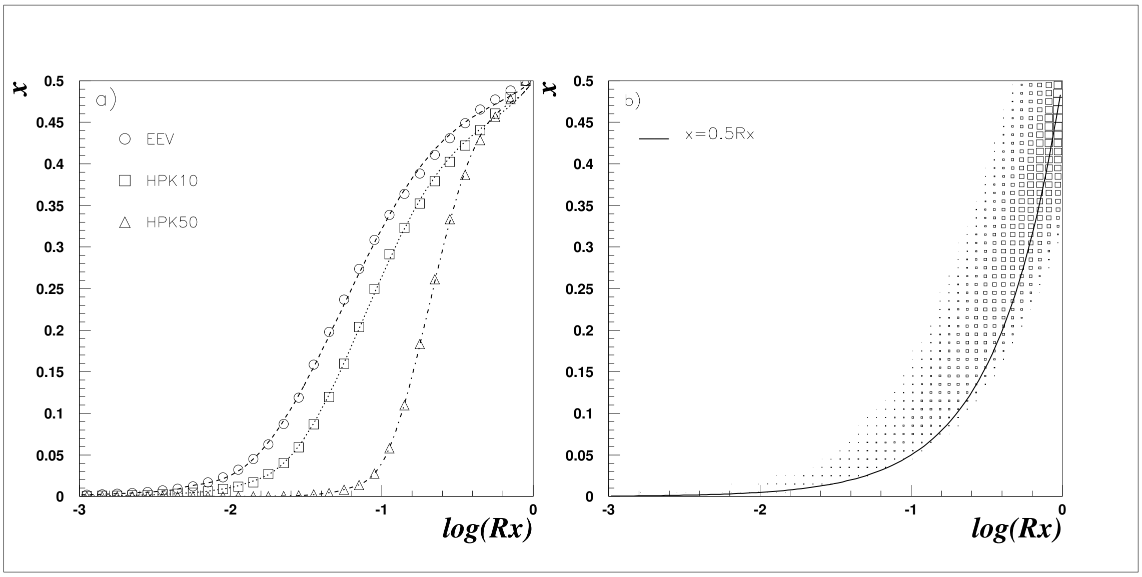

Figure 11.8: The relation of the cluster position x with the charge ratio R_x, where x is the position of the cluster normalized by pixel pitch. (a)RLM function, where symbols represent measured data and lines are obtained RLM function. (b)Linear function, where boxes region shows the allowed region of the AC-method which uses 2×2 pixels. Solid line represents a linear relation $x = 0.5R_x$.

Measured spatial resolution

The spatial resolution was derived from the residual distributions, which is the deviation of the cluster in the test sample from the extrapolated hit position from the upstream reference CCDs. The residual resolution (σ_{residual}) was obtained by fitting this distribution with the Gaussian distribution. The σ_{residual} contains the contributions from multiple Coulomb scattering (MCS) and the finite resolution of the reference CCDs. The MCS effect is suppressed by the factor $(\beta cp)^{-1}$, where βc and p is a velocity and momentum of incoming particle. We derived the residual resolution at infinite momentum by fitting the momentum dependence of residual resolutions with the function $\sigma_{\text{residual}} = \sqrt{A^2 + (B/\beta cp)^2}$, where A and B are fitting parameters, and A represents residual resolution at infinite momentum. Fig. 11.1.2 shows the momentum dependence of residual resolution with fit result.

Then the contribution from the ambiguity of the extrapolated hit position due to the finite resolution of the reference CCDs are estimated by taking the propagation of errors, and subtracted from the data. Here, we assumed spatial resolutions of reference CCDs were same as HPK10, because the reference CCDs were same type with HPK10.

The obtained spatial resolutions for normal incidence are listed in the Table 11.2, for the AC-method and the RLM-method, respectively. At -15°C, the spatial resolutions for HPK10 and EEV were improved about 20% by taking account the nonlinear charge sharing characteristics by the RLM-method. When the temperature was raised from -15°C to $+5$°C, the spatial resolutions obtained by using the RLM-method were changed its values according to the variation of the S/N value, i.e. about 20% worse for HPK10, and almost unchanged for EEV. On the other hand, the spatial resolutions derived from the AC-method were almost same, even if the temperature was changed from -15°C to $+5$°C.

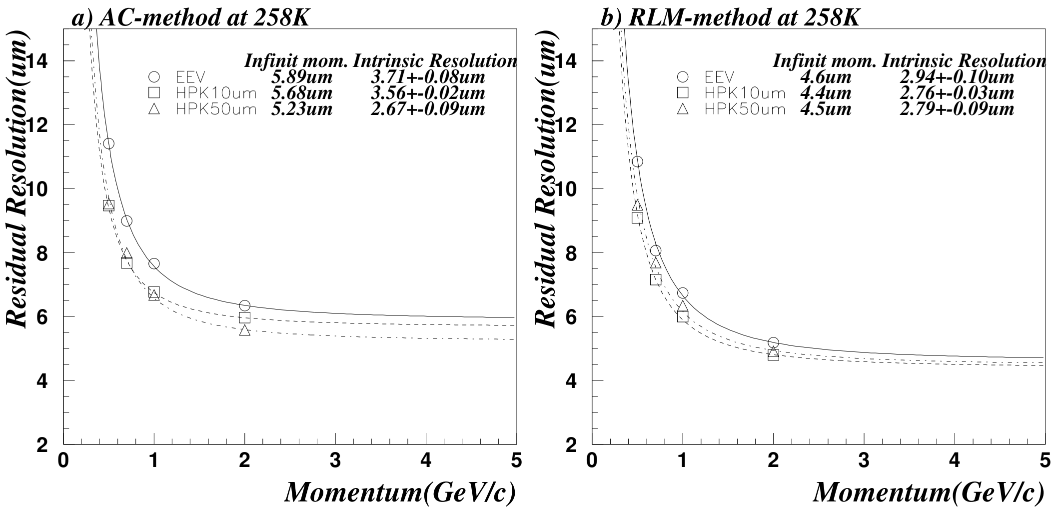

Figure 11.9: The momentum dependence of the residual resolutions for a)AC-method and b)RLM-method,respectively. The lines represents are result of fit to data.

Since the charge sharing is small in adjacent pixels for HPK10 and EEV, the resolution of R_x is deteriorated by the noise. This is the reason why the RLM-method is more sensitive to the S/N value than the AC-method. This conjecture explains the temperature dependence for HPK10 and EEV as well. For HPK50, the spatial resolutions obtained by the RLM-method and the AC-method were almost same value at both of -15°C and $+5$°C, because the RLM function is similar to the function in the AC-method as shown in Fig. 11.1.2(b). The spatial resolution become worsened about 30% if the temperature was raised from -15°C to $+5$°C. This is caused by the 50% degradation of S/N ratio.

Table 11.2: Spatial resolution in μm.

Temperature	Method	HPK10	HPK50	EEV
-15°C	AC	3.56±0.02	2.67±0.09	3.71±0.08
	RLM	2.76±0.03	2.79±0.09	2.94±0.10
$+5$°C	AC	3.68±0.03	3.34±0.10	3.84±0.08
	RLM	3.46±0.04	3.67±0.12	2.59±0.16

Efficiency

Efficiency was measured by looking for the existence of associated cluster in the interpolated region on the test sample, for the tracks which have a cluster in three reference CCDs. We require that the reference CCD at the end of tracker must have a associated cluster within 5 times of alignment errors from extrapolated hit position, for the reduction of the accidental tracks. The threshold for a leading pixel were applied as 13, 7, and 15 times of the noise level, for EEV, HPK10, and HPK50, respectively. Efficiencies at -15°C for 2 GeV pion were $98.8^{+1.2}_{-1.5}\%$, $99.4^{+0.6}_{-1.6}\%$, and $97.8^{+2.2}_{-1.6}\%$, for HPK10, HPK50, and EEV, respectively.

Discussion

- Signal-to-Noise dependence

  The result from test beam shows the degradation of the spatial resolution due to the increase of noise. We have estimated the influence of noise to the spatial resolution. The signals from CCDs are smeared with pseudo-noise that was generated according to the deviates drawn from a Gaussian distribution. Fig. 11.1.2 shows the dependence of the resolution on the 2×2 clustered signal-to-noise ratio. The RLM-method is sensitive to the S/N value, but it can improve resolution if the S/N is good enough. On the other hand, the AC-method is less sensitive to the S/N value than the RLM-method. In the case of EEV, the AC-method shows that the spatial resolution is almost unchanged even if the S/N is decreased from 19 to 7. The RLM-method requires the S/N about more than 10 for EEV and HPK10, to obtain better spatial resolution than the AC-method.

- Digitization resolution dependence

  An analog readout is a preferred solution for several reasons, including more effective monitoring of the stability of the detector properties and improvement in the spatial resolution. We need to know how many bits are required for quick extraction of the digitized information and reduction of the data size. We have investigated the spatial resolution by varying the digitization accuracy. Since we have used a 12-bit linear ADC for this experiment, we varied the digitization accuracy by using only higher bit information, while the dynamic range was unchanged.

  Fig. 11.1.2 shows the digitization accuracy dependence of spatial resolutions, for the RLM-method and the AC-method, respectively. The spatial resolutions are almost unchanged even if the digitization accuracy is reduced to 10 bits. If the accuracy was reduced less than 10 bits, the spatial resolution become worse. Fig. 11.1.2 shows the considerable event pattern and its observed pattern when the ADC accuracy is reduced. The worst spatial resolution at 6 bits is explained by the "symmetry" observed pattern that is described in Fig. 11.1.2(c). In this case, there is the ambiguity of choice of clustering. The cluster can be one of two types of clustering, and loose direction information. Fig. 11.1.2 shows the mean value of output signals in units of adc counts. The points shown in the figure are output level of horizontal over clock(HOC), dark charge which was derived with 12 bit resolution, the leading pixel in the cluster(P_{max}), the pixel which is the adjacent pixel to x-direction inside the cluster(P_x), and the pixel which is in the opposite side of the P_x(P_{opp}). We used average of HOC output as a baseline for calculation of the signals so that the HOC also affect to the other signal levels.

  As shown in the figure, P_x and P_{opp} is almost same as dark charges for EEV and HPK10, and is disappeared as reduction of adc resolution. Then the event type become single event.

  Both of P_x and P_{opp} are separated even at the 8 bit resolution for HPK50. However, at 6 bit resolution, both signals are recognize as identical , while those are separated from dark charge. This is the case of symmetry event type and loose the direction information.

In the case of AC-method, the signal used for position determination is defined by sum of two pixels. The reason for distortion of the spatial resolution at 6 and 4 bit adc accuracy for HPK50 is same as that of RLM-method. But the reason is quite different for the HPK10. The distortion of the spatial resolution at 6 bit, is due to the minus signal at the adjacent pixel. The calculated position become opposite to the correct position if the adjacent signals were minus values. While the calculated position constrain to center of the maximum pixel in RLM-method. Fig. 11.1.2a) shows the correlation of the ratio for cluster side and for the opposite side of the cluster for HPK50, and Fig. 11.1.2b) shows the residual resolution for HPK10.

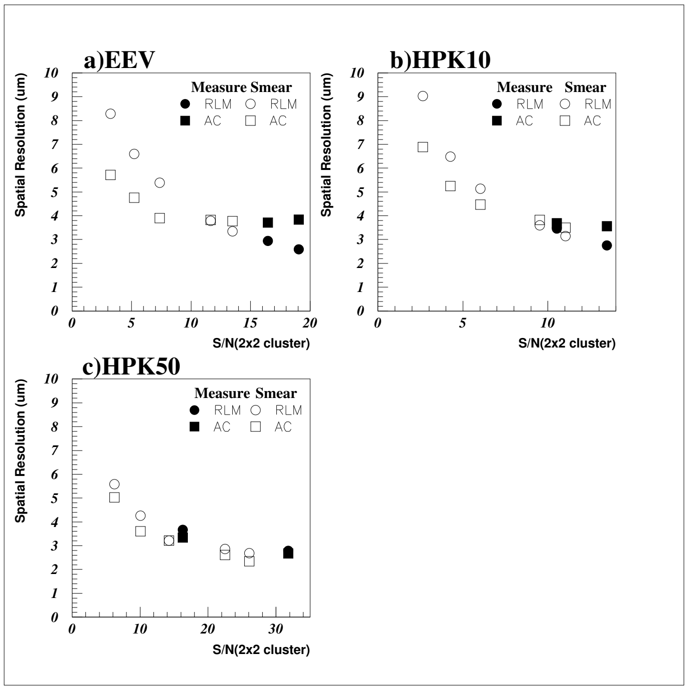

Figure 11.10: Signal to noise ratio dependence of spatial resolution for (a)EEV, (b)HPK10, and (c)HPK50, respectively. Black symbols represent the data measured at -15C° and +5C°. Open symbols represent the simulated data by smearing the data measured at -15C°.

Test with laser scanner system

The stability and excellent overall response of detector are well known. Less widely described is the fact that the internal structure of the pixel give rise to intra-pixel variations in response. These response modulations are particularly relevant to obtain the best spatial resolution.

We have made detail measurements of the response variations within a CCD, using a laser scanner system that gave a 2 micron resolution. Optical response of the CCD has been determined at all sample points within a pixel at wavelengths of 523 nm and 1064 nm whose absorption length is about 3 μm and 300 μm, respectively. Since the

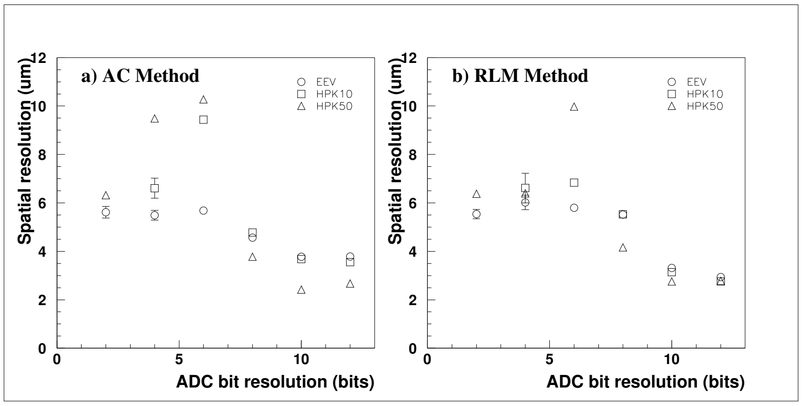

Figure 11.11: Digitization accuracy dependence of spatial resolution for (a)The RLM-method and (b)The AC-method, respectively.

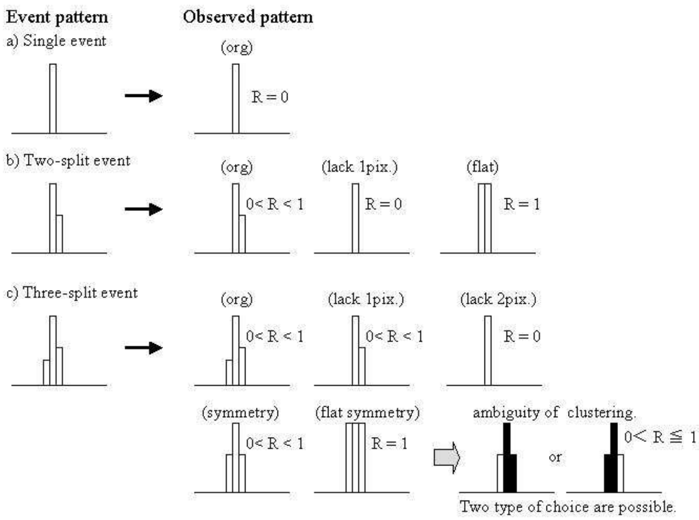

Figure 11.12: Considerable event pattern and its observed pattern.

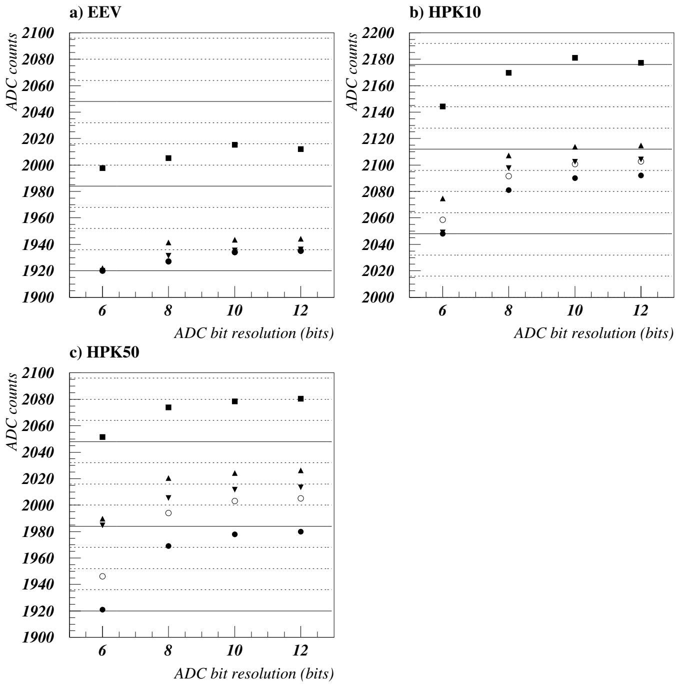

Figure 11.13: The mean value of output signals as a function of adc bit resolution, for the horizontal over clock(HOC) (black circle) which was used for the offset of the output, dark charge obtained with 12 bit accuracy (open circle), maximum signal in the cluster (black square), the signal used for the calculation of R (black triangle), and the signal of the pixel in the opposite direction of R (reversed black triangle). The solid and dashed lines represent 6 bit and 8 bit adc accuracy, respectively. For the EEV, dark charge is very small, i.e 0.14 adc counts, the output of dark charge is almost same with HOC.

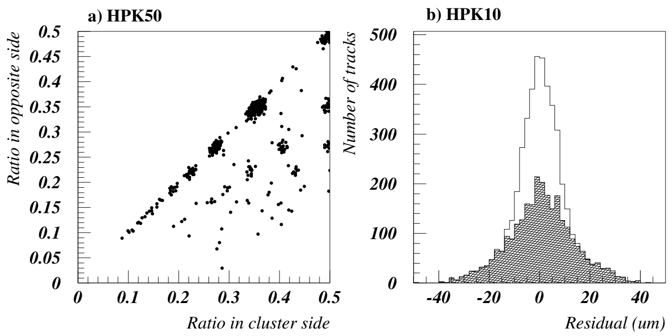

Figure 11.14: a) charge ratio of the cluster side and opposite of the cluster side for HPK50 at 6 bit adc resolution. b) The residual distribution for HPK10 at 6 bit adc resolution, where the open area represents a all tracks, and hatched area represents the tracks with minus value of the charge ratio.

thickness of the epitaxial layer of CCDs is typically 10∼50 μm, the pulsed laser of 1064 nm wavelength induces electron-hole pairs along the passage of the light nearly uniformly in a epitaxial layer of CCD. The Laser light of 1064 nm is suitable for simulating the signal generated by charged particles in a CCD.

Fig. 11.15 shows the schematic view of the experimental arrangement. The system consists of YAG laser, optics, xyz moving stage, and temperature box. A CCD is set on the xyz moving stage that can move with an accuracy of about 1μm. The CCD and xyz moving stage are in the temperature box, and kept at 0°C. The laser power is adjusted to simulate a pulse height of minimum ionizing particles by using ND filter. The spot size of laser light is about 2μm×2μm on the surface of a CCD. Fig. 11.1.2 shows the result of the measurement fro EEV. The charge ratio was calculated as signal charge in a pixel normalized by total charge of the cluster, where cluster was defined by adjacent three pixels. The result of 532 nm shows rather narrow charge sharing region, because of the short absorption length which makes the effect of the lateral charge diffusion small. We observed a broad charge sharing region with a triangle shape for 1064 nm. Also there is some different property in horizontal and vertical scanning. These results are used to investigate a charge sharing property and obtain a precise RLM-function. Also, this laser scanner system will be used for the calibration of the CCDs.

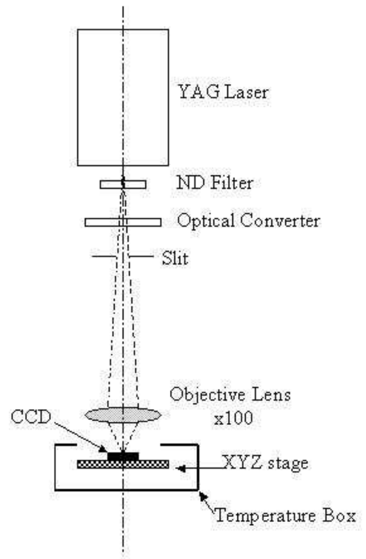

Figure 11.15: The schematic view of the laser scanner system.

Summary

We have studied the spatial resolution of a CCD. Three types of CCD detectors which have different structures were tested.

The present series of test showed that:

1) S/N ratio of more than 10 can be achieved even at +5°C and at accumulation time of 3 s including readout time, by successful operation in the MPP mode. In the JLC project, the readout cycle is much faster than this experiment. We expect the S/N become better, because noise due to the dark current is largely suppressed.

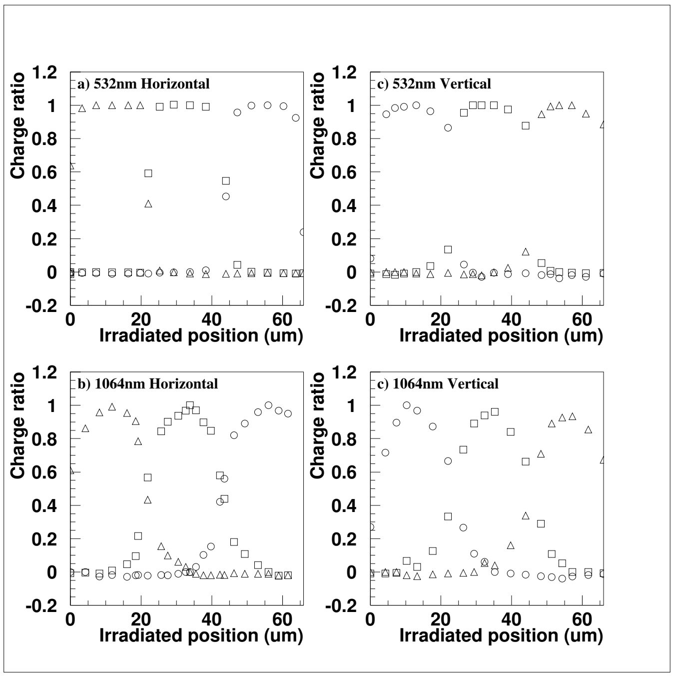

Figure 11.16: The charge sharing ratio for EEV. (a) and (b) show the charge ratio in the horizontal scanning with the wavelength of 532 nm and 1064 nm, respectively. (c) and (d) show same figures in the vertical scanning. The three sets of symbols are observed charge ratio on three adjacent pixels.

2) The spatial resolutions were improved for HPK10 and EEV by taking the nonlinear charge sharing characteristics into account by the RLM-method.

3) The temperature dependence of the spatial resolution in the AC-method was small for HPK10 and EEV samples, while spatial resolution become worse about 30% if the temperature was changed from $-15°$C to $+5°$C for HPK50.

4) The RLM-method needs S/N more than 10 for EEV and HPK10 to keep the spatial resolution better than the AC-method.

5) More than 10 bits digitization accuracy is needed to keep the spatial resolution better.

6) The precise measurement of the charge sharing property was studied using laser scanner system. This system will make it easier to measure CCD property.

11.1.3 Radiation Hardness of CCD Sensors

The backgrounds at the future LC pose significant challenges to the radiation hardness of CCD sensors. The main component of the background comes from e^+e^- pairs with estimated 10-year fluence of $\approx 1.5 \times 10^{12}$ cm^{-2}. Neutron background from (γ, n) reactions is also present, reaching $\approx 5 \times 10^9$ cm^{-2} for the same period. The electron background is expected to affect mainly the CCDs in the innermost layer, because it is closest to the beam pipe. The neutron irradiation is almost uniformly distributed in the volume of the vertex detector and affects all CCD chips.

Study of commercially available CCDs is required to build a model for the radiation damage effects, which can be used for estimation of the device lifetime in the expected environment. Radiation hardness studies of CCDs can provide valuable information on the preferable device architecture, chip geometry and operating conditions, which ultimately determine the vertex detector design, performance and cost. Much of this study was concentrated on the device application at **near-room** temperature because of the advantages of this operation. Operation at low temperatures is usually required to suppress the radiation damage effects in CCDs [9]. By avoiding cooling to cryogenic temperatures it is possible to decrease the thermal distortions of the supporting CCD ladders and to simplify their design, which results in better detector geometry and increased measurement precision. Although attractive from designer's point of view, operation at elevated temperatures faces problems from radiation damage effects, which are addressed in this study.

Both surface and bulk damage effects are expected to take place in the CCD sensors because of the type and the energy spectrum of the radiation background. Ionizing radiation creates electron-hole pairs in silicon dioxide, which is used as gate and field dielectric in CCDs. Charge carriers drift in the electric field (externally applied of built-in) to the corresponding electrode. Electrons quickly reach the positive electrode, but some of the holes remain trapped in the oxide and give rise to radiation-induced trapped positive oxide charge, which can be stable for long time. At any Si-SiO_2 interface there are a number of interface traps, which result from the strained or dangling silicon bonds at the boundary between the two materials. Ionizing radiation causes the density of these traps to increase, generating radiation-induced interface traps. The formation of radiation-induced trapped oxide charge (or flat band voltage shift) and interface traps is referred under the term **surface damage**.

Radiation with sufficiently high energy can displace Si atoms from their lattice positions, creating displacement damage. This process affects the properties of the bulk semiconductor and is known as **bulk damage**. Low energy electrons and X-rays can deliver only small energy to the recoil Si atom and mainly isolated displacements, or point defects, can be created. On the other hand, heavier particles, such as protons and neutrons can knock out silicon atoms which have sufficient energy to displace other atoms in the crystal. The secondary displacements form defect clusters, which have high local defect density and can be tens of nanometers wide. Defect clusters often have complicated behavior and more damaging effect on the properties of semiconductor devices than point defects. The energy threshold for displacement of a Si atom has been estimated to be about 260 keV for electrons and 190 eV for neutrons, therefore in the expected radiation environment bulk defects can be generated by both particles. Cluster damage is also expected, because the threshold for cluster production is known to be $\approx$5 MeV and $\approx$15 keV for electrons and neutrons [10], respectively.

Trapped holes in the oxides change the parameters of MOS structures in a way identical to applying an external voltage to the gates. Small flat band voltage shifts, in the order of few volts, can be accommodated by adjustment of the amplitude of the gate bias and drive voltages. A limitation may arise from the maximum allowed power dissipation in the gate drivers and in the CCD chip, because the dissipated power is proportional to the voltage amplitude squared. If the flat band voltage shifts are higher, the device can stop to function properly because of parasitic charge injection from the input structures, incomplete reset of the output node or distortion of the shape of the potential wells [11]. However, as long as no parasitic effects from the increased pulse amplitudes appear, the shifts are not a limitation for the device operation.

Interface traps are the dominant source of dark current in modern CCDs, because the generation rate at the Si-SiO_2 interface is usually higher than that in the epitaxial bulk silicon. Increase of the surface dark current is the main effect expected from radiation-induced interface defects.

Radiation-induced bulk defects cause the dark current in CCDs to increase, which is well known phenomenon [12] [13]. Dark current is an issue only for near-room temperature operation or long integration times, because it can be reduced to negligible values by cooling. Irradiation with heavy particles (e.g. protons, neutrons) often creates large non-uniformities in the dark current spatial distribution in the CCDs [14]. These non-uniformities, also known as "dark current spikes" or "hot pixels" manifest themselves as pixels with much higher dark current than the average value for the CCD. Their presence has been connected with the high electric fields caused by the device architecture and field-enhanced emission, the cluster nature of the radiation damage and crystal strains in the silicon material. Dark current spikes have big consequences for high temperature applications. Additionally, some of them show random fluctuations of the generated current, or Random Telegraph Signals (RTS) [15].

Another important bulk damage effect is the loss of signal charge during transfer, or Charge-Transfer Inefficiency (CTI). Charge losses occur when bulk defects capture electrons and emit them at a later moment, so that the released charge cannot join the original signal packet from which it has been trapped. The basic mechanism can be explained by the different time constants and temperature dependencies of the electron capture and emission processes. In the presence of bulk defects electrons are trapped with a capture time constant of τ_c and consequently released with an emission time constant of τ_e. For a defect at energy position E_t below the conduction band the Shockley-Read-Hall theory gives

$$\tau_e = \frac{1}{\sigma_n X_n v_{th} N_c} \exp\left(\frac{E_t}{kT}\right) \tag{11.5}$$

and

$$\tau_c = \frac{1}{\sigma_n v_{th} n_s}, \tag{11.6}$$

where

σ_n = electron capture cross section,
X_n = entropy change factor by electron emission,
v_{th} = thermal velocity for electrons,
N_c = density of states in the conduction band,
k = Boltzmann's constant,
T = absolute temperature,
n_s = density of signal charge.

The capture time constant is typically of the order of several hundred nanoseconds and has weak temperature dependence, whereas the emission time constant changes many orders of magnitude because of the exponential temperature behavior. At low temperature the defects can be considered almost permanently occupied with electrons, because the emission time constant of the defects can be very large, of the order of seconds. The defects cannot capture signal electrons and the CTI at low temperature is small. At high temperature the emission time constant becomes small and comparable with the charge shift time. Trapped electrons are able to join their signal packet, because most of them are emitted already during the charge shift time, and charge losses are small. At temperatures between the two extremes these is a peak of the CTI value.

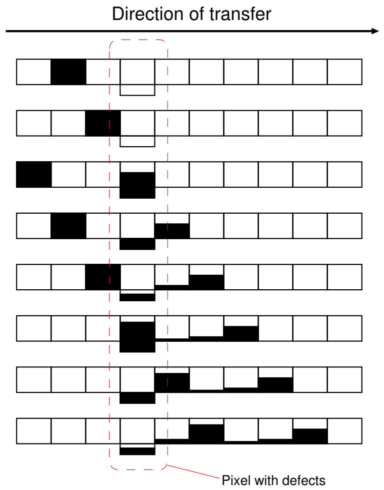

Figure 11.17: Schematic representation of the mechanism of charge transfer losses. For simplicity it has been assumed, that only one pixel contains defects.

The mechanism of charge transfer losses is illustrated on Fig. 11.1.3. When the signal packet encounters traps, some of its electrons are captured and later released. Those electrons, which are released in the trailing pixels do not join their original signal packet and account for the CTI. If a charge packet enters a pixel, in which part of the traps are occupied, less signal electrons can be trapped and therefore less charge can be lost.

We are often interested not only in the CTI value, but in the total losses the charge suffers after all the transfers it takes to reach the output. For a generated charge C_{gen}, transferred n times, the output charge C_{out} is given by

$$C_{out} = C_{gen}(1 - CTI)^n. \tag{11.7}$$

This dependence shows, that CTI and the number of transfers are the two important parameters that need to be considered for minimizing the charge transfer losses.

For near-room temperature applications one is particularly concerned with the dark current of the CCD sensors. Multi Pinned Phase (MPP) mode CCDs [16] were used in our experiments because they feature much lower dark current than standard devices. In MPP CCDs the Si-SiO_2 interface is biased into inversion and populated with holes, leading to suppression of the carrier generation from interface defects. With the surface inverted, only bulk defects contribute to the dark current. Since in contemporary buried channel CCDs current generation from defects at the Si-SiO_2 interface is dominant, MPP mode operation can reduce the device dark current by more than one order of magnitude. This method has the ability to suppress the dark current from the interface states formed during irradiation and can offer increased radiation hardness [17].

The radiation hardness of two types of buried channel, MPP mode CCDs was studied. The S5466 CCD, manufactured by Hamamatsu Photonics is 2-phase device with 10μm epitaxial layer and 512×512 active pixels with size 24μm×24μm. Three other types of S5466-based CCDs were studied, including high speed device (10 Mpix/s), notch CCD and device with SiO_2-Si_3N_4-SiO_2 gate (ONO) dielectric. A three-phase CCD, manufactured by EEV Ltd. was investigated as well. The device CCD02-06 has 20μm epitaxial layer and 385×578 active pixels with size 22μm×22μm.

Several devices were exposed to electron irradiation from a ^{90}Sr source and 2 CCDs were irradiated by neutrons from a ^{252}Cf source. The change of the voltage needed to achieve MPP mode operation was used as a measure of the flat band voltage shifts. The dark current of the devices was measured in the temperature range from −100°C to +20°C by averaging the dark charge over several frames. The CTI of the horizontal (serial) and the vertical (parallel) registers of the CCD was measured in the same temperature range by observing the charge and the position of isolated pixel events (IPE), created by the 5.9 keV Mn-K_α line of a ^{55}Fe source. After sufficient averaging, the dark signal of each pixel was stored into memory and this dark frame was then subtracted pixel by pixel during the X-ray exposure. The readout speed was usually 250 kpixels/s. For the high-speed Hamamatsu CCD the speed was raised to 2 Mpixels/s.

The change of the MPP threshold voltage in electron-irradiated S5466 CCD, irradiated unbiased, is shown on Fig. 11.18. Due to the SiO_2-Si_3N_4 gate dielectric in the EEV devices, the change of the MPP threshold is slightly smaller than than in Hamamatsu CCDs. In biased and clocked S5466 CCD higher shift was observed (Fig.11.19), which is explained by the lower ratio of recombining holes in biased oxides. The flat band voltage shifts were estimated to be 0.02 V/krad for unbiased devices and 0.07 V/krad for biased Hamamatsu CCDs. The flat band voltage shift of electron-irradiated Hamamatsu ONO CCD was also measured, however it was higher that in standard S5466 devices, on the contrary to the expectations. In neutron-irradiated devices such shifts were not expected and were not observed.

The dark current in MPP mode in both electron and neutron irradiated devices increased after irradiation, which is attributed to creation of bulk traps. The CCD demonstrates effective suppression of the surface component of the dark current by almost 3 orders of magnitude (Figs. 11.18 and 11.19) when $|V_{ee}^{V}| > |V_{ee}^{MPP}|$ and the interface is populated with holes. In that condition the dark current is limited by carrier generation in the bulk.

Spurious dark charge, which was superimposed on the bulk current, was observed in electron irradiated Hamamatsu CCDs. This spurious current, which was named "dark current pedestal" (DCP) does not depend on the accumulation time of the readout cycle [18]. Because it is produced by the clocking, dark current measurements are not affected. However, the DCP provides background charge in the CCD and decreases the measured CTI through the "fat zero" effect. It was found, that the spurious current was caused by impact ionization by holes, returning to the channel stops and to the adjacent gates after the surface potential has been switched from inversion to depletion [19]. The temperature dependence of the DCP is shown on Fig. 11.20. In the low temperature region holes are provided by tunneling from near-interface traps, while at higher temperatures carriers

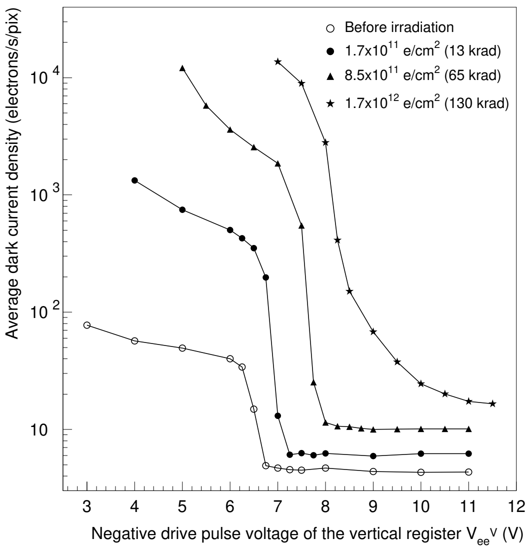

Figure 11.18: Average dark current density as a function of the electron irradiation fluence and of the negative drive pulse voltage V_{ee}^{V} at T = −26°C. The device #JS14/026 is irradiated unbiased.

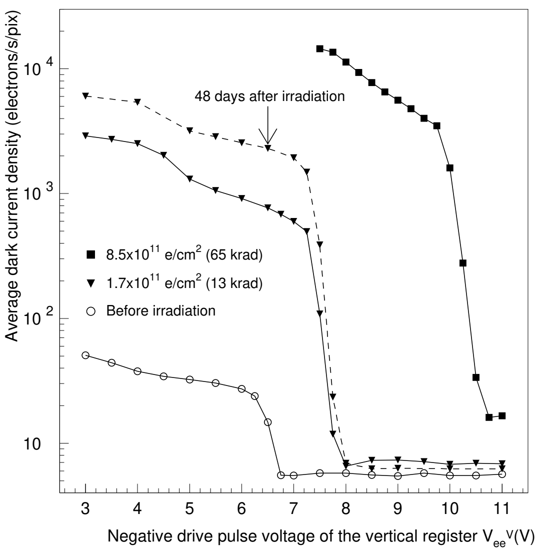

Figure 11.19: Average dark current density as a function of the electron irradiation fluence and of the negative drive pulse voltage V_{ee}^{V} at T = −26°C. The device #JS8/053 was biased and clocked during irradiation.

are released by thermal excitation from interface defects. The DCP severely limits the application of Hamamatsu devices because it is much larger than the bulk dark current at the same temperature.

Investigation of dark current spikes was performed on both Hamamatsu and EEV devices, which showed very similar results. No increase of the dark current non-uniformities was observed in electron irradiated devices (Fig. 11.21(a)–11.21(d)). Neutron irradiated CCDs however, showed significant creation of dark current spikes (Fig. 11.21(e)) after irradiation with fluence as low as 2.4×10^8 neutrons/cm^2. After subtraction of the dark frame pixel by pixel, the resulting distribution (Fig. 11.21(f)) is close to that of a electron-irradiated CCD. This subtraction shows an efficient way to correct for the large dark current non-uniformities in CCDs, irradiated by heavy particles. During operation, the dark current map should be updated regularly to include the contribution of the newly created defects.

Random telegraph signals (RTS) were observed in many hot pixels when their current was recorded for sufficiently long time (Fig. 11.22). During the typical time, required for one CTI measurement (≈ 5 min), these fluctuations are difficult to notice and they have small effect on the subtraction of the dark frame. In a long time scale, it is not possible to correct for the dark current of such pixels as was shown on Fig. 11.21 because of the random fluctuations of the pixel current. The RTS can generate false signals, similar to those created by X-rays or MIPs, and can be a source of erroneous track reconstruction. A measurement to find isolated pixel events, caused by RTS was performed on Hamamatsu and EEV CCDs, with similar results. The number of false IPE greatly depends on the

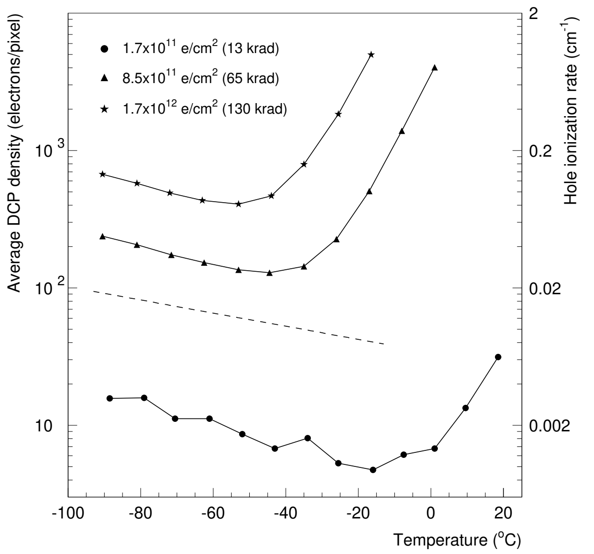

Figure 11.20: Temperature dependence of the average DCP density in device #JS14/026 as a function of the electron irradiation. Dashed line shows the calculated temperature dependence of the hole ionization rate at 10^5 V/cm.

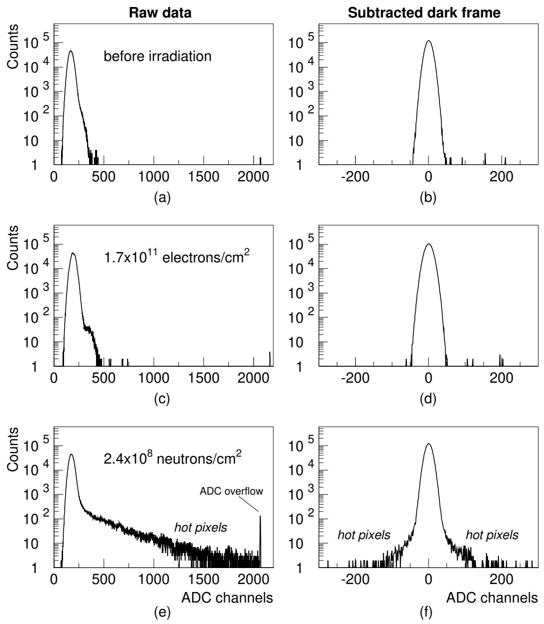

Figure 11.21: Dark current distribution at $+10°$C in S5466 CCDs before irradiation (a), (b); in an electron irradiated to $1.7{\times}10^{11}$ cm^{-2} CCD (c), (d); and in a neutron irradiated to 2.4×10^8 cm^{-2} CCD (e), (f). The gain is $\approx$ 6.0 electrons/ADC channel.

threshold, which is imposed for the search of signal. The same threshold of 600 electrons, used for the CTI measurements was employed in the measurement. The ratio of false IPE per CCD readout frame (i.e. the pixel occupancy), caused by RTS is shown on Fig. 11.23. The RTS amplitude depends on the temperature and the integration time t_i and these 2 parameters were varied during the measurement. Although about 40% of the hot pixels exhibit RTS, most of them are rejected by the applied threshold for IPE search. When the integration time is short, a ratio of false IPE signals of less than 10^{-4} can be achieved even in the temperature range above 0°C.

Much attention was paid to the measurement of radiation-induced CTI, because it is the main factor that requires low temperature operation [9]. A model for the charge transfer in 2- and 3-phase CCDs was developed [19], which allows one to calculate the CTI as a function of the temperature, timing of the transfer, concentration of background charges, signal size and pixel occupancy.

The results from the CTI measurements on electron irradiated S5466 CCD, together with modeled results are shown on Fig. 11.24. Modeling was performed using the experimental values of the dark current and of the DCP, presented in the previous paragraphs. The modeling on electron irradiated CCDs showed that a trap at $E_c{-}0.37$ eV with σ_n $= 4{\times}10^{-15}$ cm^2 is responsible for the observed increase of the vertical CTI. Additional pre-irradiation defect was identified at $E_c{-}0.44$ eV. The energy position of the main defect, derived from the model, varies between $E_c{-}0.37$ eV and $E_c{-}0.39$ eV in three samples. The simulated results on Fig. 11.24 are based on the presence of two traps at

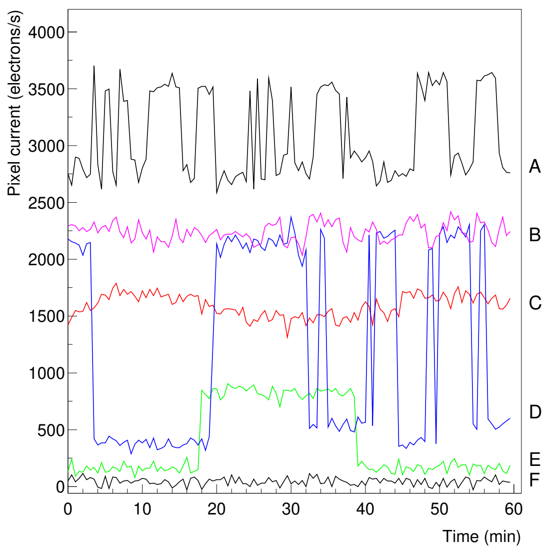

Figure 11.22: Time variation of the dark current at -1.6°C in hot pixels, showing RTS behavior. The measurement was carried out on Notch CCD #P4 1-5B1-4, irradiated to 5.7×10^9 neutrons/cm^2. Pixel F is normal (not "hot"), is plotted for reference.

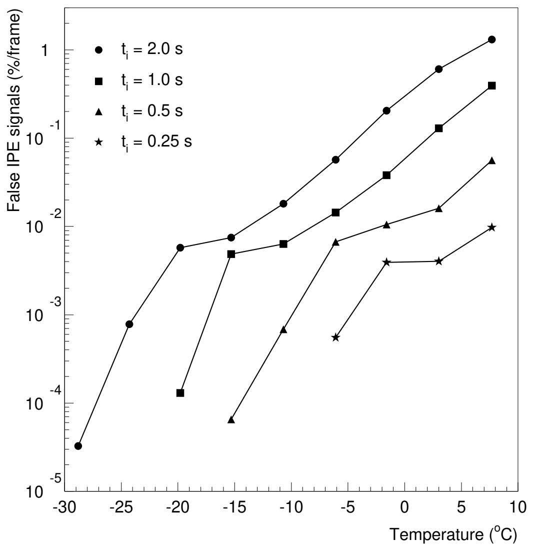

Figure 11.23: Ratio of false IPE per CCD frame, caused by RTS, at 4 different integration times t_i. The measurement was performed on Notch CCD #P4 1-5B1-4, irradiated to 5.7×10^9 neutrons/cm^2. The threshold is set at 600 electrons.

E$_c-$0.37 eV and E$_c-$0.44 eV. The concentration of the trap at E$_c-$0.44 eV, obtained from the model increases insignificantly under irradiation. The CTI of the horizontal register is less than 10^{-4} in the whole temperature range. As explained by the model, the peak in the HCTI, which would have occurred at high temperatures is suppressed by the dark current pedestal and the exponentially increasing dark current.

Similar result was obtained in electron-irradiated EEV CCD, however the VCTI in that device was about 4 times higher than in S5466 devices. Numerical simulations showed, that under equal conditions the 3-phase CCDs has about 2.5 times larger CTI than 2-phase devices, because of the higher signal density in 2-phase CCDs. The greater than expected difference can be explained mostly by the DCP in Hamamatsu devices, which decreases the measured CTI values by the "fat zero effect" [18]. Two-phase devices are superior to 3-phase CCDs in term of CTI and should be preferred for applications in radiation environment.

The VCTI of neutron-irradiated to 8.9×10^9 cm^{-2} S5466 CCD is about 4×10^{-4}, and VCTI peak of 3×10^{-4} was measured in an EEV CCD, irradiated with approximately the same fluence. The same defect at E$_c-$0.37 eV, derived from the model, was found responsible for the CTI increase in neutron-irradiated devices. In all CCDs the HCTI is significantly smaller than the VCTI, which is explained by the different timing of the transfer in the registers.

The defect at E$_c-$0.37 eV was identified from annealing studies and additional measurements as contribution from both E and $V-V^-$ centers [19]. The E center, which anneals out at 150°C was found to be dominant, contributing to $\approx$ 60% of the CTI peak. The measured energy position of the defects is reduced by the Frenkel-Pool effect. This

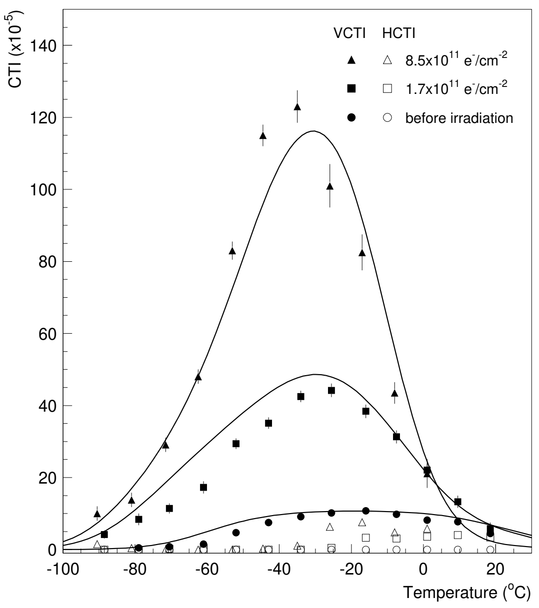

Figure 11.24: CTI as a function of the temperature and of the electron irradiation fluence in S5466 CCD. Symbols are the experimental data; solid lines represent the modeled VCTI for the combination of two traps at $E_c-0.37$ eV and $E_c-0.44$ eV.

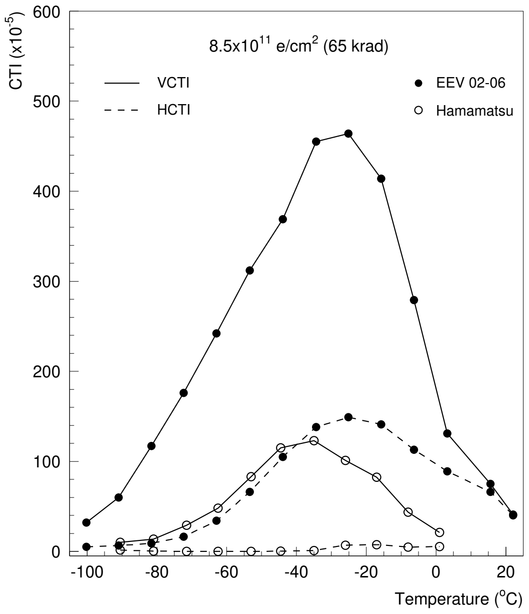

Figure 11.25: CTI of 2-phase (Hamamatsu S5466) and 3-phase (EEV CCD02-06) electron-irradiated CCDs.

effect is also responsible for the thermal activation of the dark current in most of the hot pixels.

Modeling showed, that in the accumulated 10-year background from e^+e^- pairs of 1.5×10^{12} cm^{-2} the VCTI will reach 1.5×10^{-1} in 3-phase EEV-like CCD. Safe margin is included in this calculation by considering the bulk damage from e^+e^- pairs to be 10 times larger than that from ^{90}Sr electrons. Neutron-induced CTI is much smaller than those generated by electrons, and only the latter is being considered. Such a high CTI value is unacceptable, because the charge will be lost only after a few transfers. Measures have to be taken to decrease the VCTI, including better CCD design and appropriate device operating conditions, in order to extend the lifetime of the CCDs.

One important method to improve the CTI is to use an additional narrow implant in the CCD channel (Fig. 11.26). This implant forms a sub-channel, or "notch" in the potential profile of the transport channel, confining the signal charge into a fraction of the pixel volume. CTI depends on the concentration of signal electrons n_s as

$$CTI \propto n_t/n_s, \tag{11.8}$$

where n_t is the defect concentration, therefore increasing the signal density by forcing the same charge into a smaller volume can improve the CTI.

The radiation-induced CTI was measured in electron- and neutron-irradiated notch CCD, based on the S5466 design. Due to the additional 3μm-wide notch channel, its CTI

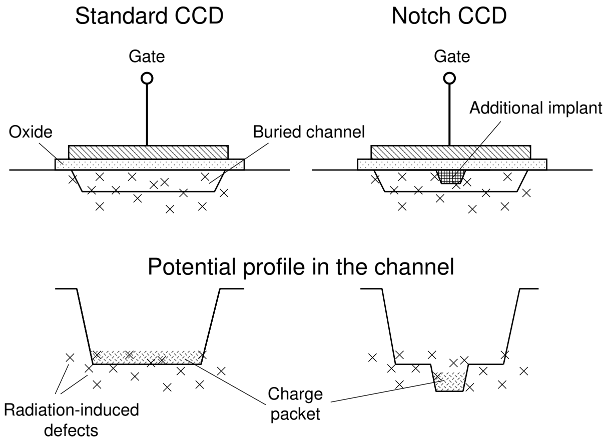

Figure 11.26: Schematic and potential profile in the channel of standard and notch CCD.

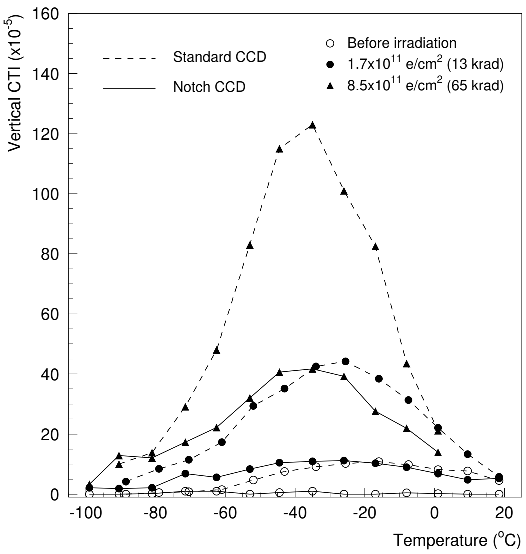

Figure 11.27: CTI of notch and standard S5466 CCDs.

is about 3 times lower than that in conventional S5466 device (Fig. 11.27). In neutron-irradiated to 5.7×10^9 cm^{-2} notch CCD the peak CTI was below 10^{-4}.

A calculation of the frequency dependence of the CTI was carried out to study the possible improvement by varying the readout speed of the CCDs. At speeds higher than several Mpix/s, horizontal CTI decreases rapidly because charge dwell time becomes shorter than the capture time constant of the defects. Vertical CTI is much less influenced, because charge spends longer time in the imaging section. Increasing the readout speed has relatively small ability to control the the VCTI and other methods to reduce it should be chosen. At high readout speed the horizontal CTI becomes more than an order of magnitude smaller than the VCTI.

It was not possible to back this calculation by experimental data from the high-speed Hamamatsu CCD, because of the dependence of the DCP on the width of the shift pulses [19]. The frequency dependence of the CTI was masked by the “fat zero” effect from the DCP and a definite conclusion could not be drawn.

One of the most powerful methods, that can be used for CTI improvement is injecting of a sacrificial charge, or “fat zero” into the CCD registers. This charge reduces the CTI in two ways: by increasing the signal charge density (11.8), as it is transported together with the signal; and most importantly, by filling the traps in front of the signal packet, so that less electrons can be captured.

Experimental and theoretical studies several devices have shown, that the CTI of the vertical register dominates the charge losses in the CCD. Introducing additional charge in the vertical register through the injection port is not a trivial task because of the large non-uniformity of the injected charge [20]. We have developed another method to inject “fat zero”, which employs the dark current characteristics of MPP mode CCDs. By varying the negative gate bias voltage of the vertical register V_{ee}, the CCD can be

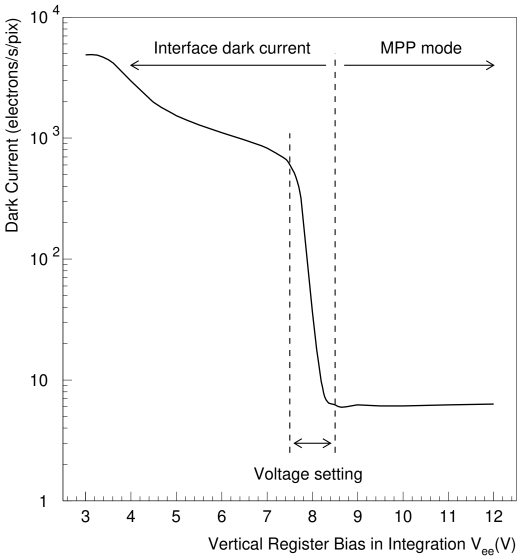

Figure 11.28: Principle of thermal "fat zero" generation in MPP mode CCDs.

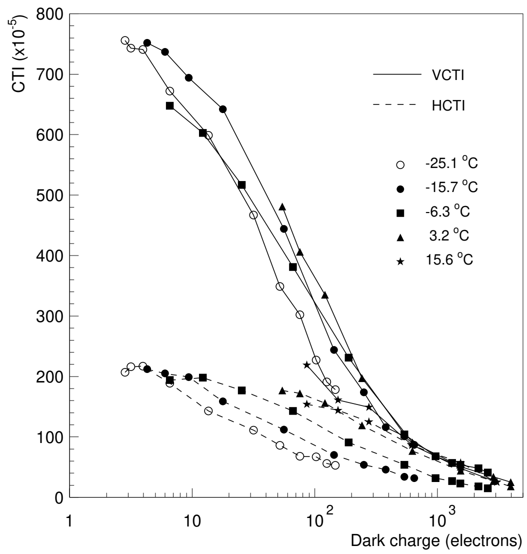

Figure 11.29: Measurement of CTI reduction by "fat zero" effect in EEV CCD02-06.

driven into semi-MPP mode and its dark current can be controlled between the MPP mode value and ≈100 times that value (Fig. 11.28). At high temperatures, this current can be sufficient to provide charge of the order of 1000 electrons even if the CCD readout cycle is very short. The proposed method works on any type of MPP CCD, because the "fat zero" is generated thermally. The amount of injected charge can be controlled either by adjusting the V_{ee}, or by setting V_{ee} to some low value and adjusting the time, during which the CCD is out of MPP mode. Practical implementation of the proposed method depends on the irradiation level and requires precise adjustment.

Another important feature of this method is that it has the ability to self-adjust for non-uniformities of surface damage. If in some pixels the flat band voltage shift is higher, corresponding to higher surface and bulk damage, the interface component of the dark current will be higher than for the rest of the CCDs at the same setting of V_{ee}. Therefore, larger dark current is generated automatically, which compensates for the higher CTI in those pixels.

The experimental data on Fig. 11.29 is obtained by changing the V_{ee} voltage. It shows, that the CTI can be reduced several times by injecting "fat zero" of approximately 1000 electrons, which is almost half the number of signal electrons. The additional charge increases the noise of the device, however this does not degrade the performance of the high-speed CCDs, for which the readout noise is of the order of $100e^-$ RMS. Estimations of the radiation-induced dark current after receiving combined electron and neutron irradiation at the expected 10-year levels show that dark current generation of > 1000 electrons can be achieved by this method at temperatures > 5°C and integration time of 6.7 ms.

As shown in the previous paragraphs, the VCTI is the main point of concern, because the HCTI can be reduced to less than 10% of VCTI. Using all the options for CTI improvement described above, the VCTI can be reduced more than 60 times, as shown in Table 11.3. However, this may not be sufficient, and the number of transfers in the vertical direction (i.e., the vertical chip size) may have to be reduced in accordance with (11.7) to limit the charge losses.

Table 11.3: Vertical CTI improvements.

Option	VCTI improvement
Raise the output speed to >5 Mpix/s	≈1.3 times
Use 2-phase CCD	≈2.5 times
Use notch CCD	3 to 4 times
Inject "fat zero" >1000 e^-	6 to 8 times
Total improvement	≈ 60 to 100 times

Speaking only of the CTI, the CCD lifetime in a radiation environment depends on the chosen value of charge transfer losses. Some example parameters of the CCD can be calculated if 25% lost charge is considered acceptable and the HCTI is taken as 10% of the VCTI. As was mentioned before, the VCTI of a 3-phase EEV-like CCD is expected to reach 1.5×10^{-1} after 10 years of operation in the radiation environment of the future linear collider. A CCD, which contains 2 Mpixels and 12 outputs, each reading 250 vertical and 667 horizontal pixels, will have 23% transfer losses after ≈3 years of operation. Although all the measures from Table 11.3 with improvement of 60 are applied in this calculation, the main contribution (18%) comes from the VCTI. Assuming pixel size of 24μm, the chip has dimensions 96mm×12mm, and can be read out completely between two pulses (6.7 ms) at 25 Mpix/s.

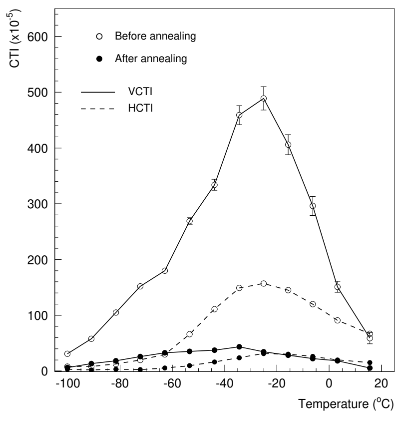

Figure 11.30: Temperature dependence of the CTI in electron-irradiated to 8.5×10^{11} cm^{-2} EEV CCD02-06 (#A4003-18) before and after annealing at 150°C for 2 hours.

Another possible method for reduction of the radiation-induced CTI is device annealing. It is known, that the $P - V$ center, which is the dominant bulk defect in n-type buried channel CCDs [15] anneals at about 150°C. By periodically heating of the CCD it is possible to restore the pre-irradiation CTI, provided that the mechanical support and mounting are designed to withstand such a temperature cycle.

An annealing experiment was performed on both electron irradiated Hamamatsu and EEV devices [21]. In the EEV chip the CTI decreased almost to its pre-irradiation level after 2 hours at 150°C (Fig. 11.1.3). Similar experiment on a Hamamatsu device showed CTI improvement of about 60%.

Conclusions

The most important results from the radiation damage studies of CCDs can be summarized as follows:

- The radiation hardness of 2- and 3-phase MPP mode CCDs from different manufacturers has been extensively studied;
- A model for the charge transfer losses in the CCDs has been developed and applied in good agreement with the experimental data;
- Two-phase, notch CCDs should be used because of the greatly reduced CTI in comparison to 3-phase and standard devices;
- Thermal charge injection is the major factor for reducing the CTI and promises successful near-room operation in harsh radiation environment;
- Device annealing can be used for restoring the CTI to sufficiently low levels. It can be performed periodically when the detector is not working;
- Large flat band voltage shifts and spurious dark charge in Hamamatsu CCDs are the main limitations at the moment. These issuies can be solved by more advanced radiation-hard devices, currently under development.

11.2 Intermediate Tracker

11.3 Forward Tracker

11.4 Central Tracker

11.4.1 Overview of CDC

We start our discussion with general design principle of a central tracker in order to translate the physics requirements to concrete chamber parameters. A possible set of chamber parameters for the central tracker is given according to the general design principle. We then list up our R&D items that include mechanical and operational stability issues, feasibility studies of required chamber performance, and effects of space charge and magnetic field. Finally we summarize our R&D and discuss future direction.

11.4.2 Design principle

Outline of Geometrical Parameters Decision Process

The parameters that determine the geometrical configuration of a small-jet-cell cylindrical drift chamber can be classified into two groups: (1) global parameters that specify the size and layout of axial and stereo super-layers, and (2) local parameters that describe the geometry of a jet cell in each super-layer. The first class includes the length, the inner and outer radii, and the stereo angle[1] of each super-layer. If there is a layer of shielding wires between adjacent super-layers, its radius and stereo angle also belong to this class. The parameters in the second class are, essentially, the relative locations of wires that comprise a single jet cell, and determine the local properties of the chamber. These parameters are optimized to achieve performance goals such as required spatial resolution, two-hit separation capability, etc, together with other non-geometrical parameters including wire high voltages, gas mixture, magnetic field, and so on.

Basic Chamber Parameters in Terms of Physics Requirements

Now let us outline a typical parameters decision process. The chamber performance goals required by physics of interest are often expressed in terms of transverse momentum resolution, dip angle resolution, two-track separation capability, polar angle coverage, etc. In our case the most stringent requirement comes from the recoil mass measurement for $e^+e^- \to Zh$ followed by $Z \to l^+l^-$. In order to confirm the narrowness of the Higgs boson, the recoil mass against the lepton pair from the Z decay should be measured to an accuracy only limited by the natural beam energy spread. This sets the following performance goal for the momentum measurement: $\sigma_{p_{l^\pm}}/p_{l^\pm} \lesssim 0.4$ % at $p_{l^\pm} = 50$ GeV. Separation of W and Z through jet invariant mass measurements demands a resolution comparable with the gauge boson natural widths. This necessitates good track-cluster matching: $\sigma_Z \simeq 1$ mm and 2-track separation better than 2 mm.

The transverse momentum resolution σ_{p_T} is approximately given by the following formula[26]:

$$\frac{\sigma_{p_T}}{p_T} \simeq \sqrt{\left(\frac{\alpha' \sigma_{r\phi}}{Bl^2}\right)^2 \left(\frac{720}{n+4}\right) {p_T}^2 + \left(\frac{\alpha' C}{Bl}\right)^2 \left(\frac{10}{7}\left(\frac{X}{X_0}\right)\right)}, \tag{11.9}$$

where

$$\left\{ \begin{array}{lll} \sigma_{r\phi} & = & \text{spatial resolution in the } r\text{-}\phi \text{ plane per wire} \\ n & = & \text{the number of sampling points} \\ \alpha' & = & 333.56\ (\mathrm{cm \cdot T \cdot GeV^{-1}}) \\ C & = & 0.0141\ (\mathrm{GeV}) \\ (X/X_0) & = & \text{thickness measured in radiation length units} \\ l & = & \text{lever arm length (cm)} \\ B & = & \text{magnetic field (T)} \end{array} \right. . \tag{11.10}$$

The number of sampling points is practically determined by the lever arm length and the minimum possible wire-to-wire distance. The best result is thus expected for the

[1]Strictly speaking, stereo angle, which is defined as the wire angle measured from the axial direction, slightly varies even within a single jet cell: it increases linearly with the radial position of a wire. As discussed later, the stereo angle of the innermost wire is the most important in deciding the stereo geometry.

largest possible B field and lever arm length with the smallest possible spatial resolution. Since the required polar angle coverage determines the wire length when the lever arm length and the radial position of the innermost wires are given, the lever arm length is limited by the maximum possible wire length for stable chamber operation[2]. The B field essentially determines the Lorentz angle given a chamber gas mixture[25] and, if a tilted cell structure is adopted, it imposes a limit on the two-hit separation capability. There will also be a technical limit to the maximum possible B field attainable with a superconducting solenoid from the mechanical strength and the stored energy to be released upon quench.

On the other hand, the dip angle resolution $\sigma_{\tan\lambda}$ can be written in the form[26]:

$$\sigma_{\tan\lambda} \simeq \sqrt{\left(\frac{\sigma_z}{l}\right)^2 \left(\frac{12}{n}\right) + (1+\tan^2\lambda)\left(\frac{C}{p_T}\right)^2 \left(\frac{13}{35}\left(\frac{X}{X_0}\right)\right)}, \tag{11.11}$$

where σ_z is the spatial resolution per wire in the axial direction which is given by

$$\sigma_z = \sigma_{r\phi}/\tan\alpha \tag{11.12}$$

in the case of stereo wires with a stereo angle α. Provided that l and B are predetermined by the requirement on the transverse momentum resolution, the only free parameter left here is the stereo angle. Apparently the larger the stereo angle becomes the better the dip angle resolution. There are, however, various restrictions to the stereo angle which are the main topics of this paper.

The two-hit separation capability is controlled by the width of a sense wire signal which is determined by the arrival time distribution of track electrons, space charge effects in the avalanche formation, and the subsequent readout electronics. Apart from the optimization of the readout electronics, appropriate choices of the drift line configuration and chamber gas are thus important. In any case, the relation of the two-hit separation capability issue to the stereo geometry is at most indirect and can be treated separately as a problem concerning local properties of the chamber[27].

Stereo Wires and Super-layer Structure

At this point we have a rough idea about basic parameters describing the chamber: the inner and outer radii, the length, the number of sampling points, and the $r\phi$ spatial resolution per wire. In order to decide the stereo geometry, we further need to know the super-layer layout of the chamber and problems introduced by the use of finite stereo angles. A stereo layer can be formed by rotating the end point of each wire belonging to this layer by a small angle ($\Delta\phi$) with the other end point fixed. As illustrated in Fig.11.31, the stereo angle α is related to $\Delta\phi$ and the wire length (L) through

$$\begin{aligned} \alpha &= \tan^{-1}\left(\frac{2r(z=\pm L/2)}{L}\sin\left(\frac{\Delta\phi}{2}\right)\right) \\ &\simeq \frac{r(z=\pm L/2)}{L}\cdot\Delta\phi, \end{aligned} \tag{11.13}$$

[2]There are some external constraints on the radial positions of the inner- and outermost wires: the radial position of the innermost wires is constrained, in the case of the present JLC design, by the size of the support tube for the final focusing quadripole magnets that reside in the detector system. The radial position of the outermost wires has to be consistent with the surrounding barrel calorimeter.

which suggests α being r-dependent even within a single stereo jet cell as mentioned earlier.

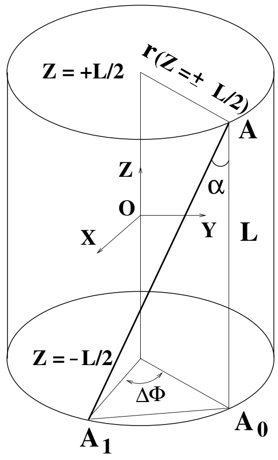

Figure 11.31: 3-dimensional view of a single stereo wire.

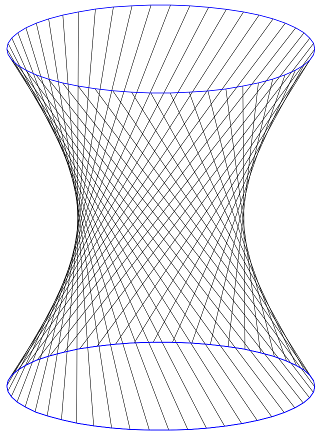

Figure 11.32: Formation of a hyperboloidal surface due to stereo wires.

The otherwise cylindrical surface of this wire layer turns into a hyperboloidal surface as shown in Fig.11.32. As a result, both the azimuthal angle and the radial position of the stereo wire becomes z-dependent:

$$\begin{aligned} \phi(z) &= \phi(z=0) + \tan^{-1}\left[\left(\frac{2z}{L}\right)\tan\left(\frac{\Delta\phi}{2}\right)\right] \\ r(z) &= \sqrt{\left(r(z=0)\right)^2 + \left(z\tan\alpha\right)^2} \\ &= \sqrt{\left(r(z=\pm L/2)\right)^2 + (z^2-(L/2)^2)\tan^2\alpha}, \end{aligned} \tag{11.14}$$

where z is measured from the middle of the chamber along the chamber axis [3].

This inhomogeneity distorts the electric field to some extent and limits the maximum possible stereo angle, thereby restricting the z resolution σ_z. Fig.11.33 demonstrates how a single stereo cell structure deforms as one moves from one endplate to the other. This z-dependent geometrical deformation of the stereo cell is parametrized by a so called shrink factor and imposes another important restriction on the possible range of stereo angles.

The shrink factor $f(z)$ is defined to be the ratio $A_2B_2(z)/AB(z=\pm L/2)$ in Fig.11.33

[3]The azimuthal wire position becomes a linear function, and the radial wire position a quadratic function of z measured from the middle of the chamber:

$$\left\{ \begin{array}{lcl} \phi(z) & \simeq & \phi(z=0) + \left(\frac{\alpha z}{r(z=0)}\right) \\ r(z) & \simeq & r(z=0) + \frac{1}{2}\left(\frac{(\alpha z)^2}{r(z=0)}\right) \end{array} \right. \tag{11.15}$$

to the lowest order of αz.

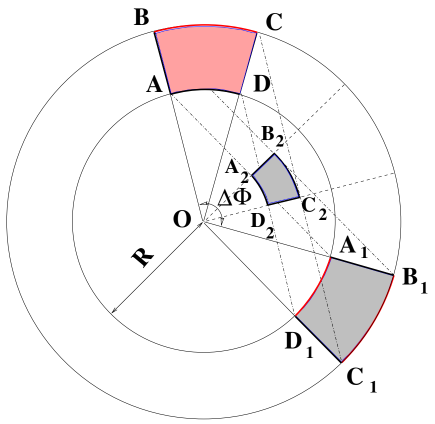

Figure 11.33: Exaggerated illustration of the stereo-cell formation through rotation by an angle $\Delta\phi$ and its deformation along the wires. $ABCD$ and $A_1B_1C_1D_1$ are the cross sections of a single stereo cell at the end plates ($z = \pm L/2$). $A_2B_2C_2D_2$ is that of the same stereo cell inbetween ($-L/2 \ < \ Z < \ +L/2$).

and is readily derived from Eqs.11.13 and 11.14:

$$\begin{aligned} f(z) &= \frac{r_B(z) - r_A(z)}{r_B(z = \pm L/2) - r_A(z = \pm L/2)} \\ &= \sqrt{1 + \left(\frac{z^2 - (L/2)^2}{L^2}\right) 4\sin^2\left(\frac{\Delta\phi}{2}\right)} \\ &= \frac{\sqrt{R^2 + (z^2 - (L/2)^2)\tan^2\alpha}}{R}, \end{aligned} \tag{11.16}$$

where $R = r(z = \pm L/2)$ and $f(z = \pm L/2) = 1$ by definition.

It is a common practice to use pairs of stereo super-layers (V and U) with alternating stereo angles ($\pm\alpha$) interleaved with axial super-layers (A)[4]. In this case, the inhomogeneity is more serious for the gap between a stereo super-layer (V) and the adjacent axial super-layer (A) just inside. The minimum gap attained at the middle point of the chamber has to be large enough for stable operations of the chamber.

11.4.3 A Possible Central Tracker

Chamber Design

Applying the general design principle explained above to the JLC case, we obtained the following basic parameters for a possible JLC central tracker: $B = 2\ T$, $r_{in} = 45$ cm, $r_{out} = 230$ cm, $L = 460$ cm, $n = 80$, and $\sigma_{r\phi} = 100\ \mu$m. The tracker consists of 6 axial and 10 stereo super-layers, each having 5 anode wires, arranged with increasing r in the following order: $AVUAVUAVUAVUA$, where A, V, and U again denote an axial

[4]The axial super-layers greatly facilitate track finding in the r-ϕ projection, since stereo super-layers alone cannot provide any absolute coordinate before its z coordinate is determined through tracking. There is, however, a logical possibility to do away with axial layers.

super-layer, stereo super-layers with stereo angles of $+\alpha$ and $-\alpha$, respectively. The gap between adjacent super-layers is correlated with the stereo angle and is equal to either 4.0 or 5.0 cm at the endplates, depending on its radial location: the U-to-A and the V-to-U gaps are equal to 4.0 cm, while the A-to-V is set at 5.0 cm (see Fig.11.34)[5].

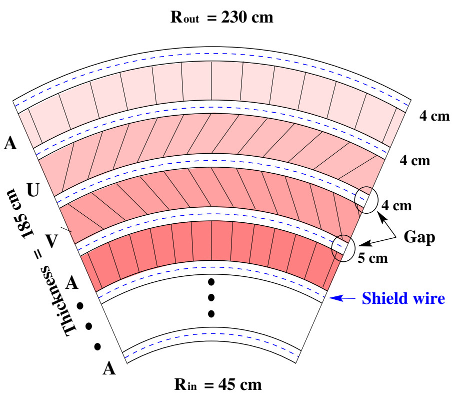

Figure 11.34: A possible super-layer layout for the central tracking system of the JLC.

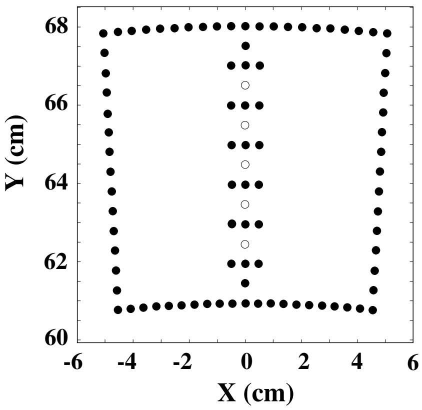

Figure 11.35: A typical geometry of a single cell: the circles (○) and (●) correspond to sense and potential wires, respectively.

In the current design, there is a layer of shielding wires in each gap between adjacent super-layers, in order to electrostatically isolate different super-layers. These shielding wires in a V-to-U gap will have the same stereo angle (α) with the V wires. On the other hand, the shielding wires in A-to-V or U-to-A gaps will have half the stereo angle of the adjacent stereo super-layers ($\pm\alpha/2$). Note also that the stereo angle varies even within a single jet cell, according to Eq.11.13.

A possible cell design is shown in Fig. 11.35. The cell has 5 sense wires spaced 1 cm, with each surrounded by ground wires in the sense wire plane and grid wires placed 5 mm away from it. The two dummy sense wires at the both ends of the sense wire plane are placed to stabilize the upper- and the lower-most sense wires. The maximum drift length depends on the radial position of each sense wire and has a typical value of 5 cm. The drift field is produced by 10 field shaping wires whose potentials change linearly. The high voltages on the wires will be chosen so as to get as uniform a drift field as possible with minimum electrostatic forces, while keeping a reasonable gas gain for a chamber gas mixture of 90%CO_2 and 10% Isobutane.

Questions to be Answered

The chamber parameters described above lead us to the following list of questions:

1. Can we control gravitational and electrostatic sags for 4.6m-long wires?
2. Is tension drop controllable for Al wires?
3. Can we stably operate 4.6m-long stereo cells?

[5]We can further optimize the inter-super-layer distances.

4. Can we achieve a spatial resolution of 85μm everywhere in this big chamber?

5. Can we achieve 2-track separation better than 2mm?

6. Is gas gain saturation observed for cool gas mixtures no problem?

7. Is Lorentz angle small enough to allow straight cells?

8. Is neutron background ($\sim$2k hits/train for $B = 2$T[33]) no problem? How big is the signal charge for a single neutron hit? Is there any dead time expected?

These questions naturally comprise our R&D items.

Let us begin with the first two questions which have to do with mechanical stability of the chamber.

Mechanical Stability

Figure 11.36: 4.6 m CDC test chamber with wire position measurement system.

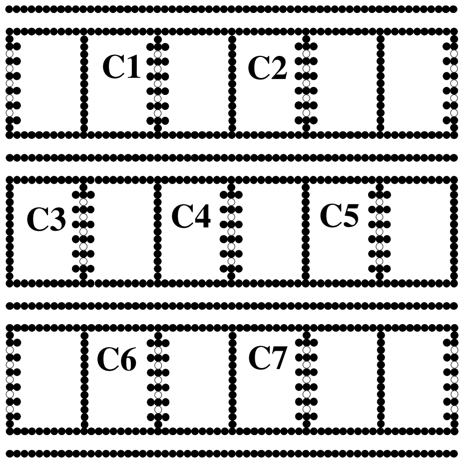

Figure 11.37: Cell layout of our 4.6 m long test chamber.

In order to investigate mechanical stability of a drift chamber with very long wires, we have built a 4.6 m long test chamber (see Fig. 11.36). We have also been developing a software program to predict wire displacement, knowing the cell structure, wire tension, and high voltage on each wire. The validity of the prediction has to be proved experimentally. We have developed a wire tension and position measurement system and measured wire tensions, gravitational and electrostatic sags for the 4.6 m long test chamber. The results of the measurements were then compared with the predictions.

Our 4.6 m long test chamber has seven identical cells with the cell parameters which approximate those of the aforementioned possible JLC central tracker. The layout of the seven cells is shown in Fig. 11.37.

The cell design is shown in Fig. 11.38-(a) which also specifies our wire naming convention to be used hereafter. The cell has 5 sense wires ($S1$ to $S5$) held at 2.5 kV and spaced 1 cm, with each surrounded by ground wires ($G1$ to $G6$) in the sense wire plane and grid wires ($GL1$ to $GL6$ and $GR1$ to $GR6$) at -0.5 kV placed 5 mm away from it.

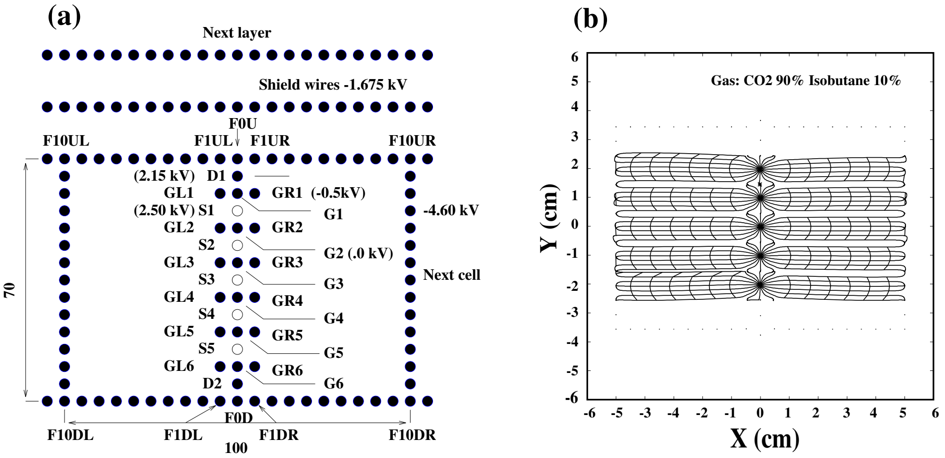

Figure 11.38: (a) possible mini-jet cell structure and (b) corresponding drift lines.

The two dummy sense wires ($D1$ and $D2$) at the both ends of the sense wire plane are held at 2.15 kV and stabilize the upper- and the lower-most sense wires ($S1$ and $S5$). The maximum drift length is 5 cm where the drift field is produced by 10 field shaping wires ($F1{*}{*}$ to $F10{*}{*}$) whose potentials change linearly in this order from -0.5 kV to -4.6 kV, and by left and right edge field wires held at -4.6 kV. The wire diameter is 30 μm for sense wires and 125 μm for the others. The high voltages on the wires were chosen so as to get as uniform a drift field as possible with minimum electrostatic forces, while keeping a reasonable gas gain for a chamber gas mixture of 90%CO_2 and 10% Isobutane. Fig. 11.38-(b) plots the drift lines calculated with a drift chamber simulation program GARFIELD [30].

Unless otherwise stated, wires we are going to deal with belong to the central cell ($C4$).

Before stringing wires, we surveyed the endplates to check their machining precision and found that the standard deviation of the actual wire hole positions from the nominal ones to be less than 8.2 μm. The sense wires are gold-plated tungsten and all the other wires are gold-plated aluminum. The reason for this choice of Al as the wire material is to minimize the total wire tension so as to reduce the thickness of the chamber endplates as required by endcap calorimeters. The wire stringing took us three weeks.

Gravitational and Electrostatic Sags

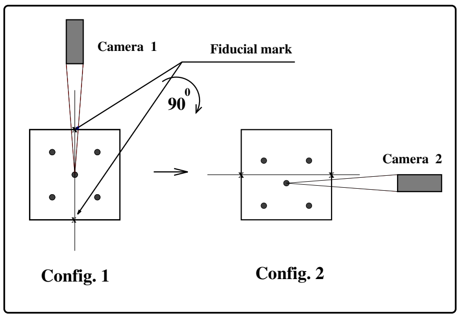

Figure 11.39: Principle of gravitational sag measurements

Fig. 11.39 illustrates our measurement scheme of the gravitational sag of a wire. The

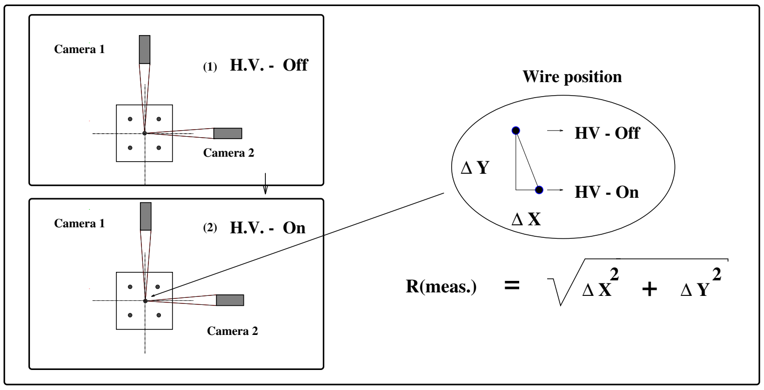

Figure 11.40: Schematic view of the electrostatic sag measurements.

measurement goes as follows. Using the vertical camera, we first put fiducial marks on the chamber windows in such a way that the line connecting them passes through the wire in question (configuration 1 in Fig. 11.39). Then we rotate the test chamber by 90° and determine the wire deflection due to gravitational sag by measuring the wire position relative to the line connecting the fiducial marks, using the horizontal camera (config.2 in Fig. 11.39).

We measured the gravitational sags 1.5 years after the wire stringing. The average gravitational sags for field and sense wires were 600μm and 353μm, respectively.

Our measurement scheme of electrostatic sag is sketched in Fig. 11.40. We first get a wire in sight on both the horizontal and vertical cameras with high voltages off. Then we measure the horizontal (ΔX) and vertical (ΔY) displacements in the camera screens after turning on the high voltages. Notice that the camera stays at rest during the measurement and the measurement accuracy is determined completely by the wire image resolutions on the screens (there is no tilt angle effect here). The overall accuracy for the electric sag measurement was estimated to be 5 μm. The wire stability in the electrostatic field has been checked by turning on and off the high voltages several times. We found no instability, meaning that the wires always return to the same positions of equilibrium.

Figs.11.41 and 11.42 illustrate the wire deflections in our 4.6 m test chamber due to gravitational and electrostatic forces. In the figures an *original position* ($\bigtriangledown$) is the initial position of a wire at the end plates. On the other hand, denoted as *gravitational sag* ($\square$) and *electric sag* ($\star$) are the measured positions of the wire under the gravitational force *before* and *after* applying high voltages, respectively. Called first iteration ($\circ$) is the calculated value of the wire deflection in the electrostatic field when other wires are at the positions after the gravitational sags. The input parameters for the second iteration ($\bullet$) are the new wire positions from iteration 1.

In Fig.11.41 we compare the measurements and predictions for a few field wires which are on the left and right sides of the sense wire plane. There is a good agreement not only in the magnitude of deflection but also in its direction for each one of these field wires. It is clear that the prediction from the second iteration is better.

Results of the predictions and measurements for sense wires $S1$ and $S2$ are shown in Fig.11.42. There is a noticeable left-right asymmetry in the measurements with respect to the original sense wire plane, which could not be reproduced by the calculation. Probably the source of such an asymmetry can be attributed to the influence of the other cells which might have some asymmetry in wire tensions, since they were strung over a finite period of time.

Wire Tension Drop Problem

Almost all methods of wire tension measurements are based on the same basic principle [28] and ours is no exception. We excite oscillations of a wire at its resonant frequency, and then determine the tension T by using the following relation:

$$T = 4\rho \cdot L^2 \cdot f^2, \tag{11.17}$$

where f is the fundamental resonant frequency. The results are shown in Figs. 11.43-(a) and -(b) for field and sense wires, respectively, as functions of the time measured from the day of wire stringing. There is still a tension drop of about 10%/year for gold-plated Al field wires unlike gold-plated W sense wires which now reach a tension plateau. Since this poses a potential problem and requires a better wire material, we are continuing wire material studies.

We now move on to question 3 which is the operational stability issue discussed in detail in [24] [29].

Operational Stability

Surface Field Variation Due to Stereo Wires

As shown earlier, the wires belonging to a stereo layer form a hyperboloidal surface. Consequently, any stereo cell shrinks as one moves from an endplate to the middle of the wires. The resultant shrink factor is shown in Fig.11.44 for all of the 10 (V,U) stereo super-layers of the possible JLC central tracking system.

The variation of the shrink factor $\Delta f/f$ is at most 3 % observed for the innermost stereo super-layer which has $r = 68$ cm and $\alpha = 75$ mrad. The z-dependent geometrical deformation of the stereo cell induces variation of the surface field on the sense wires in it, thereby introducing gain nonuniformity along the wires. We calculated the surface field variation on the sense wires, using the drift chamber simulation program, GARFIELD. The size of the cell structure depends on the shrink factor f and varies also with the radial position or the super-layer that the cell belongs to.

Fig.11.45 plots the calculated surface fields against the z coordinate. The maximum variation of the surface field is $\Delta E/E \simeq 0.43$ %.

Surface Field Variation Due to Wire Sags

In addition to the stereo geometry, there is another source of geometrical deformation of the cell structure that is the wire sags due to gravitational and electrostatic forces on the wire. These gravitational and electrostatic sags also contribute to the surface field variation and are common to both axial and stereo wires. It suffices to investigate the effects of these wire sags for axial wires only. We, therefore, calculate the surface field variation with GARFIELD, using as input the electrostatic and gravitational sags actually measured as the difference of the wire coordinates at $z = \pm L/2$ (wire ends) and $z = 0$ (mid point) for a 4.6 m-long test chamber[22]. The maximum wire-sag-induced variation of the surface field is $\Delta E_0/E_0 \simeq 1.4$ %. It should be emphasized that the fact that the field variation is comparable with those from the stereo geometry for our example is largely due to the use of Aluminum field wires. We can in principle reduce the field variation from the gravitational and electrostatic sags, by optimizing the wire materials

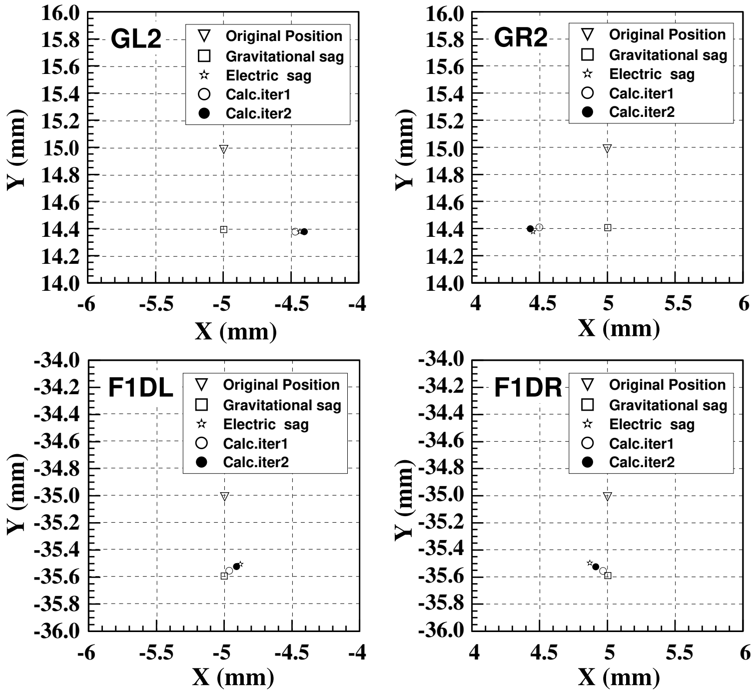

Figure 11.41: Measured positions of some representative field wires at the endplates ($\bigtriangledown$), with gravitational sags ($\square$) before and ($\star$) after electrostatic sags, compared with calculations: iterations 1($\circ$) and 2 ($\bullet$).

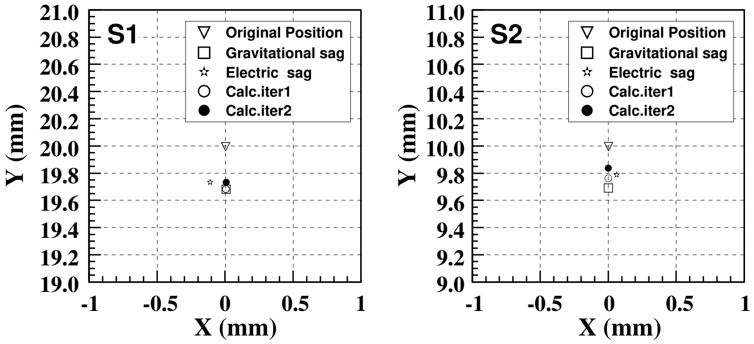

Figure 11.42: Same as Fig. 9 for the worst ($S1$) and a typical ($S2$) sense wires.

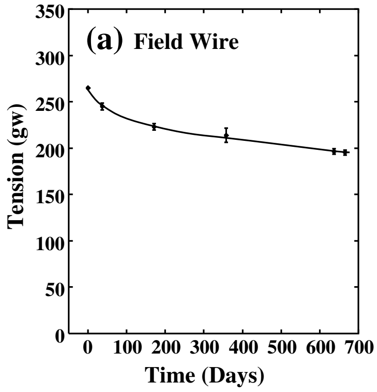

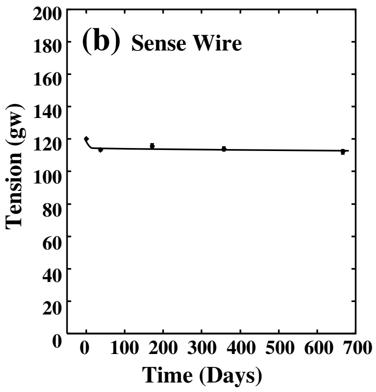

Figure 11.43: Tension versus time for (a) field and (b) sense wires

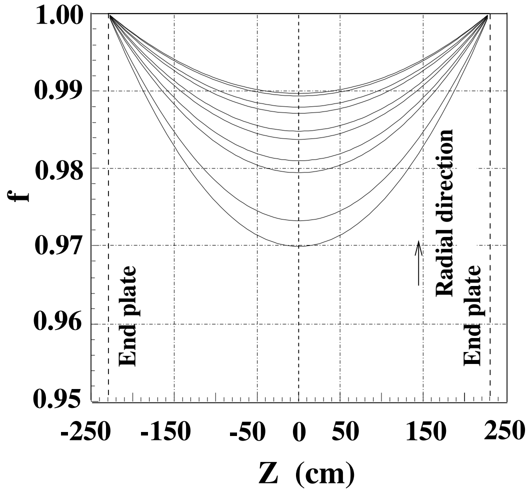

Figure 11.44: Shrink factor (f) as a function of z for all of the 10 super-layers: from the bottom to the top, the lines correspond to super-layers ordered in the radial direction.

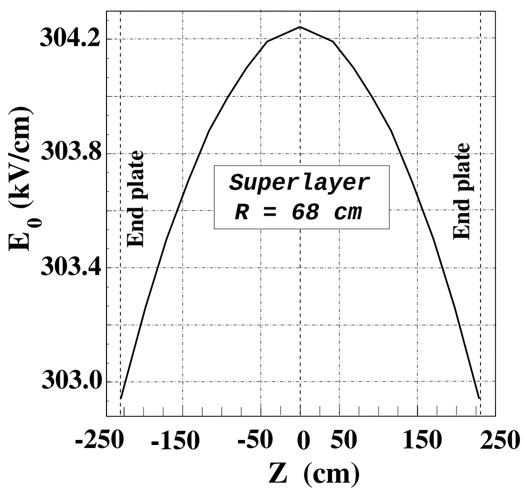

Figure 11.45: Surface field as a function of z for a sense wire in the innermost stereo super-layer at $r = 68$ cm.

and by stringing these wires with higher tensions. On the other hand, the limitation coming from the stereo geometry is inherent in any stereo chamber and is unavoidable.

Gas Gain Variation Along the Wires

Now that we know the surface field variation along any wire, we can study its z-dependent gas gain variation and discuss the operation feasibility of the chamber, provided that the relation of the surface field to the gas gain is known. Conversely, the stereo angle should be so determined to make the gain variation acceptable.

We have measured the gas gain for the CO_2(90%)-Isobutane (10%) mixture, by using a single wire proportional counter[29]. The counter is made of an aluminum cathode tube with a 10 mm inner diameter and a gold-plated tungsten anode wire with a 30 μm diameter. For the ^{55}Fe X-rays (5.9 keV) and ^{90}Sr β-rays, the charges collected on the anode within 1 μsec were measured as a function of the applied voltage.

Gas gain measurements for different Isobutane concentrations (5%, 10%, and 15%) have been made. The results for X-rays are shown in Fig.11.46. The gas gain increases as the Isobutane concentration becomes bigger.

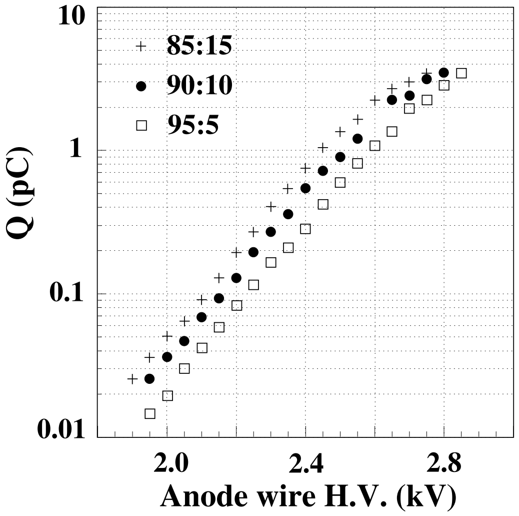

Figure 11.46: HV dependence of the charges collected in 1.0 μs for X-rays with three different concentrations of the CO_2/Isobutane mixture.

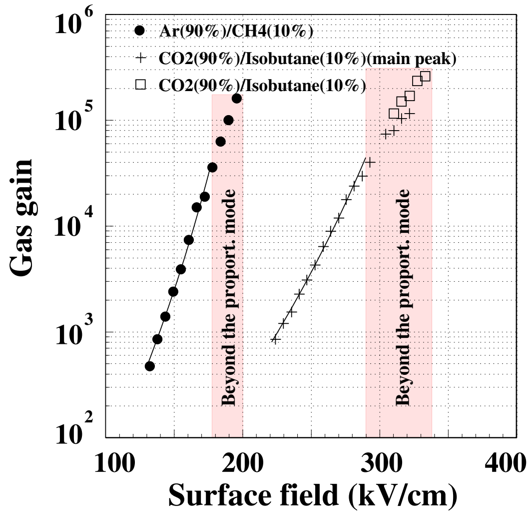

Figure 11.47: Gas gain as a function of the surface field for the Single Wire Tube with the CO_2(90%)-Isobutane (10%) gas mixture.

The measured data on the gain variation as a function of the surface field are fitted in Fig.11.47 to the following empirical formula:

$$\ln G = a + bE_0, \tag{11.18}$$

where a and b are the parameters to be determined. From these data, we obtain the following relation:

$$\frac{\Delta G}{G} = (15 \sim 20)\left(\frac{dE_0}{E_0}\right) \tag{11.19}$$

around $E_0 \simeq 300$ kV/cm, where the gas gain is about 10^4.

By combining these results with the surface field variations calculated above, we estimate the gain variation of the stereo wire due to the stereo geometry to be at most 8 % which is acceptable.

The surface field variation due to the wire displacements induced by gravitational and electrostatic forces for our 4.6 m test chamber could give rise to some additional gain variation as large as 25 % at worst. The wire displacements can, however, be reduced by appropriate choices of wire materials enduring higher tensions, a higher gain gas mixture allowing lower high voltages on sense wires, etc. On the other hand, the gas gain variation due to the stereo geometry is irreducible without geometry redesigning.

Finishing up with the stability questions, let us move on to questions 4 and 5 concerning required chamber performance [23].

Expected Chamber Performance

bf Spatial Resolution

Can we actually achieve the required spatial resolution over the full length of the 4.6 m-long chamber? In order to confirm this, we studied the performance of the test chamber using cosmic rays [23].

The so-obtained residual distribution for the central wire ($S3$) is plotted in Fig. 11.48-(a) against the drift length for tacks passing through the central cell ($C4$) in the middle of the wires, with the two trigger counters vertically aligned so as to primarily sample tracks perpendicular to the sense wires (for our naming covention, see Fig. 11.38(a)). Fig. 11.48

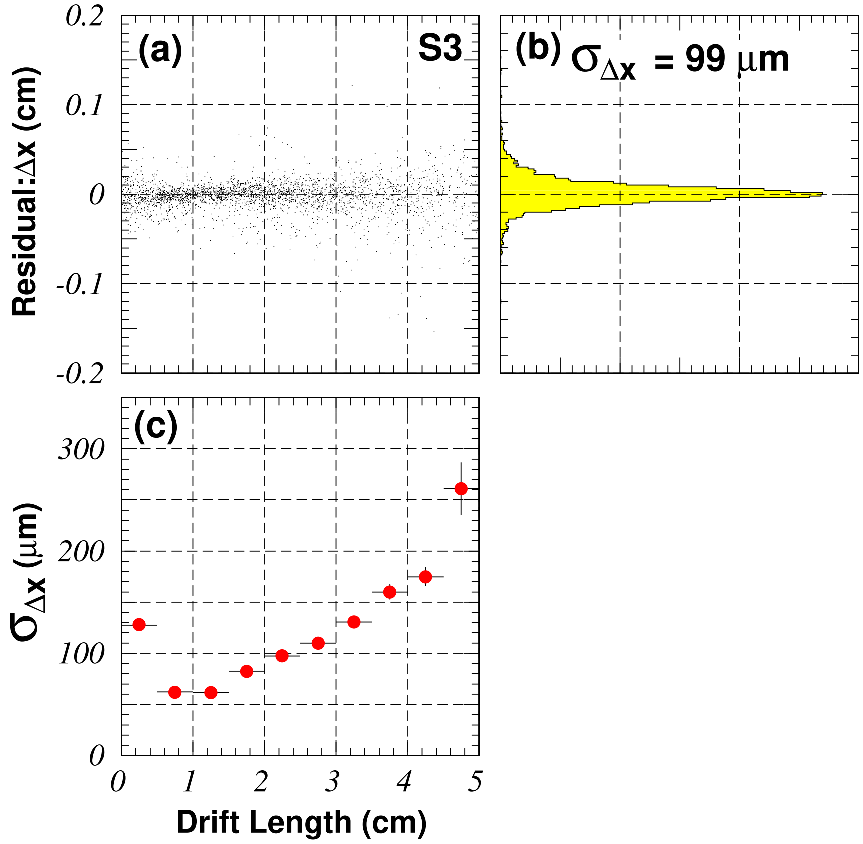

Figure 11.48: Residual for $S3$ at the center of the test chamber (a) plotted against drift length, (b) its projection to the vertical axis, and (c) the standard deviation of the residual distribution as a function of the drift length.

shows the one-standard-deviation (1-σ) width of the residual distribution as a function of the drift distance. The width is less than 100 μm for a drift length less than 2.5 cm, except for the vicinity of the sense wire[6]. It becomes, however, gradually worse up to about 200 μm towards the edge of the drift volume. Fig. 11.48-(b) is the projection to the vertical (residual) axis, demostrating the overall residual distribution. The edge wires ($S1$ and $S5$) have wider distributions. This is due to the reference track extrapolation error for $S1$ and $S5$ being much larger than the interpolation error for $S2$ to $S4$. In order to estimate the intrinsic spatial resolution of each wire we calculated the track

[6]The apparent degradation of the resolution near the sense wire is not only coming from primary ionization statistics but also from left-right ambiguity.

error as a function of the drift distance and subtracted it in quadrature on a bin-by-bin basis. We then averaged the resultant resolution over the drift distance to compensate the acceptance non-uniformity. The so-obtained overall intrinsic spatial resolutions for individual sense wires are summarized in Table 11.4. Inspection of the table tells us that the overall resolutions are around 100μm, approximately satisfying our performance goal at least locally. A similar analysis was carried out for tracks passing though the central cell near the both ends of the wires, in order to make sure that the performance goal be satisfied over the full length of the chamber. Though the spatial resolutions became slightly worse, they are still close to 100 μm as listed in Table 11.4.

Table 11.4: Summary of spatial resolutions

Wire Number	Center	Ends	Inclined
S1	$117 \pm 23(\mu m)$	$163 \pm 75(\mu m)$	$94 \pm 38(\mu m)$
S2	$103 \pm 7(\mu m)$	$136 \pm 52(\mu m)$	$95 \pm 15(\mu m)$
S3	$103 \pm 9(\mu m)$	$120 \pm 22(\mu m)$	$102 \pm 19(\mu m)$
S4	$98 \pm 9(\mu m)$	$119 \pm 22(\mu m)$	$90 \pm 19(\mu m)$
S5	$109 \pm 16(\mu m)$	$132 \pm 45(\mu m)$	$105 \pm 39(\mu m)$

The intrinsic resolutions may also depend upon the incident angle of a track to the sense wires. In order to investigate this effect, we set the two trigger counters in the middle of the chamber but slightly displaced so as to primarily sample inclined tracks having an incident angle of around 45° to the wires. This incident angle (45°) corresponds to the maximum dip angle with the full number of sense wires for the possible JLC central tracker. The width of the residual distributions were translated into overall intrinsic spatial resolutions after the track error and acceptance corrections, and are summarized also in Table 11.4. We thus confirmed that a spatial resolution of about 100μm up to an incident angle of 45°.

The efficiency for each wire was calculated as a function of the drift distance to be the fraction of tracks with actual hits on the wire in a 5-σ window. Fig. 11.49 is the results of the calculations, for an oxygen contamination in the chamber gas of about 60 ppm. The efficiency stays flat above 95% except in the last several bins close to the edge of the drift volume. The slight drop towards the edge is primarily coming from the track electron absorption due to the oxygen contamination.

To investigate the effect of the oxygen contamination in the chamber gas, we compared the chamber performance for two different oxygen contaminations, 60 ppm and 120 ppm. The oxygen molecules, being electro-negative, capture some track electrons drifting towards a sense wire and make the signal pulse smaller as the drift length gets longer. We chose the chamber gas with a slow drift velocity to reduce the effect of the diffusion of the track electron clusters. This choice made the chamber more sensitive to a small contamination from electro-negative gases. The pulse hight becomes smaller with the drift distance due to the diffusion. However, the total charge of the pulse must stay the same, as long as there is no track electron loss.

Plotted in Fig. 11.50-(a) is the integrated signal charge on $S3$ against the drift distance for an oxygen contamination of 60 ppm. The signal charge gets smaller as the drift distance becomes longer, indicating that an electro-negative gas at work.

In order to confirm this effect, we intenstionally increased the oxygen contamination to 120 ppm and measured the drift-length dependence of the signal charge. As seen in

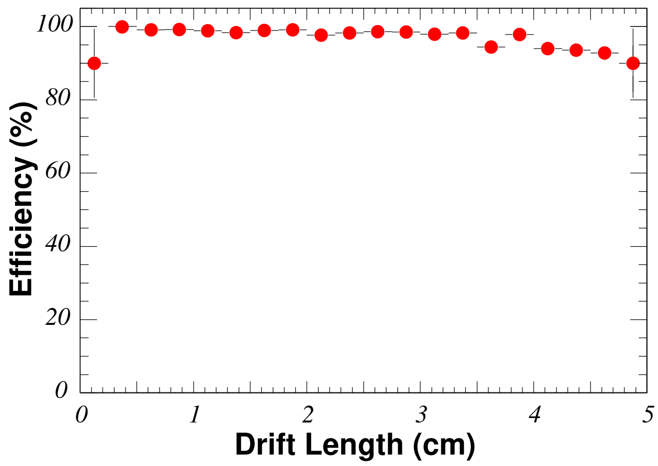

Figure 11.49: Efficiency of the central sense wire ($S3$) as a function of the drift distance.

Fig. 11.50-(b), the pulse charge rapidly decreases with the drift distance and vanishes down below the threshold at the large drift distance, suggesting a total loss of track electrons.

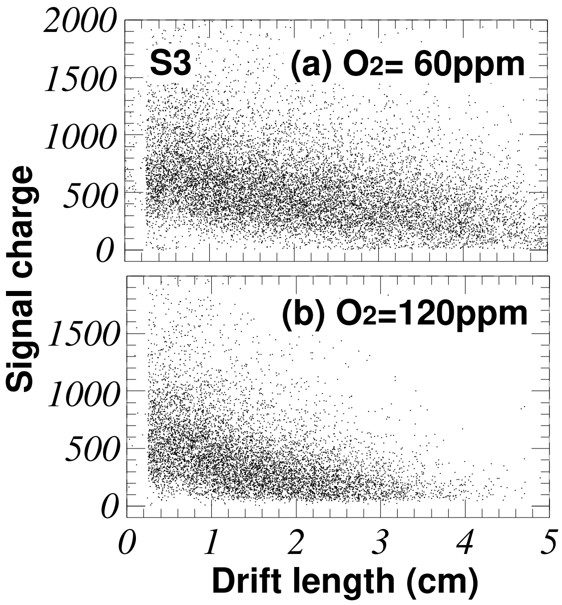

Figure 11.50: (a) Pulse charge on the central sense wire ($S3$) as a function of the drift distance for an oxygen contamination of 60 ppm. (b) Same as (a) but for an oxygen contamination of 120 ppm.

This effect not only diminishes the wire efficiencies but may also deteriorate the spatial resolutions in the large drift-length region. As a matter of fact, Fig. 11.48 shows a resolution increment with the drift distance larger than naively expected from diffusion. It may be explained by the track electron loss due to the oxygen contamination. A better performance can thus be expected if the oxygen contamination will be reduced.

Baby chamber results will be inserted later in draft 2. **Two-track separation**
We have carried out 2-track separation experiments for our baby chamber, using e^+e^- pairs produced by gamma conversions at an Al converter (see Fig. 11.51-(a) for typical FADC signals for a single event). Figure 11.51-(b) shows a preliminary result of 2-hit separation efficiency for a single sense wire as a function of 2-track distance, in the case of normal incidence. Although the preliminary result looks promising, more studies are

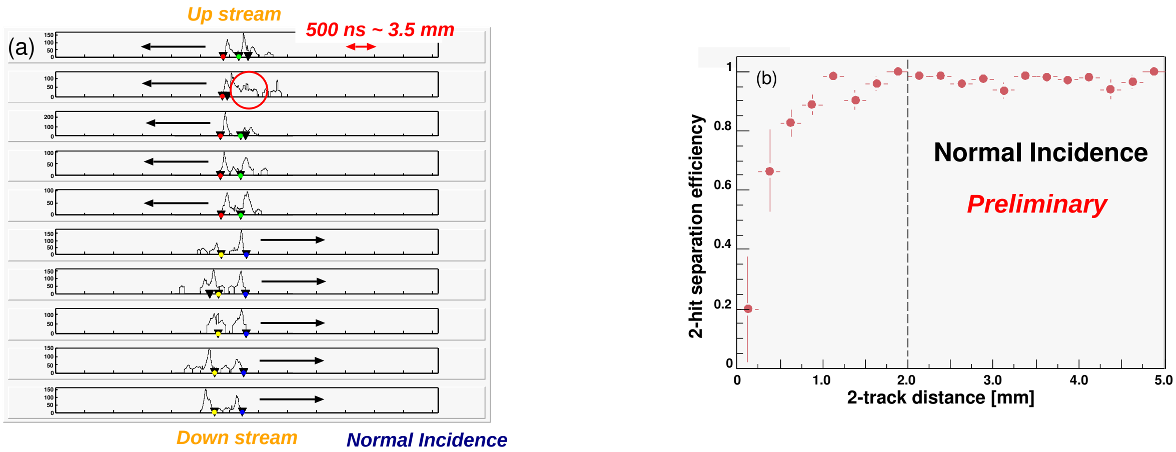

Figure 11.51: (a) FADC signals as a function of time (500 ns/division) for a typical 2-track event. (b) 2-hit separation efficiency as a function of 2-track distance.

needed to investigate possible space charge effects due to the small diffusion nature of our gas mixture. We will return to this problem later in subsection 3.f.

Particle identification *Sorry, at present this subsection is in preparation for the second draft.*

In order to investigate possibilities of further improving the chamber performance, we need detailed understanding of the space charge effects in our gas mixture, which will be discussed in the next section.

Space charge effect

On gas gain

Sorry, at present this subsection is in preparation for the second draft.

On two-track separation

Sorry, at present this subsection is in preparation for the second draft.

So much for the performance issues, let us now move on to question 7, concerning the magnitude of the magnetic field and how it affects the cell design.

Magnetic field effect

2 Tesla Design

The Lorentz angle, which is the angle between the drift direction of electrons under the influence of magnetic field and the direction of electric field, is one of the key parameters to determine the jet cell design. The existence of the magnetic field tilts drift lines by the Lorentz angle with respect to the electric field direction. If this angle is too big, drift lines for the edge wires hit top or bottom walls of the drift cell, thereby leading us to loss of detection efficiency.

Fig. 11.52 shows electron drift lines in a jet cell calculated by the chamber simulation program GARFIELD [30] (a) without and (b) with the magnetic field. The results indicates that the drift lines are completely contained in the cell at least up to a magnetic field of 2 T. There is, however, no systematic experimental data published for the Lorentz angles of CO_2/isobutane gas mixtures, which makes difficult for us to test the reliability of our calculations using the GARFIELD program. In order to confirm the results of the

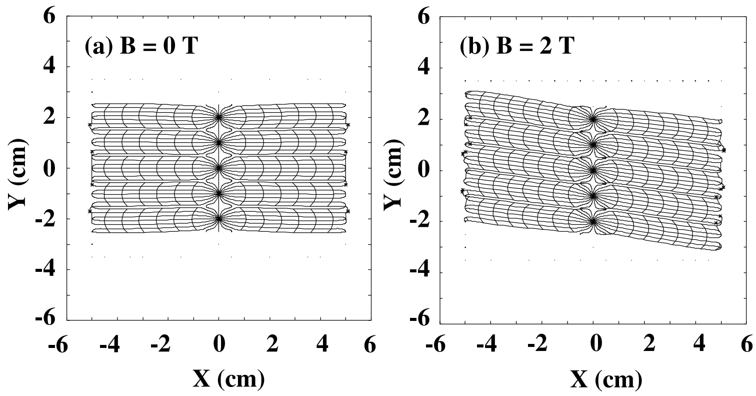

Figure 11.52: GARFIELD results of electron drift lines and iso-chrones in the JLC-CDC for the CO_2/isobutane(90:10) gas mixture.

GARFIELD calculations and to verify the validity of our cell design, we have developed a Lorentz angle measurement system for cool gas mixtures, which have small Lorentz angles, and carried out systematic measurement for CO_2/isobutane gas mixtures. The measurement system is characterized by the use of two laser beams to produce primary electrons and flash ADCs to read their signals simultaneously.

We measured the Lorentz angles for different CO_2/isobutane gas mixtures. The results are shown in Figs. 11.53-(a), -(b), and -(c) as a function of the electric field for three mixing ratios: (85 : 15), (90 : 10), and (95 : 5). At each electric field value in each figure, seven points are plotted, corresponding to, from bottom to top, seven magnetic field values: 0.0, 0.3, 0.5, 0.75, 1.0, 1.2,, and 1.5 T, respectively.

Curves in Figs. 11.53-(a), -(b), and -(c) are predictions obtained with MAGBOLTZ-1 (version 1.16) through its GARFIELD interface, although its accuracy for the velocity distribution of electrons is known to be limited under certain circumstances[31]. The loss of accuracy is caused by a decomposition of the velocity distribution function in Legendre polynomials, in which the lowest two or three terms are retained in the calculation. Therefore results given by the program may not be precise enough when the velocity distribution deviates far from isotropy or it has no axial symmetry as in the case of crossed electric and magnetic fields. On the other hand, our experimental condition seems to be favorable for application of MAGBOLTZ-1: electrons in CO_2-based gas mixtures under a low electric field are nearly thermal and the axial symmetry of the velocity distribution

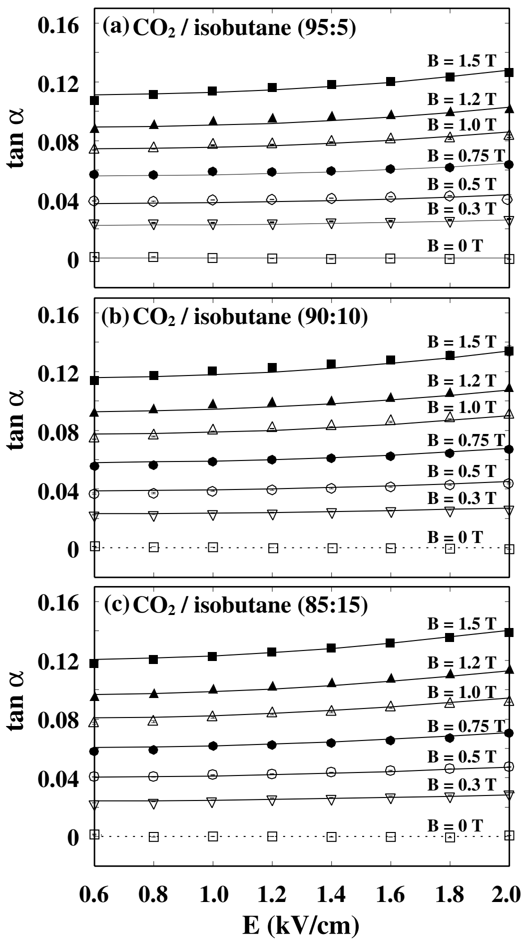

Figure 11.53: Tangent of the Lorentz angle ($\tan\alpha$) as a function of the electric field for CO_2/isobutane mixtures of (a) (95:5), (b) (90:10), and (c) (85:15). Smooth curves are GARFIELD/MAGBOLTZ predictions.

holds to a good extent, because their Lorentz angles are small even in a high magnetic field. To confirm this we ran the Monte Carlo version (MAGBOLTZ-2, version 2.2[32]), which is free from the problems stated above though time-consuming, to simulate Lorentz angles for several electric and magnetic field combinations. The results were found to be consistent with those obtained with MAGBOLTZ-1.

We calculated the magnetic deflection coefficient (ψ) from the measured Lorentz angles and the drift velocities obtained without magnetic field. Fig. 11.54 shows the resultant ψ as a function of electric field strength for the CO_2/isobutane(90:10) mixture at $B = 1.5$ T, while Fig. 11.55 shows the drift velocity in the absence of magnetic field(v_D^0). The values of ψ were found to be close to unity within $\pm$ 5% for the whole range of the applied electric and magnetic fields and for all the gas mixtures used. The gas dependence of the Lorentz angle is shown in Fig. 11.56. The observed increase of the Lorentz angle with isobutane concentration is consistent with the increase of drift velocity and with $\psi = 1$.

The current design of the JLC-CDC assumes operation under a magnetic field of 2.0 T. Figure 11.57 plots the Lorentz angle as a function of the magnetic field. The Lorentz angle is proportional to the magnetic field as long as $\psi = 1$. We thus fit the data points below 1.5 T to a straight line passing through the origin and extrapolate the line to 2.0 T, in

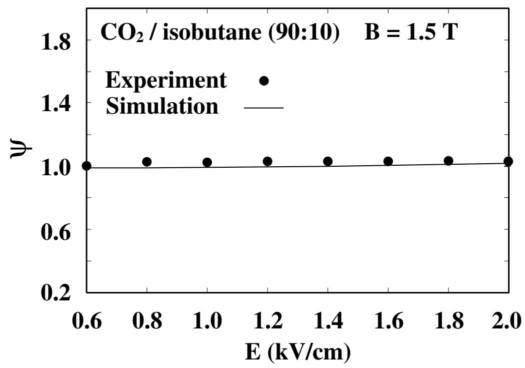

Figure 11.54: Magnetic deflection coefficient at $B = 1.5$T as a function of the electric field for the CO_2/isobutane(90:10) mixture.

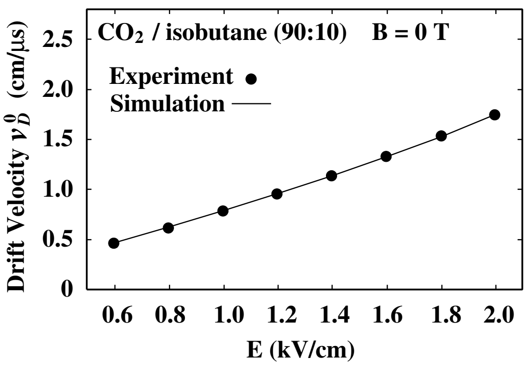

Figure 11.55: Drift velocity at $B = 0$ as a function of the electric field for the CO_2/isobutane(90:10) mixture.

order to estimate the Lorentz angle for the JLC-CDC. At $E = 1$ kV and $B = 2$ T the extrapolated Lorentz angle is $\tan\alpha = 0.159 \pm 0.002$ for the CO_2/isobutane(90:10) mixture. The shaded band above 1.5 T indicates 1-σ extrapolation error interval. The solid line in the figure is the prediction of GARFIELD/MAGBOLTZ which is consistent with the extrapolation for 2 T.

Higher Magnetic Field Option

Motivated mainly by recent studies of beam-induced background[33], possibility of higher magnetic field is now under serious considerations. Our current cell design allows a magnetic field up to about 3 T. Since GARFIELD/MAGBOLTZ reproduces our Lorentz angle data very well, it is plausible that it continues to work well at around 3 T, too. It is, however, desirable to confirm this experimentally. We are thus planning to measure Lorentz angles at higher magnetic fields.

11.4.4 Summary and Conclusions

11.5 Performances of tracking system

Vertexing performance

Using the Quick Simulator, performances of the topological vertexing and the mass tagging method was studied. The topological vertexing algorithm was developed by SLD group[**?**].

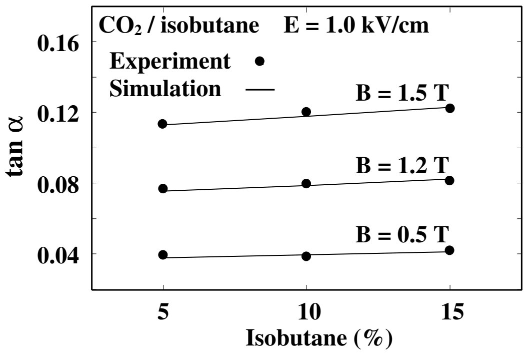

Figure 11.56: Isobutane concentration dependence of $\tan\alpha$ at $E = 1.0$ kV/cm. The solid lines are GARFIELD/MAGBOLTZ predictions.

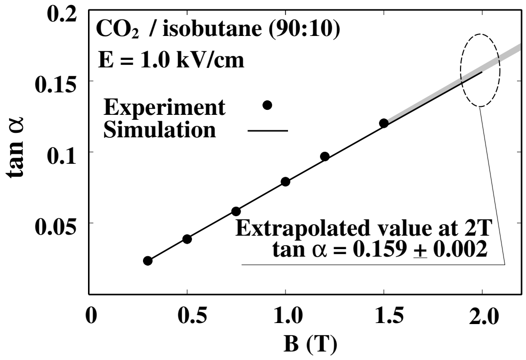

Figure 11.57: $\tan\alpha$ at $E = 1.0$ kV/cm plotted against the magnetic field for the CO_2/isobutane(90:10) mixture. The shaded band above $B = 1.5$ T is the 1-σ bound for the straight-line extrapolation, while the solid line is the GARFIELD/MAGBOLTZ simulation.

In this method, a tube of probability is defined along a particle trajectory. Since the probability is high when trajectories overlap, such points are selected as vertices. When secondary or tertiary vertex is found, the p_t corrected mass (`MSPTM`) is calculated from the vertex mass (M_{vtx}) and the vertex momentum transverse to the flight direction of the vertex (P_T): `MSPTM`$=\sqrt{M_{vtx}^2 + P_T^2} + |P_T|$.

For the study, we generated quark pair events at Z pole. The events were clustered to two jets by using the JADE clustering algorithm. Y_{cut} were varied so as to clustered as two jets. When the production angle of the jet satisfied $|\cos\theta_{jet}| < 0.8$, the tagging method was applied and efficiencies and purities were studied.

The Fig. 11.58(A) shows a probability to find secondary vertices when $b\bar{b}$ events are generated. The efficiency was about 90% and flat for decay length greater than about 0.1 cm. The distribution of `MSPTM` is shown in Fig. 11.58(B) for jets whose secondary decay length is greater than 300 μm. We can see clear separation between b quark jets and c quark jets.

We tagged jets as b when the decay length was greater than 300 μm and M_{corr} was greater than the cut value. The purity and the efficiency of b tagging is shown in Fig. 11.58(C), which was obtained by changing the cut value from 1.0 GeV to 5.0 GeV. The open-square points are for the JLC 3T detector. For comparison, we defined a new geometry with an additional CCD layer at 1.2 cm and the beam pipe at 1.0 cm. The purity and the efficiency in that case is shown in the same figure. In this case, the

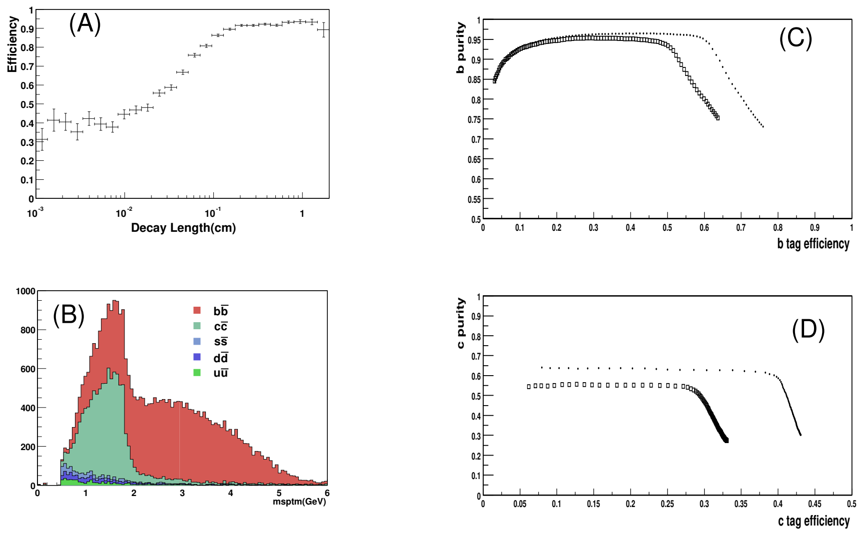

Figure 11.58: (A) The efficiency to find secondary vertices in b quark jets, (B) The p_t corrected secondary mass distribution for each quark, (C) b tag efficiency and purity for the JLC detector (open square) and for additional CCD layer at 1.2 cm (circle), (D) Same as (C) for c tag.

requirement to the decay length was reduced to 150μm, thanks to the improved vertex resolution. As a result, the efficiency was increased about 10% for the selection of purity greater than 95%.

In the case of c tagging, we required the decay length to be greater than 150μm and `MSPTM` was between 0.55 GeV and the cut value, which is changed from 1.0 GeV to 5.0 GeV. The result is shown in the Fig. 11.58(D) for the case of the JLC detector and with the additional CCD layer. The c tag efficiency is about 30% with the purity of about 50% in the case of the JLC detector. Both the efficiency and the purity will be improved by using additional conditions such as vertex momentum, etc.

The tracking performance

As tracking performances, we studied a momentum resolution and a missing mass resolution of $e^+e^- \to ZH$ process using the JIM Full simulator.

To study the momentum resolution, we generated a single μ track by JIM. Generated exact hits points were smeared by assumed resolution. Hit points were fitted by helix parameters separately for CDC and VTX. After moving a pivot of CDC helix parameter to that of VTX, taking into account energy losses and multiple scatterings, they were averaged with weights of error matrices to get a CDC-VTX combined helix parameter. This method does not require a cpu time consuming minimization procedure such as a kink fitting and reasonable results can be obtained as multiple scatterings and energy losses in the material can be well approximated by Gaussian.

The p_t resolution and the impact parameter resolution as a function of p_t are shown in the paper[?] presented at the session of “Simulation Tools’. The p_t resolution was $0.9 \times 10^{-4} p_t$ at high momentum and the impact parameter resolution in $r\varphi$ plain was 25 μm at 1 GeV.

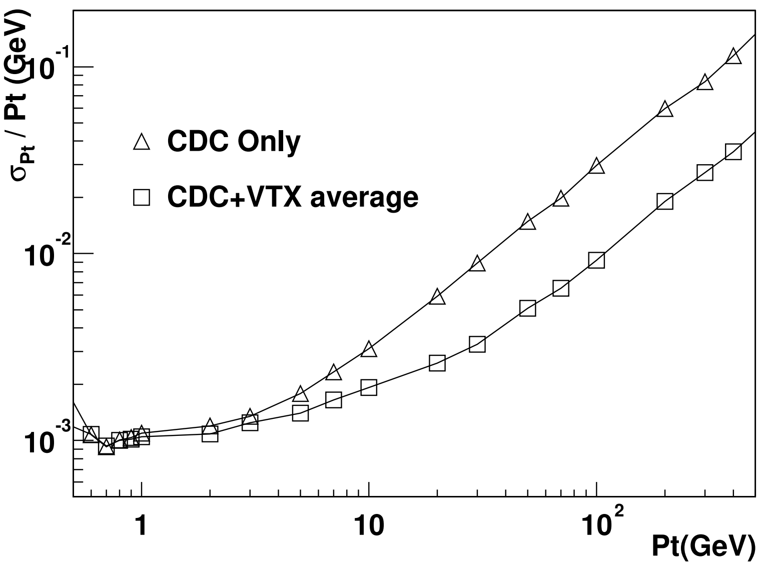

Figure 11.59: The p_t resolution by a fit to CDC hits only and by a CDC and VTX helix average

The obtained p_t resolution is shown in Fig. 11.59. The momentum resolution(σ_{p_t}/p_t) of about $1\times10^{-4}p_t$ can be achieved at high momentum. The impact parameter resolution as a function of p_t is shown Fig. 11.60, which is about 25 μm at 1 GeV.

The missing mass resolution was also studied using a process $e^+e^- \rightarrow \mu^+\mu^-X$. This is a channel to search Higgs independently with its decay mode and a width of Higgs can be measured if it is large enough to be detected. For the study, we generated events using Helas[?]/Bases/Spring[?] libraries in PhysSim[?] package. The beamstrulung spectrum of JLC-I[17] X-band 300 GeV parameter with $\pm0.5\%$ initial energy spread was included. The center-of-mass energy was 250 GeV.

The event was selected by requiring two good charged tracks (the number of sampling is equal to 50) whose invariant mass is between 80 to 100 GeV. The obtained the missing mass spectrum is shown in Fig. 11.61. The spectrum is fitted by the curve given by

$$F(m) = N_H \int F_H(m,t) \exp^{-\frac{t^2}{2\sigma^2}} dt + N_Z \cdot F_Z(m) \tag{11.20}$$

where $F_Z(m)$ is a scaled missing energy respect to Z($F_Z(m) = 1 - \frac{m-M_Z}{\sqrt{s}-M_Z}$), and $F_H(m,t)$ is that to Higgs ($F_H(m,t) = Max(0, 1 - \frac{m-M_H+t}{\sqrt{s}-M_H})$). From the fit, we obtained the missing mass resolution of 1.0 GeV. The main contribution to the width is the initial energy spread of $\pm0.5\%$, but the resolution could be slightly improved to 0.9 GeV if the measurement is performed at 240 GeV.

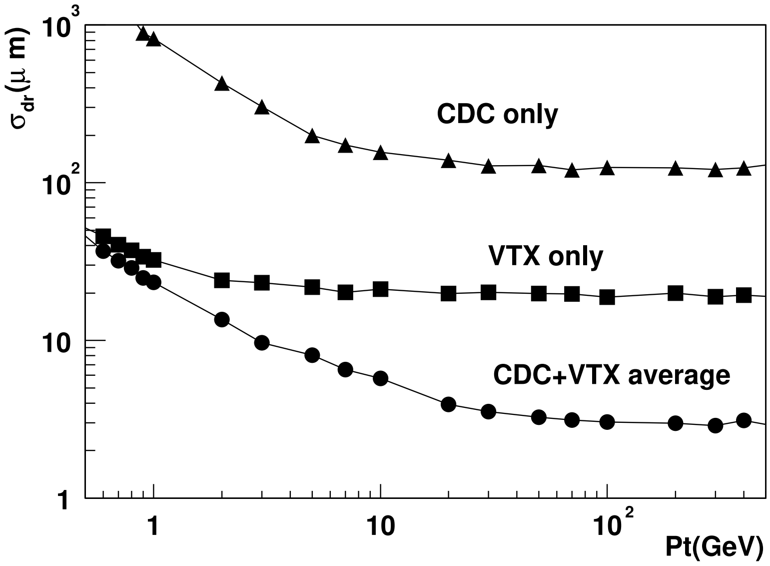

Figure 11.60: The 2D impact parameter resolution as a function of P_t by a fit to CDC hits only, VTX hits only and CDC-VTX helix average.

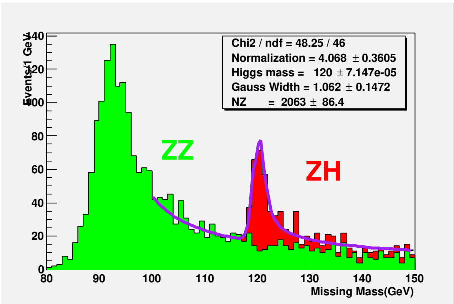

Figure 11.61: The missing mass spectrum of the two tracks for $e^+e^- \to ZH$ and ZZ processes.

Bibliography

[1] K. Abe *et al.*, "Design and Performance of the SLD Vertex Detector, a 307 Mpixel Tracking System", Nucl. Instr. and Meth. A400, 287-343 (1997).

[2] J. Janesick et al., *SPIE. Optical Sensors and Electric Photography* **1071** (1997) 153. in: N. S. Saks. *IEEE Electron Device Lett.* **EDL-1-7** (1980) 131.

[3] S5466, *FFT-CCD Image Sensor S5466.* (1995) Hamamatsu Photonics K.K. Ltd.

[4] CCD02-06 Series SIS, *A1A-CCD02-06 Series Scientific Image Sensor Issue 4.* (1993) EEV Co. Ltd.

[5] T.Aso et al., *KEK Report* **99-84** (1999).

[6] C. White, *Nucl. Instr. and Meth.* **A351** (1994) 217.

[7] T. Tsukamoto et al., *Nucl. Instr. and Meth.* **A383** (1996) 256. in: T. Tsukamoto et al., *KEK Preprint.* **98-19** (1998).

[8] R. Turchetta, *Nucl. Instr. and Meth.* **A335** (1993) 44.

[9] K. Abe *et al.*, "Design and Performance of the SLD Vertex Detector, a 307 Mpixel Tracking System", SLAC-PUB-7385 (1997).

[10] R. Wunstorf, "Radiation Hardness of Silicon Detectors: Current Status", *IEEE Trans. Nucl. Sci.*, **NS-44**, 806–814 (1997).

[11] T. Roy, S. J. Watts, and D. Wright, "Radiation Damage Effects on Imaging Charge Coupled Devices", *Nucl. Instrum. Methods*, **A275**, 545–557 (1989).

[12] J. Janesick, T. Elliott and F. Pool, "Radiation Damage in Scientific Charge-Coupled Devices", *IEEE Trans. Nucl. Sci.*, **NS-36**, 572–578 (1989).

[13] G. R. Hopkinson, "Cobalt-60 and Proton Radiation Effects on Large Format, 2-D, CCD Arrays for an Earth Imaging Application", *IEEE Trans. Nucl. Sci.*, **NS-39**, 2018–2025 (1992).

[14] G. R. Hopkinson, C. J. Dale, and P. W. Marshall, "Proton Effects in Charge-Coupled Devices", *IEEE Trans. Nucl. Sci.*, **NS-43**, 614–627 (1996).

[15] I.H. Hopkins and G.R. Hopkinson, "Random Telegraph Signals from Proton-Irradiated CCDs", *IEEE Trans. Nucl. Sci.*, **NS-40**, 1567–1574 (1993).

[16] N. S. Saks, “A Technique for Suppressing Dark Current Generated by Interface States in Buried Channel CCD Imagers”, *IEEE Electron. Dev. Letters*, **EDL-1**, 131–133 (1980).

[17] N. S. Saks, “A New Technique for Hardening CCD Imagers by Suppression of Interface State Generation”, *IEEE Trans. Nucl. Sci.*, **NS-27**, 1727–1734 (1980).

[18] K. D. Stefanov, T.Tsukamoto, A. Miyamoto, Y. Sugimoto, N. Tamura, S. Takahashi, K. Abe, T. Nagamine, and T. Aso, “Investigation of the Radiation Performance of CCD Sensors in a Vertex Detector Application”, *Nucl. Instrum. Methods*, **A436**, 182–187 (1999).

[19] K. D. Stefanov, T. Tsukamoto, A. Miyamoto, Y. Sugimoto, N. Tamura, K. Abe, T. Nagamine, and T. Aso, “Electron and Neutron Radiation Damage Effects on a Two-Phase CCD”, *IEEE Trans. Nucl. Sci.*, **NS-47**, 1280–1291 (2000).

[20] Y. Sugimoto and H. Y. Young, “Test of Charge Injection into CCD Sensors”, JLC VTX Internal Report, KEK (2000).

[21] K. D. Stefanov, “Radiation Damage Effects in CCD Sensors for Tracking Applications in High Energy Physics”, Ph.D. thesis, Saga University (2001).

[22] *Nucl. Instr. Meth.* **A383** (1996) 391.

[23] *Nucl. Instr. Meth.* **A441** (2000) 393.

[24] *Nucl. Instr. Meth.* **A428** (1999) 403.

[25] KEK Preprint 2000-113 (hep-ex/0012002), Submitted to *Nucl. Instr. Meth.* **A**.

[26] R.L. Gluckstern, Nucl. Inst. and Meth. **24** (1963) 381, JLC physics group, http://www-jlc.kek.jp/subg/offl/lib/docs/helix_manip

[27] JLC CDC group, a paper on two-track separation paper, in preparation.

[28] T.Regan, Nucl. Inst. and Meth. A219 (1984) 100; S.Bhadra et al., Nucl. Instr. and Meth. A269 (1988) 33; E.R.Mueller, Nucl.Instr. and Meth. A281 (1989) 652.

[29] *Nucl. Instr. Meth.* **A447** (2000) 459.

[30] R. Veenhof, Nucl. Instr. and Meth. **A419** (1998) 726,
S.F. Biagi, *Nucl. Instr. and Meth.* **A421** (1999) 234.

[31] R. Robson, M. Hildebrandt, and B. Schmidt, Nucl. Instr. and Meth. **A394** (1997) 74.

[32] S.F. Biagi, Nucl. Instr. and Meth. **A421** (1999) 234.

[33] *Beam BG section of this report*

Chapter 12

Particle Identification

Chapter 13

Calorimetry

13.1 Design Criteria

One of the most important physics to study at LC is precision study of Higgs boson produced in a reaction $e^+e^- \to Z^0H$. Large backgrounds to this process from W^+W^- and Z^0Z^0 pair production should be removed by b-tagging and reconstructed 2-jet masses. Precision study of weak couplings and top properties also need precise event reconstruction using 2-jet masses under up to 8-jet environment. We therefore set a design criteria for the calorimeter system in combination with the central tracker such that the 2-jet mass resolution be as good as the natural width of weak bosons for excellent W/Z identification. Based on this criteria, the baseline detector model has been made and simulation studies have been carried out.

In order to achieve the required 2-jet mass resolution, we set target energy resolution for calorimeters to be

$$\begin{aligned}\frac{\sigma_E}{E} &= \frac{15\%}{\sqrt{E(\mathrm{GeV})}} \oplus 1\% \quad \text{for e}/\gamma,\ \text{and}\\ \frac{\sigma_E}{E} &= \frac{40\%}{\sqrt{E(\mathrm{GeV})}} \oplus 2\% \quad \text{for hadrons,}\end{aligned}$$

with reasonably fine granularity. In addition, the calorimter should have cluster-position resolution better than 1 mm to achieve precise track-cluster association for jet reconstruction.

Fig. 13.1 shows an example of 2-jet mass resolution obtained by quick simulation with the baseline detector of 2tesla version for the reaction $e^+e^- \to W^+W^-$ at $\sqrt{S} = 400$ GeV. Obtained mass resolution of 2.9 GeV with kinematical fit is reasonably good taking into account that anlysis algorithm and paramteters are not yet optimized very well. Various origins of the width are decomposed in the table 13.1. Each contribution was calculated by replacing each information with generator information.

It has been widely known that in order to achieve the best event reconstruction, tracking information should be used for charged particles, while calorimeter information should be used only for neutral particles. This has been a conventional way in energy analysis of e^+e^- collider data from the early days. For this purpose, calorimeter hits generated by charged particles should be precisely identified and deleted. Therefore,

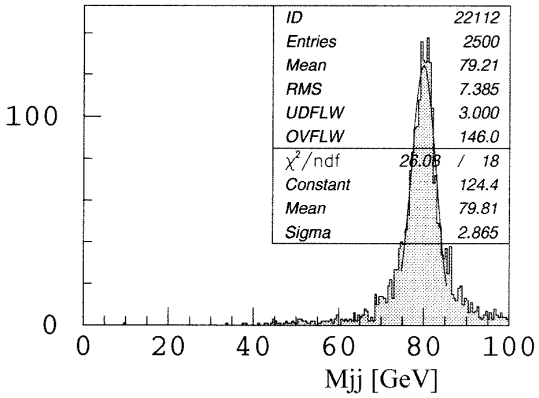

Figure 13.1: An example of reconstructed-mass resolution for W with kinematical fit for the reaction $e^+e^- \to W^+W^-$ at $\sqrt{S} = 400$ GeV, obtained by quick simulation with the baseline detector of 2Tesla version.

Natural width of W	~ 1.6 GeV (in terms of σ)
Neutrino escape	~ 0.8 GeV
CDC momentum resolution	~ 1.3 GeV
CAL energy resolution	~ 1.2 GeV
Cluster-track association	~ 1.9 GeV
Jet clustering	~ 1.1 GeV
Total Width	~ 3.3 GeV (without kinematical fit)

Table 13.1: Various contributions to the width of reconstructed W mass for the reaction $e^+e^- \to W^+W^-$ at $\sqrt{S} = 400$ GeV.

excellent clustering followed by precise track-cluster association plays essentail role in analysis. This conventional method has been used for analysis of quick-simulation data. However, existence of neutral objects are identified solely by energy-momentum unbalance of associated cluster and track, which does not not require very fine granularity.

From the table, it is seen that more improvements in track-cluster associaction algorithm and in hadron clustering should further improve this result. Needless to say, however, verification with full simulation is indispensible to validate/optimize the baseline parameters.

13.2 Baseline Design

The JLC calorimeter system is characterized by :

- excellent hadron energy resolution;
- reasonably fine granularity;
- whole calorimter system inside of the superconducting solenoid.

Required hadron energy resolution of $40\%/\sqrt{E}$ can only be achieved with compensation, which means that calorimeter signals for EM particles and for hadrons of the same energy have the same amplitude. There are two ways to acheive the compensation; either hardware compensation or software compensation. Software compensation, first adopted by H1 liq.Ar calorimter [1], requires very fine granularity to apply to LC detectors aimed at precision physics, and thus results in very high cost. On the other hand, hardware compensation can be achieved by simply adjusting the calorimeter composition, and requires no additional effort/cost. We therefore chose hardware-compensation with tile/fiber technique as the a baseline design. By adopting hardware compensation, we can de-couple energy resolution and granularity ; the best energy resolution can be achieved regardless the granularity, and granularity can be determined only by the criteria from topological reconstruction.

The tile/fiber calorimeter has following features:

- Essentially crackless hermeticity;
- Capability for very fine longitudinal segmentation;
- Easy to design projective tower layout;
- Easy to integrate preshower and shower-max detectors;
- Reasonable transverse segmentation;
- Less expensive than crystals and liq.Ar.

In addition, the hardware compensation results in following features:

- Excellent hadron energy resolution and linearity;
- High density;
- Reasonable EM energy resolution;
- Relatively low light yield.

Our analysis based on quick simulations indicates that very fine granularity is not necessary for calorimeter. Therefore present baseline design is considered to be almost optimum for the hadron calorimeter (HCAL). For the EM calorimeter (EMC), on the other hand, very fine granularity might be required for precise event topology reconstruction, even though quick simulation tells us that present granularity shows high performance.

In that case software compensation would be another option. Further simulation analysis will answer this question.

We also need excellent preshower detector (PSD) and shower-max detector (SMD) for $e/\gamma/\pi^{\pm}/\pi^0$ separation, two-cluster identification, and track-cluster association. To have plural layers of shower position detectors (SPD) in EMC enables precise measurement of off-vertex photon direction.

All the calorimter system, including the photon detectors, are designed to be located inside of the 3 Tesla (or 2Tesla) magnetic field. We therefore need high-gain high-sensitivity photon detectors operational in the strong magnetic field, since hardware compensation results in relatively poor photon yiled compared to the usual sampling calorimeters. We discuss such photon detectors in a separate section.

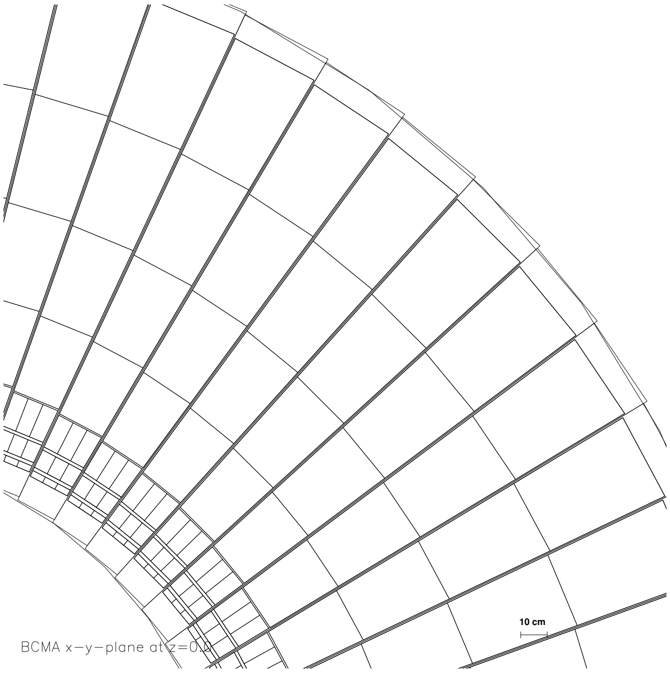

Figure 13.2: Configuration of the baseline design of barrel calorimeter system (x-y cross section) implemented into a full simulator.

The GEANT3 drawing of the baseline-design barrel calorimeter is shown in Fig. 13.2. There are 2 Tesla option and 3 Tesla option, and detector sizes are smaller for the latter.

In the case of the 3Tesla design, inner and outer radii of the barrel calorimeter are 160 cm and 340 cm, respectively, and the length is ± 180 cm. Inner radius of the endcap calorimeter is 50 cm, and the front face locates at $z = \pm 190$ cm. Angular coverage of the endcap calorimeter with full-thickness therefore extends to $|\cos\theta\ | < 0.966$, while partial-thickness coverage extends to $|\cos\theta\ | < 0.991$.

The calorimeter is an array of super-towers with pointing geometry with small offset. One super-tower is composed, from the inner-radius to the outer-radius, of PSD (3×3 in a super-tower), SMD, EMC-1(3×3), SPD, EMC-2(3×3), HCAL-1, HCAL-2, HCAL-3, and HCAL-4. There are about 2000 super-towers in the barrel calorimeter, and about 3000 in total in the endcap calorimeters. One super-tower has readout channels of 31 and 48 for calorimetric measurement and for position measurement, respectively.

	2T-case	3T-case	
Barrel Inner Radius	250cm	160cm	
Barrel Outer Radius	400cm	340cm	
Endcap Inner Radius	50cm	50cm	
Endcap Face Z-location	290cm	190cm	
Angular Coverage			
Full Thickness	$\|\cos\theta\|<0.985$	$\|\cos\theta\|<0.966$	
Partial Thickness	$\|\cos\theta\|<0.994$	$\|\cos\theta\|<0.991$	
SHmax Detector	Sintillator Strip (1cm-wide)	Sintillator Strip (1cm-wide)	option= Si-pad (1cm x 1cm)
Thickness			
PreSH	4Xo	4Xo	4mm-Pb x 6 layers
EMC	23Xo	23Xo	4mm-Pb x 32 layers
HCAL	6.5λo	6.5λo	8mm-Pb x 130 layers
Granurality			
PS/EMC transverse	6cm x 6cm (24mrad)	4cm x 4cm (24mrad)	
longitudinal	3 sections	3 sections	6+12+20 layers
HCAL transverse	18cm x 18cm (72mrad)	12cm x 12cm (72mrad)	
longitudinal	4 sections	4 sections	25+30+35+40 layers

Table 13.2: Parameters of the calorimeter system implemented into a full simulator. 2 Tesla option is the previous large detector option, and 3 Tesla option is a new detector design.

Parameters of these sub-detectors are summarized in Table 13.2. All the parameters in the table are the first trials, and need optimization with full simulation.

13.2.1 EM Calorimter (EMC)

EMC is a sampling calorimeter composed of 4mm-thick lead plates and 1mm-thick plastic scinitllator plates. Photons from the scintillator plates (tiles) are read out via wavelength shifting fibers (WLS fibers) embedded in the tiles, and then transfered through clear fibers to photon detectors (tile/fiber technique). Additional 1mm-thick acryl plates are stacked on the tile assembly to accomodate clear fibers. This design sampling frequency is expected to achieve stochastic term of the EM energy resolution of $15\%/\sqrt{E}$, provided that photon statistics does not contribute.

EMC is longitudinally divided into PSD, EMC1 and EMC2, to improve hadron/electron identification. Thicknesses of these sections are 4.3 X_0 (radiation length), 8.6 X_0, and 14.3 X_0, respectively. We expect pion rejection better than 1/1000 with electron efficiency of 98% when used with HCAL information. Transverse cell size of EMC is 4cm$\times$4cm in the baseline design of 3Tesla-version, and 3×3 EMC cells cover one HCAL cell. This transverse size is limited by the cost and technical feasibility of small tiles, or to be more precise, bending radius of WLS fibers at corners.

13.2.2 Hadron Calorimter (HCAL)

HCAL is composed of 8mm-thick lead plates, 2mm-thick plastic scinitllator plates, and 1mm-thick fiber-routing acryl plates. HCAL also has tile/fiber configuration. This sampling frequency was expected to achieve stochastic term of the hadron energy resolution of $40\%/\sqrt{E}$, provided that photon statistics did not contribute.

HCAL is longitudinally divided into four sections with thicknesses of 1.25 λ_0 (interaction length), 1.5 λ_0, 1.75 λ_0, and 2.0 λ_0. Total thickness including EMC is 7.5 λ_0. Transverse segment size of HCAL is 72 mrad at $\theta = 90°$ seen from the interaction point, which corresponds to 12cm at the front face of HCAL section in the case of 3Tesla-design.

Number of longitudinal segmentation is limited only by number of photon-detector channels. Improvement in multi-channel photon detecotrs enables much finer longitudinal segmentation, and thus enables more sophisticated clustering and two-cluster separation algorithms. Transverse segment size, on the other hand, is limited by cost, and it seems difficult to make it much smaller.

13.2.3 Shower-Max Detector(SMD) and Shower-Position Detector(SPD)

The purpose of SMD is π^0/γ identification, precise measrement of cluster position for track-cluster association, and two-cluster recognition. SMD also improves $e/\pi^{\pm}$ separation by transverse signal distribution. For this purpose, fine segmentation is necessary for SMD. Also needed is wide dynamic range to detect minimum-ionizing particles (MIP) and developing EM showers simultaneously.

The baseline design for SMD is an arrays of plastic scintillator strips. Strip size is 1cm-wide and 5mm-thick. An array of 12 strips covers one super-tower in the case of 3Tesla design, and 18 strips in the case of 2Tesla design. Two orthogonal layers give $\theta - \varphi$ position information with accuracy of better than 1 mm for e/γ of energy greater than several GeV. Ghosts are removed, though not completely, by pulse-height analysis.

Photons from the scintillator strips are read out by WLS-fibers in the baseline design. Another option is under study to read out photons directly using photo-diodes attached on the strips.

Another shower position detector (SPD) is installed between EMC-1 and EMC-2. SPD has the same configuration as SMD. The purpose of SPD is to measure the direction of the isolated off-vertex photons. SPD also helps hadron shower position measurement by measureing early stage of hadron shower development, and thus improves track-cluster association for charged hadrons.

The baseline design has only one set of SPD. Whether we need more layers or not should be investigated.

13.2.4 Photon Detectors

Photon detectors for scintillating light are designed to sit at the end of the calorimeter assembly in the magnetic field, rather than stretching the clear fibers to the outside of the iron yoke of the whole detector. Therefore high-sensitivity photon detectors operational inside of 3Tesla (or 2Tesla) magnetic field are necessary. At present, we assume that;

- Both EMC and HCAL are read out by multi-channel HPDs;
- PSD are read out either by multi-channel HPDs or multi-channel HAPDs;
- SMD and SPD are read out either by multi-channel HAPDs or EBCCDs.

Here HPD, HAPD and EBCCD stand for Hybrid Photo-Diode, Hybrid Avalanche Photo-Diode, and Electron-Bambarded CCD, respectively. Though some fine-mesh photomultiplier tubes show quite high gain even in 2.5 Tesla, we decided not to use them. Detailed R&Ds are further needed to decide which option is better.

There are 133k , 20k, and 237k channels of EMC, HCAL, and SMD/PSD to read out, respectively. Therefore, it is impractical to use single-channel photon detectors. With multi-channel HPDs and EBCCDs under study at present, only one multi-channel HPD and one EBCCD can read out of all the calorimetric signals and position detector signals from one super-tower, respectively.

13.2.5 Other Detector Options

There are several calorimter schemes other than the baseline-design tile/fiber scheme. The features of various detector schemes are summarized in Table 18. The listed features are just potentials, and whether constructed detectors really have such features or not is a different question. For the energy resolution, resolutions of typical EM calorimeters are quoted. Hadron energy resolution strongly depends on the detailed structure and analysis algorithm. It should be stressed that longitudinal segmentation is essentially important for e/π separation.

Besides the properties in the table, liquid calorimeters have additional bad features as:

- Cryogenic pipes and walls tend to behave as anomaly (or a hole at the worst case);
- Materials and gap between inside tracker and EMC deteriorate track-cluster association and EMC performance.

Nevertheless, liq.Ar calorimeter has been adopted by ATLAS EMC due to its high resistance against radiation damage, which is not the case for LC environment. For large-scale general-purpose detectors at LC, therefore, tile/fiber scheme has the best-balanced features.

Detector Scheme	EM Energy Resolution	Transverse Segmentation	Longitudinal Segmentation	Hermeticity	Cost	Examples
Crystals	Excellent	Good	Poor	Good	Expensive	L3, Belle, CMS
SPACAL	Good	Good	Poor	Good	Expensive	H1, KLOE
Shashlik	Good	Good	Poor	Good	Expensive	Phenix, Hera-B
W/Si	Good	Excellent	Excellent	Excellent	Very Expensive	luminosity monitors
liq.Ar	Good	Excellent	Excellent	Reasonable	Expensive	SLD, D0, H1, ATLAS
Tile/fiber	Reasonable	Reasonable	Excellent	Excellent	Reasonable	CDF, STAR

Table 13.3: Properties of various detector schemes for EM calorimetry.

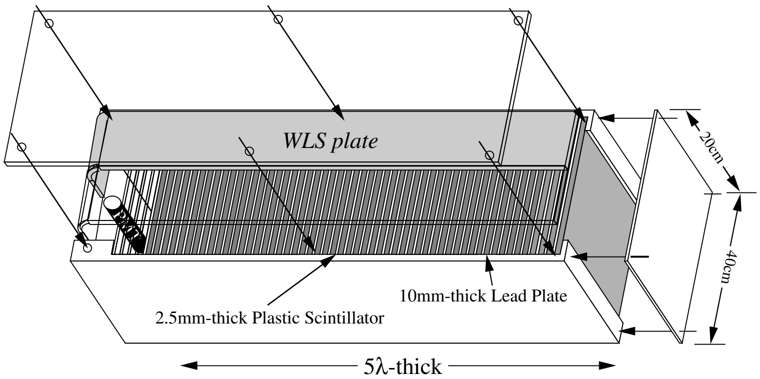

Figure 13.3: Schematical drawing of ZEUS-type test module.

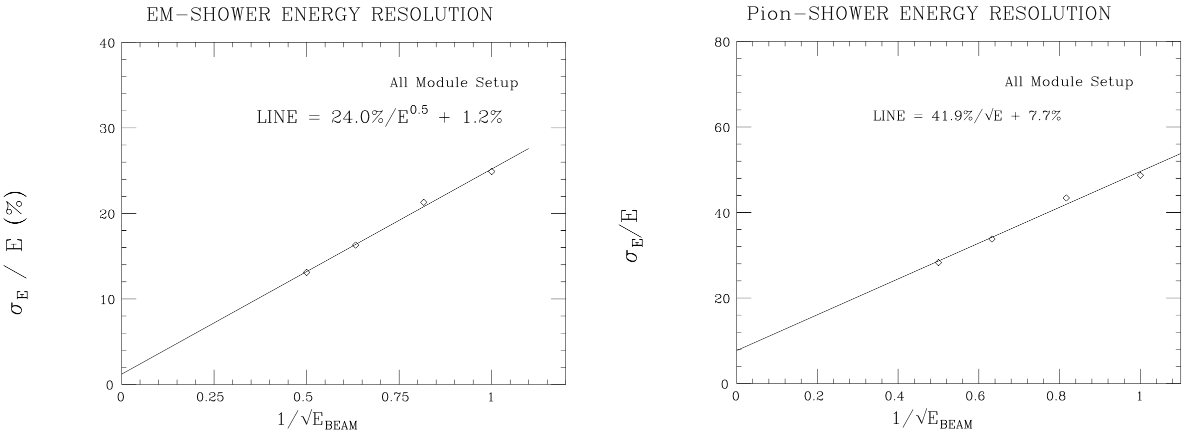

Figure 13.4: Energy resolutions of ZEUS-type hadron calorimeter test modules for electrons (left) and for pions (right).

13.3 Hardware Study

13.3.1 ZUES-type Test Module

We first investigated the possibility of ZEUS-type sandwich calorimeter because it was the best-operating hadron calorimeter in the collider detectors when we started R&Ds. We built four hadron calorimeter test modules with similar configuration to the ZEUS test modules [2]. It was composed of 10mm-thick lead plates and 2.5mm-thick plastic scintillator plates as shown in Fig. 13.3. This volume ratio was expected to acheive hardware compensation. Photons were read out by WLS plates attached on the both sides of the stack. Photon collection efficiency was higher than the tile/fiber scheme. Number of total layer was 80, which corresponds to the total thickness of $5\lambda_0$. This simple structure realizes low-cost and easy assembling, but at the same time results in a massless gap between modules.

A testbeam measurement was carried out at KEK $\pi 2$ beamline [3] using 1-4 GeV beams with a PSD, an SMD, and a SPACAL-type test module, which is described in the next section. Measured energy resolution is shown in Fig. 13.4. The results were as expected except the large constant term for pions, which was due to transverse shower

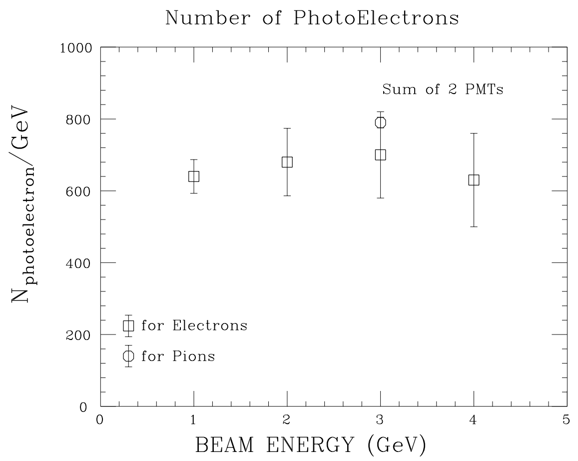

Figure 13.5: Photo-electron yield of ZEUS-type hadron calorimeter test modules for electrons. The same amount is expected for pions since the module was hardware-compensating.

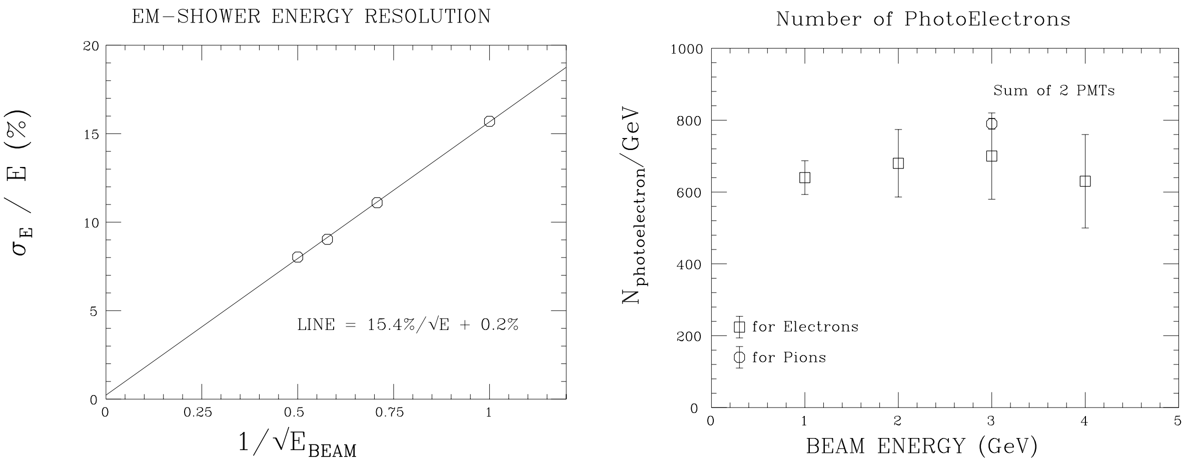

Figure 13.6: Energy resolution (left) and photo-electron yield (right) of ZEUS-type EM test module.

leakage caused by small detector assembly cross section of 60cm×60cm. An e/π ratio, a measure of compensation, was obtained to be 1.01. Also obtained was photo-electron yield of the module to be 160 p.e./GeV on average as shown in Fig. 13.5. This photo-statistics worsens the pion energy resolution from $40.0\%/\sqrt{E}$ to $40.8\%/\sqrt{E}$. This is not a problem for hadron calorimetry. In order to test the response to electrons, another ZEUS-type EM calorimeter test module was made with 4mm-thick lead plates and 1mm-thick plastic scintillator plates. Beam test was carried out at KEK $\pi 2$ beamline with 1-4 GeV beams. Measured energy resolution and photo-electron yield are shown in Fig. 13.6. Obtained energy resolution of $15.4\%/\sqrt{E}+0.2\%$ satisfies expected resolution. The measured photo-electron yield of 660 p.e./GeV has effect on the stochastic term of the energy resolution to worsen it from $15.0\%/\sqrt{E}$ to $15.5\%/\sqrt{E}$. Though this would be acceptable, photon readout scheme with better photon collection efficiency shoule be desirable for EMC. Detailed simulation study is needed to verify this effect.

Though measured energy resolutions were quite satisfactory, we decided not to continue R&Ds of ZEUS-type sandwich calorimeter due to following reasons:

- Longitudinal segmentation is difficult;
- Massless gap made by WLS plates running radially introduces signigficant response anomaly.

13.3.2 SPACAL-type test module

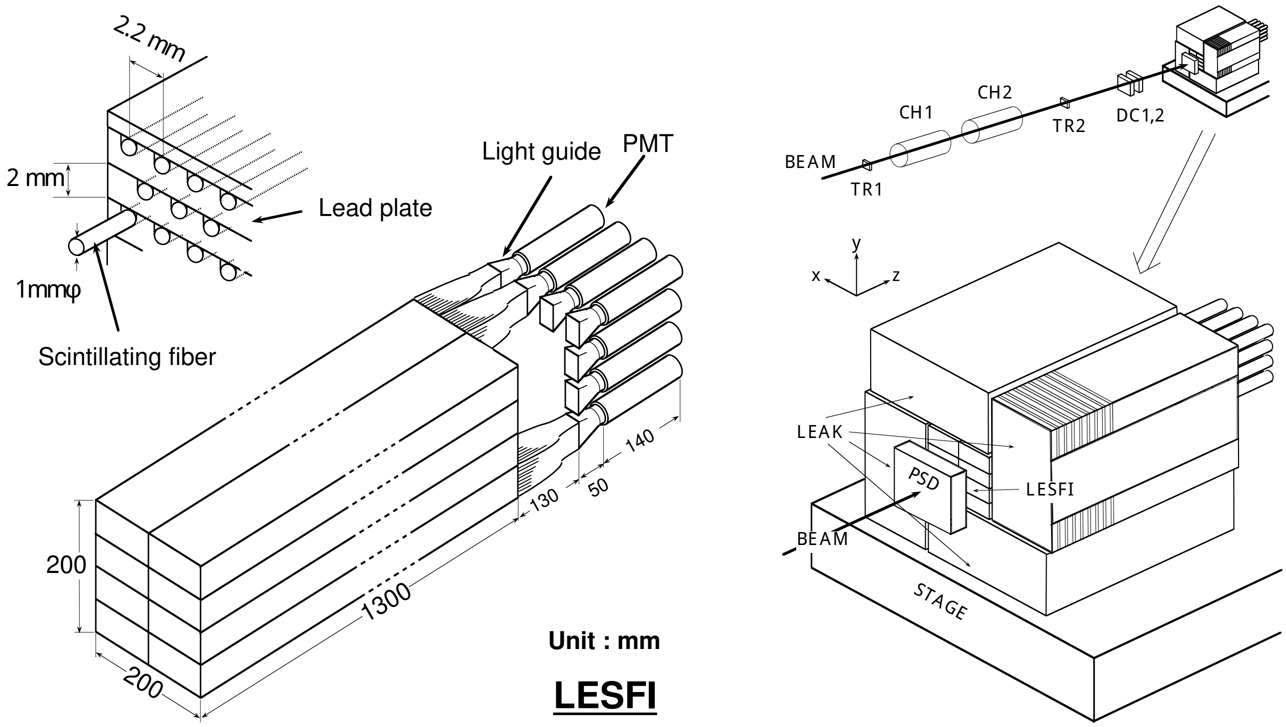

Figure 13.7: Schematical drawing of the SPACAL-type test module (left) and setup of the combined beam test of ZEUS-type and SPACAL-type test modules at KEK-π2 beamline (right).

We also studied SPACAL-type calorimeter in parallel with the ZEUS-type calorimeter at the first stage of the R&D because the SPACAL-type calorimeter was the best-performance calorimeter that time, even though there was no running experiment using SPACAL. Since SPACAL-type calorimeter was quite expensive and extremely elaborating, we built only one module with sizes of 20cm$\times$20cm$\times$130cm as shown in Fig. 13.7. Pure lead plates with grooves are stacked, and 1 mmϕ scintillating fibers are embedded in the grooves. The volume ratio of lead to scintillator is 4:1 for hardware compensation. One module was read out by 16 PMTs to have 4×4 sub-tower structure for transverse shower profile measurement.

Beam test was done at KEK π2 beamline using 1-4 GeV beams [3]. The setup is also shown schematically in Fig. 13.7. One SPACAL-type module at the center was surrounded by the ZEUS-type calorimeter modules, and a PSD was set in front of the SPACAL module for some measurements.

Measured energy resolutions are shown in Fig. 13.8. The results are parametrized as

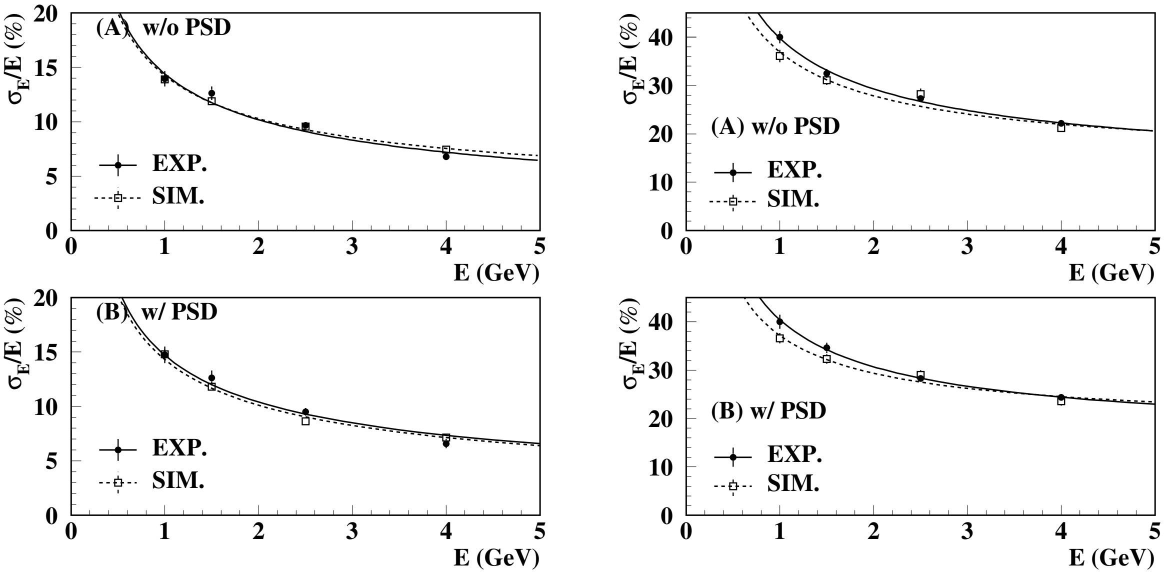

Figure 13.8: Energy resolutions of SPACAL-type test module for electrons (left) and for pions (right). Bottom figures are for measurements with PSD in front, and top ones are without PSD. Dotted lines are results of GEANT simulation.

$$\frac{\sigma_E}{E} = \frac{(14.4 \pm 0.3)\ \%}{\sqrt{E(\mathrm{GeV})}} \oplus (0.0 \pm 1.4)\ \% \quad \text{for electrons,}$$
$$\frac{\sigma_E}{E} = \frac{(38.1 \pm 1.3)\ \%}{\sqrt{E(\mathrm{GeV})}} \oplus (11.6 \pm 1.4)\ \% \quad \text{for pions.}$$

These resolutions were very good except the large constant term due to transverse shower leakage. We also obtained pion rejection factor of 1/200 with electron efficiency of 98% using PSD pulse height and transverse shower profile. This rejection score is not very high because it is difficult to separate e/π with transverse shower profile at low energies ; longitudinal profile does better.

In conclusion of the series of R&Ds, we decided not to continue R&Ds of SPACAL-type calorimeter due to following reasons:

- Longitudinal segmentation is very difficult;
- Preshower and shower-max detectors can not be integrated naturally;
- Really expensive and elaborating.

13.3.3 Tile/Fiber Test Module

Tile/fiber structure is characterized by a wavelength shifting fiber embedded in a plastic scintillator tile. This enables compact optics for light collection and transfer from scintillators to photon detectors without sacrificing photon yield so much. This scheme was extensively studied by SDC group[4], and then by CDF group[5] with slightly different fiber layout. The tile/fiber calorimeters have been widely adopted by CDF, STAR[7], CMS[6], and so on. For the JLC calorimeter, the tile/fiber sturcture with hardware compensation was adopted as a revised baseline design in 1996, and systematic R&Ds were initiated. Following bench tests of each component, test modules were constructed for generic shower study and realistic performance study, and series of beam tests were carried out at KEK and at FNAL. In the following sections, detail of the R&Ds are described.

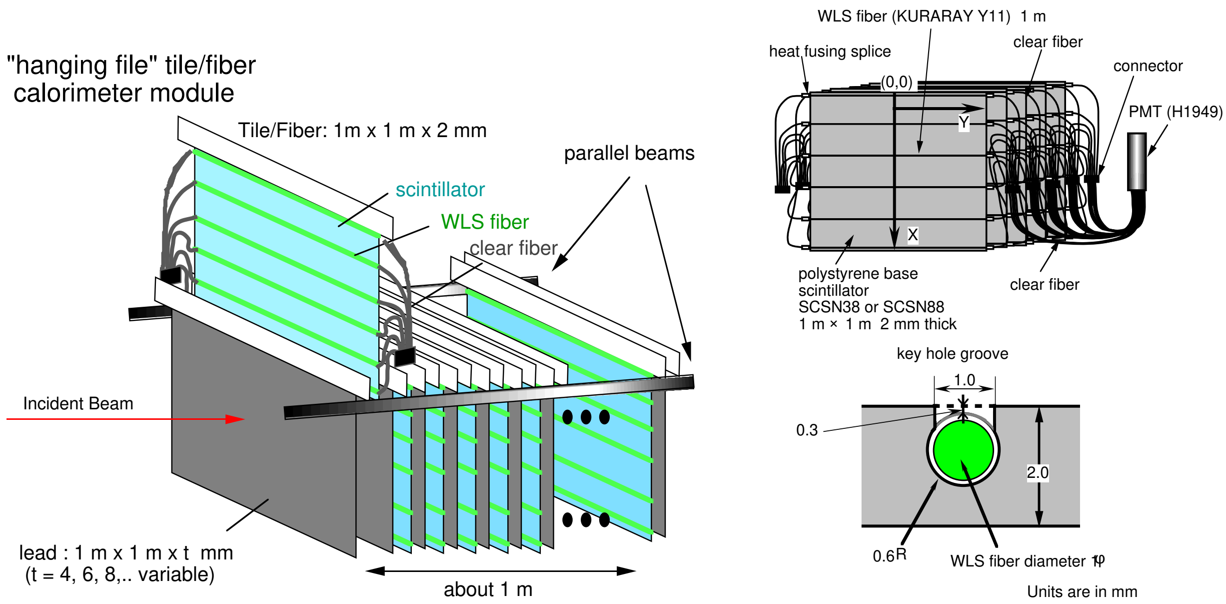

Figure 13.9: Schematical view of straight-groove hanging-file test module (left), and optical readout scheme (right).

1) Generic Studies with Straight-groove Module

Though extensive R&Ds had been carried out by SDC/CDF group before 1996, combination with hardware compensation raised two open questions:

- First of all, possibility of hardware compensation itself with tile/fiber configuration must have been established. There were several calculations and measurements on compensation with lead and plastic scintillator sampling calorimeters[3, 8, 9]. However those results had significant discrepancies with each other. Addition of fiber-routing plates for tile/fiber configuration was another unknown factor on compensation. This might affect the compensation condition. Those problems must have been examined before making calorimeter module of tile/fiber design.

- In order to realize required energy resolution with hardware-compensating composition using lead absorber, very thin scintillator plates of 1mm-thickness should be used for EM calorimeter, and 2mm for hadron calorimeter. Photon yield, uniformity, and mechanical feasibility must have been examined for such thin sciltillator plates.

A test module with hanging-file structure was constructed to examine possibility of hardware compensation. The structure is schematically shown in Fig. 13.9. Lead plates and scntillator plates, and acryl plates if necessary, were hung over a pair of supporting beams to enable re-configuration for generic studies. As absorbers, 4mm-thick lead plates and 2mm-thick lead sheets were used to change the lead thickness from 4 mm to 16 mm by 2mm-step. The thicknesses of plastic scintillator plates and acryl plates, on the other hand, were fixed to be 2 mm. Transverse size of the plates were 1m×1m for good shower containment.

Photon-readout scheme is also shown in Fig. 13.9. The scintillator plates had six straight grooves of key-hole cross section, where 1 mmϕ WLS fibers were embedded. Distance between the grooves, 20cm, was determined to re-use the scintillator plates for the tile/fiber module. Fibers from five successive scintilator plates on each side were ganged to form a superlayer, and were read out by one PMT. There were 42 superlayers in the configuration with 4mm-thick lead plates, and detailed study on longitudinal shower profile was carried out. In the case of 8mm-thick lead plates, there were 24 superlayers, resulting in the total thickness of $6\lambda_0$.

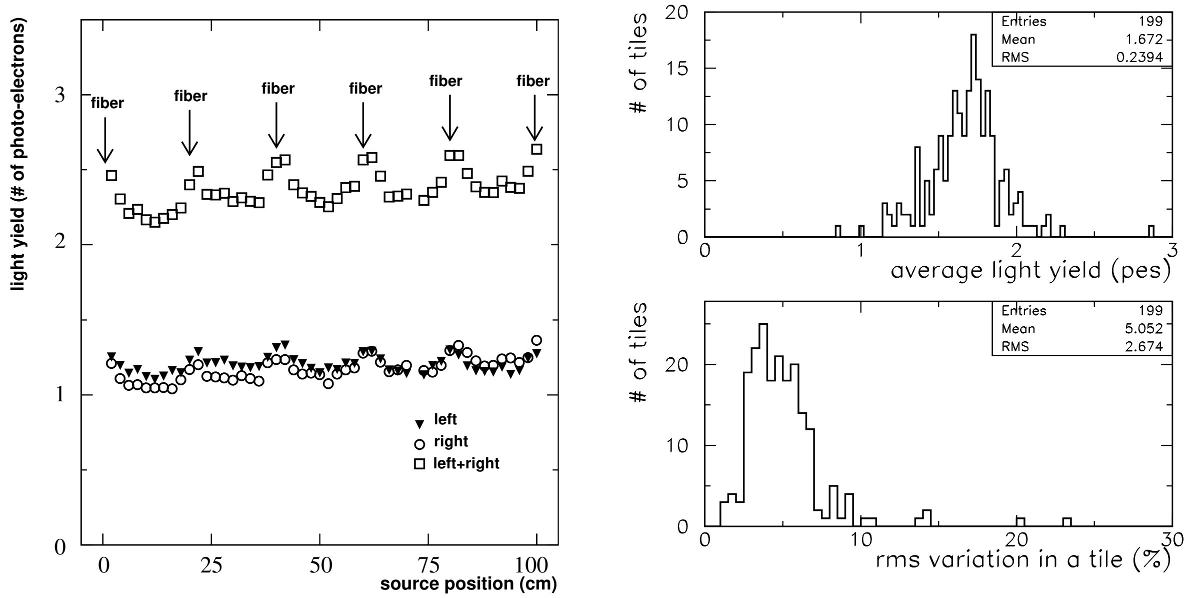

Figure 13.10: Non-uniformity of photo-electron yield over one scintillator plate (left), distributions of its average (right-top) and RMS (right-bottom).

Response of scintillator plates were measured with an RI source before assembling. Non-uniformity of photo-electron yield over one scintillator plate and distributions of its average and RMS are shown in Fig. 13.10. Since the fiber distance is rather large, average photo-electron yield is only 1.6 p.e./MIP. Measured response map shows prominent peaks at the embedded WLS locations. Effects of measured non-uniformity and distribution of average photo-electron yield on calorimeter responses were examined by GEANT simulation, and concluded not to be significant for hadrons [10].

Energy Measurement

Series of beam tests were carried out at KEK $\pi 2$ beamline with beam energies from 1 GeV to 4 GeV [10]. Fig. 13.11 shows energy resolution for pions and e/π response ratio versus lead plate thickness. Target energy resolution is achieved with lead plates of 8mm-thick or thinner. The hadron energy resolution of $33.6\%/\sqrt{E}$ achieved with 4mm-thick lead plates are one of the best hadron energy resolution achieved so far. In Fig. 13.11, dependence of energy resolution on lead thickness d is parametrized as $\sigma_E = \sqrt{\sigma^2_{intrinsic} + (\sigma^2_{sampling} + \sigma^2_{photostat})/d}$, neglecting the constant term. Intrinsic hadron shower fluctuation was obtained to be 24.4±0.7% as a result of the fitting. This is significantly larger than previously reported value of 13.4±4.7% by ZEUS [11], which was derived only from two sampling frequencies. However this could simply be due to the difference of incident energy.

It is concluded from the fitting that hardware compensation should be achieved with 9mm-thick lead plates in the case of 2mm-thick plastic scintillator plates.

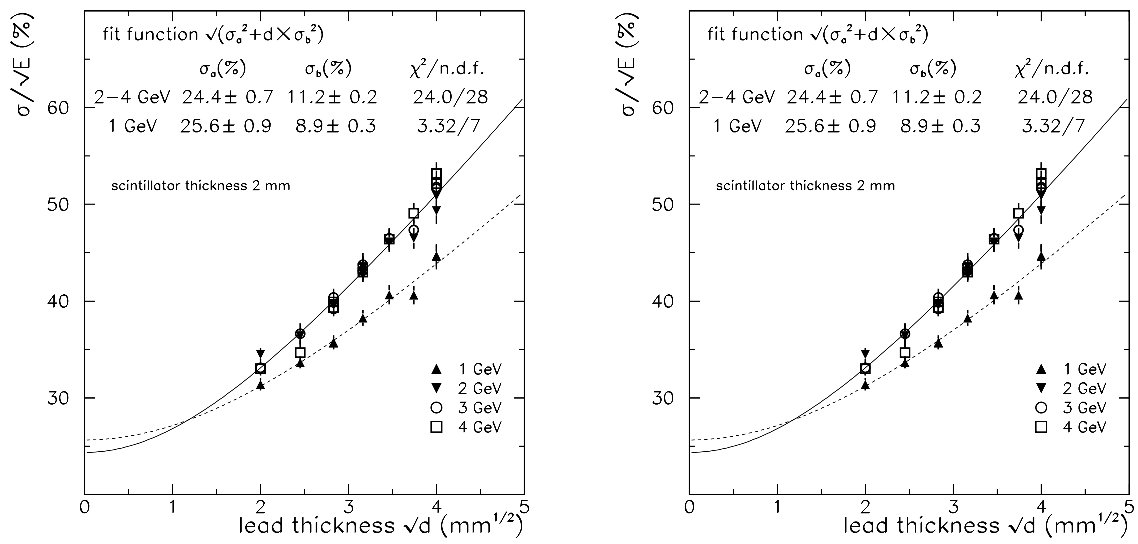

Figure 13.11: Energy resolution for pions (left) and e/π ratio (right).

In order to check effect of fiber-routing acryl plates on compensation, three configurations are tested in the case of 8mm-thick and 16mm-thick lead plate configurations:

- no acryl plates were used (lead and scintilator only);
- an acryl plate was put upstream-side of every scintillator plate;
- an acryl plate was put downstream-side of every scintillator plate.

The motivation of measurement with 16mm-thick lead plates was such that compensation might be achieved with 16mm-thick lead plates + 2mm-thick scintillator plates + 2mm-thick acryl plates, resulting in the volume ratio of lead to total plastic to be 4:1.

Effects of acryl plates on the energy resolution and e/π ratio is summarized in Table 13.4. It is seen from the results of 8mm-thick lead-plate case that acryl plates does not destroy the hardware compensation if they are placed downstream-side of scintillator plates. Hadron energy resolution, however, gets slightly worse by their presence regardless of their location. These behaviour is not clear in the case of 16mm-thick lead-plate case due to large error. However it is clear that compensation was not achieved, meaning that acryl plates do not contribute to the volume-ratio counting.

lead thickness	position of acryl	σ_E/E for electrons	σ_E/E for pions	e/π ratio
8mm	No acryl plates	(12.0±0.5)%	(20.5±0.4)%	1.03±0.02
	Acryl plates upstream	(11.6±0.5)%	(22.7±0.4)%	1.07±0.02
	Acryl plates downstream	(12.0±0.5)%	(22.8±0.4)%	1.01±0.02
16mm	No acryl plates	(18.1±1.1)%	(27.1±0.7)%	0.90±0.04
	Acryl plates upstream	(18.1±1.1)%	(28.1±0.7)%	0.95±0.04
	Acryl plates downstream	(18.1±1.1)%	(28.8±0.7)%	0.87±0.04

Table 13.4: Energy resolutions and e/π ratios with and without acryl plates for 4 GeV/c electrons and pions.

Shower Fluctuation Analysis

Longitudinal shower profile and its event-by-event fluctuation was studied with configuration of 4mm-thick lead plates, which had 42 longitudinal samplings (superlayers). The purposes of this study is;

- Improve hadron energy resolution (software weighting);
- Construct parametric hadron shower generator with realistic fluctuation;
- Obtain e/π separation capability as a function of the longitudinal segmentation of the calorimeter.

Analysis has been done for both EM and hadron showers following the work by CDF for EM shower analysis[12]. Correlation plots between pulsehieght fluctuations for different superlayers are shown in Fig. 13.12 for raw fluctuations δ_i and for orthogonalized fluctuations $\tilde{\delta}_i$. Orthogonalization is done by diagonalizing correlation matrix of raw fluctuation, and obtaining the eigen vectors for fluctuation. In the case of electrons, no correlation is seen between amplitudes of the orthogonalized eigen vectors. On the other hand, $\tilde{\delta}_i$ for pions have correlation even after orthogonalization procedure, meaning that orthogonalization of hadronic fluctuation is not yet successful. Therefore parametrization of hadron shower fluctuations with orthogonal parameter set has not been completed yet.

Pulseheight fluctuation can be used to improve e/π identification, which is usually done by shower profile only. Deviations of measured pulseheights from electron profile template and from pion profile template are normalized by typical fluctuation for each particle, and likelihood to each particle are calculated. Distribution of electron-ness and pion rejection capability are shown in Fig. 13.13. Number of mode in the right figure is number of eigen vectors of pulseheight fluctuation used in the analysis. Since there are 42 superlayers, there are 42 orthogonal eigen vectors to represent pulseheight fluctuation. Using six or seven major eigen vectors achieves almost the best score ; higher minor eigen vectors are noisy, and using them does not improve the score. For single-particle e/π separation, therefore, six or seven longitudinal segmentation should be good enough if they are segmented in optimum way.

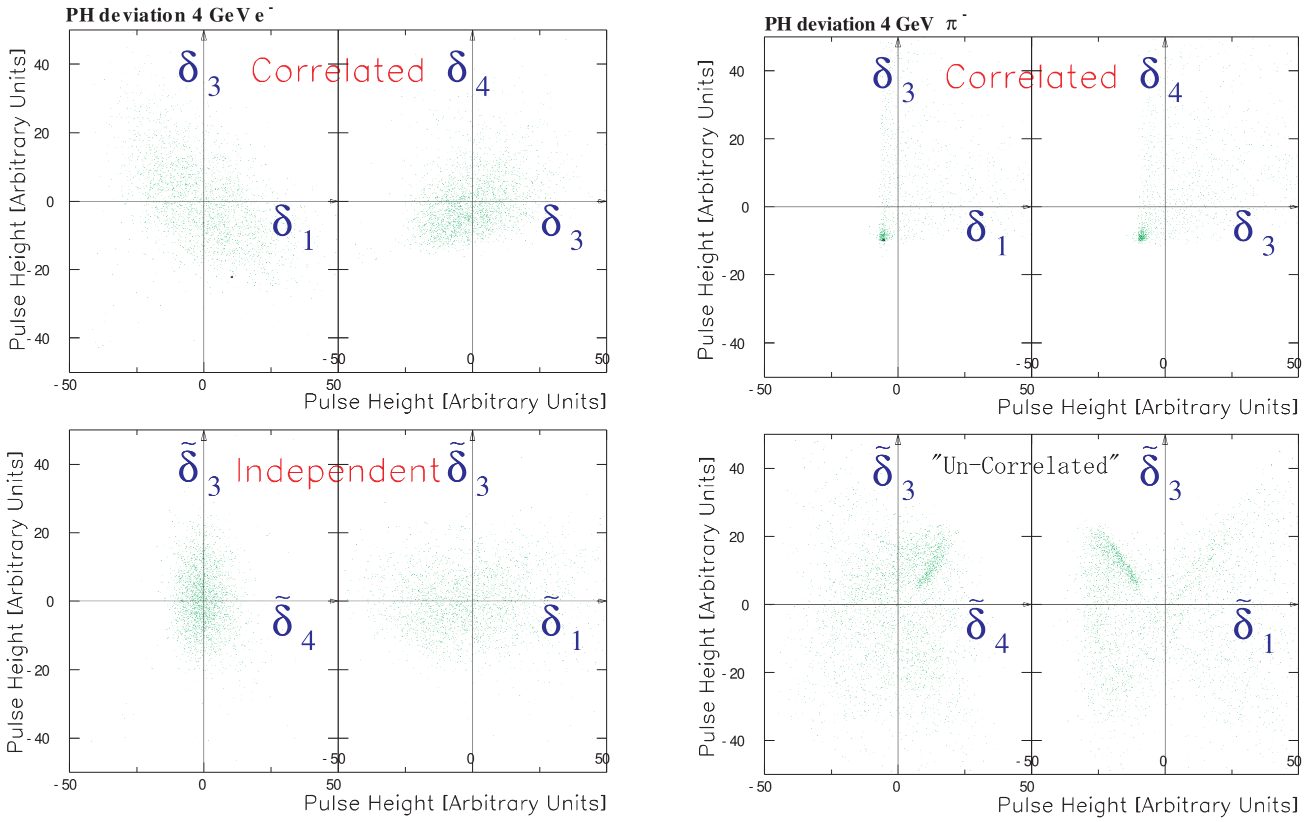

Figure 13.12: Correlation between pulsehieght fluctuations for different superlayers for electrons (left) and for pions (right). Upper distributions are for raw fluctuations, and lower ones are after orthogonalization.

2) Study of Tile/Fiber Module

Based on the results of the generic studies and tile bench tests, the straight-groove module was rebuilt to be a tile/fiber calorimeter module. The design of the module is schematically shown in Fig. 13.14. The module was composed of a front section (FCAL) and a rear section (RCAL).

In the FCAL part, the 1m×1m plastic scintillator plate was modified to be a scintillator tile assembly as shown in Fig. 13.14. Twenty-five tiles with size of 20cm×20cm×2mm-thick were arranged on a fiber-routing acryl plate to form 5×5 tower structure. Four sides of the tiles were painted white with TiO_2-based emulsion, and the assembly was covered with white PET films for better light collection efficiency. The tile had a σ-shaped groove with a key-hole cross section, where a WLS fiber was embedded. The WLS fiber was connected to a clear fiber by heat splicing at the exit from the tile. The clear fiber then ran in the groove on the fiber-routing acryl plate to exit from the detector assembly, and was connected to a photon detector. Photo-electron yield and uniformity over a tile measured with β rays from an RI source are shown in Fig. 13.15. Obtained photo-electron yield is translated to the calorimeter response of 83 p.e./GeV for 8:2 configuration, about the half of the ZEUS-type modules. This slightly worsens the stochastic term of hadron energy resolution from $40\%/\sqrt{E}$ to $41\%/\sqrt{E}$, which is not a problem for hadron calorimetry. The measured non-uniformity was estimated using GEANT3 simulation to

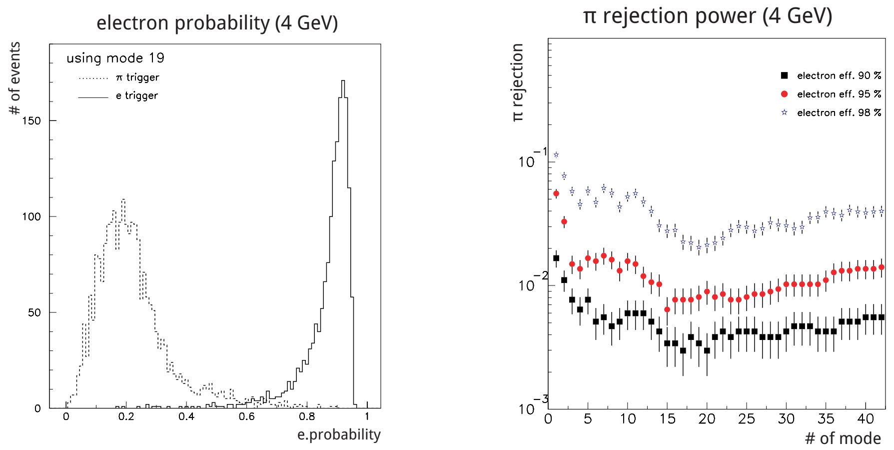

Figure 13.13: e/π separation by pulseheight fluctuation from template distributions for electrons and pions. Left histogram is electron probability distribution for electron and pion samples, and right plot is pion rejection factor as a function of number of modes (used eigen vectors).

introduce systematic uncertainty of 0.3% on average on energy resolution measurement. This, again, is not significant.

These tile assemblies were interleaved with 8mm-thick lead plates. There were 80 layers of the tile assemblies in FCAL in total. They were divided into four sections longitudinally, each of which contained 20 layers. One quadrant of a tower were read out by one PMT.

Following the tile/fiber part, unmodified straight-groove section remained as RCAL. There were two superlayers in RCAL in the case of low energy beam test at KEK. In the case of high energy beam test at FNAL, ten superlayers were installed, the last of which did not have lead absorbers to be used for muon tagging. RCAL also had 8mm-thick lead plates as absober.

The layouts of the beam tests at KEK and at FNAL are schematically shown in Fig. 13.16. Both setups are quite similar except for that there were momentum-analyzing devices at FNAL beam test, and that SRD was used for electron identification at FNAL instead of Cerenkov counters. Details of the setup and analysis are given elsewhere [10, 13]. Energy of the beam was 1-4 GeV and 10-200 GeV at KEK and at FNAL, respectively. The beam was unseparated, and particle identification was done off-line. In the case of FNAL test, however, electorn-rich and pion-rich conditions were realized by selecting appropriate converters/absorbers on the beamline. Tower-to-tower gain calibration was done using penetrating muons.

Energy Measurement

Measured energy resolution, linearity, and e/π ratio are shown in Figs. 13.17 and 13.18. The energy resolution is slightly worse than those shown in Fig. 13.11, and is consistent with that of the straight-groove module with acryl plates interleaved shown in the Table 13.4. We can therefore conclude that acryl plates used for fiber-routing do deteriorate the energy resolution, regardless their location. On the other hand, the e/π ratio is consistent with 1.0, and hardware compensation is established to be retained in the case of the tile/fiber structure if each acryl plate is located downstream-side of each

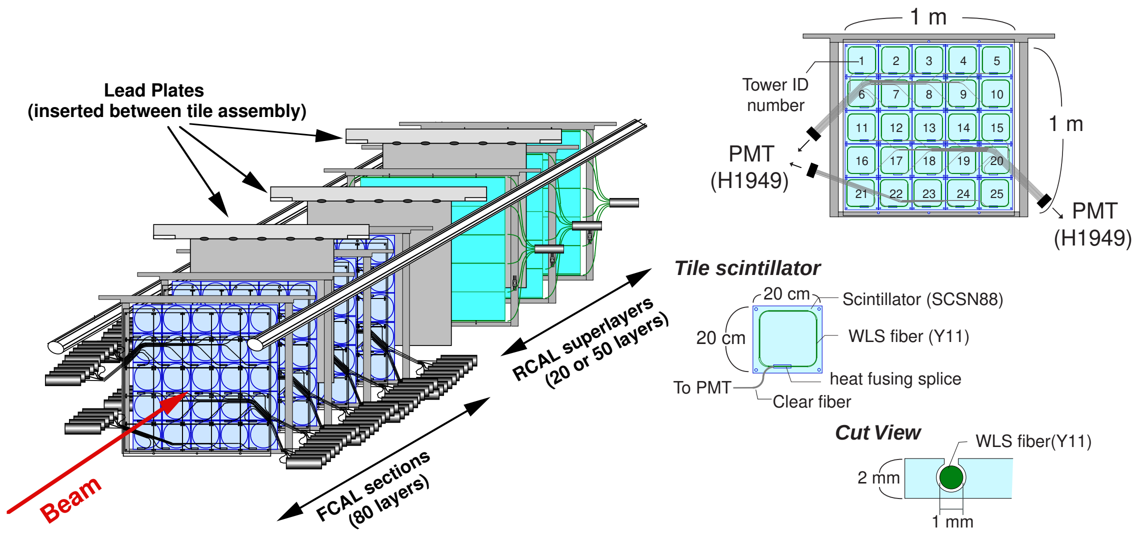

Figure 13.14: Schematic view of the tile/fiber test module (left) and layout of fibers and tiles (right).

scintillator assembly.

If we stick to the hadron energy resolution of $40\%/\sqrt{E}$, sampling frequency of the HCAL should be finer than 8mm-thick lead plates plus 2mm-thick plastic scintillator. However measured hadron energy resolution of $46\%/\sqrt{E}$ may be acceptable for physics analysis. This should be examined by further simulation study.

Tower Property

Cross-talk between towers measured with electron central injection are shown in Fig. 13.19. Amount of cross talk to adjucent towers are 1%-level. This is consistent with the optical crosstalk at the bench test measured with an RI-source. Cross talk of this level is negligible to hadron shower analysis. For EMC of finer-granularity option, however, cross talk may have significant impact, and needs to be examined.

Response at the tower boundary are shown in Fig. 13.20. Energy measurement for pions may have enhancement of about 3% at the region where WLS fibers are embedded. This is consistent to the non-uniformity at the bench test shown in Fig. 13.15. This enhancement is not significant when EMC is loacted before the HCAL and response smears out. On the other hand, energy measurement for electrons has prominent enhancement at the boundary. This must be equalized by ajusting reflection index of tile surface around the WLS when EM modules are constructed.

3) EMC R&Ds at Testbench

Photo-electron yield of 1mm-thick scintillator for EM calorimeter was measured for 10cm$\times$10cm tiles. It also had a σ-groove, and 0.7 mmϕ WLS fiber was used. The average photo-electron yield was obtained to be three as shown in Fig. 13.21. This corresponds to 350 p.e./GeV for compensating calorimeter, and is not sufficient for EM calorimetry. Comparison between 20cm$\times$20cm$\times$2mm-thick tiles and 10cm$\times$10cm$\times$1mm-thick tiles suggests that photo-electron yiled is inversely proportional to the area of tiles, since we know from independent measurement that photo-electgron yiled is proportional to the tile thickness.

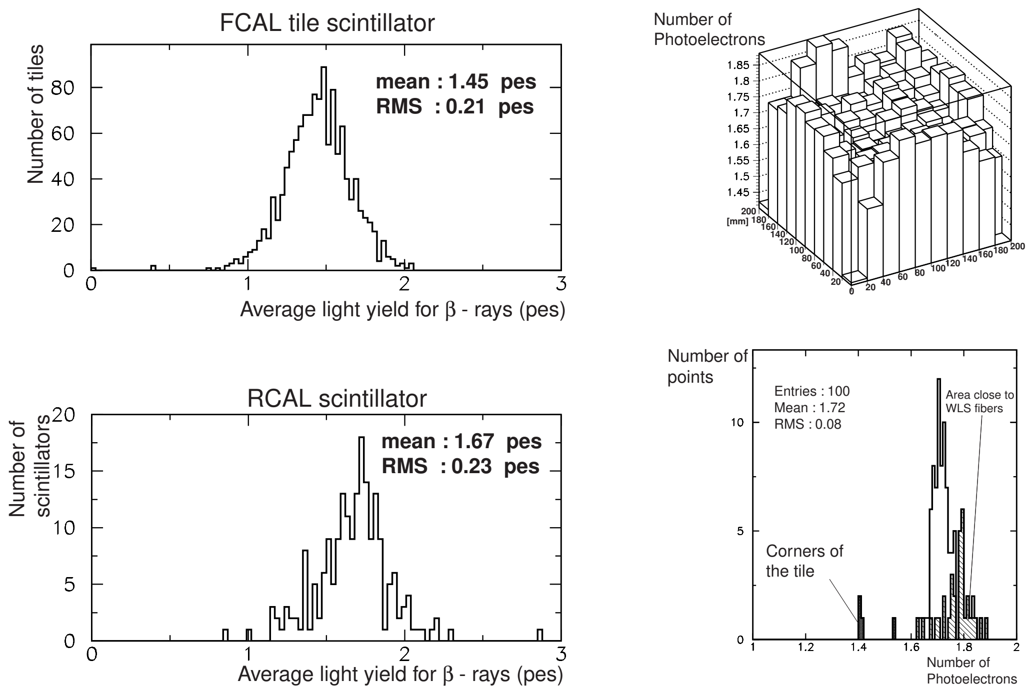

Figure 13.15: Average photo-electron yield for tiles (left-top), average photo-electron yield for straight-groove plates (left-bottom), uniformity over one tile (right-top), and distribtion of photo-electron yield for a tile (right-bottom).

Smaller tiles such as 5cm×5cm is considered to have sufficient photo-electgron yiled. This, together with non-uniformity, should be established by further measurement.

R&Ds on another option of finer-granulartiy EMC, made of stacks of scintillator strip arrays like SMD, are in progress. This option requires huge number of photo-detector channels, and has become possible by recent advances in multi-channel HPD and EBCCD. Whether we can remove ghosts efficiently or not must be investigated with a full simulator.

Bench tests on strip properties were carried out for various strip sizes with thickness of 2 mm. Non-uniformty of photo-electron yield over a strip was measured to be 4.8% at most for 1cm-wide strips as shown in the Fig. 13.22, and is acceptable for EMC. Average photo-electron yield, on the other hand, is 4.6 p.e./MIP. This corresponds to 260 p.e./GeV

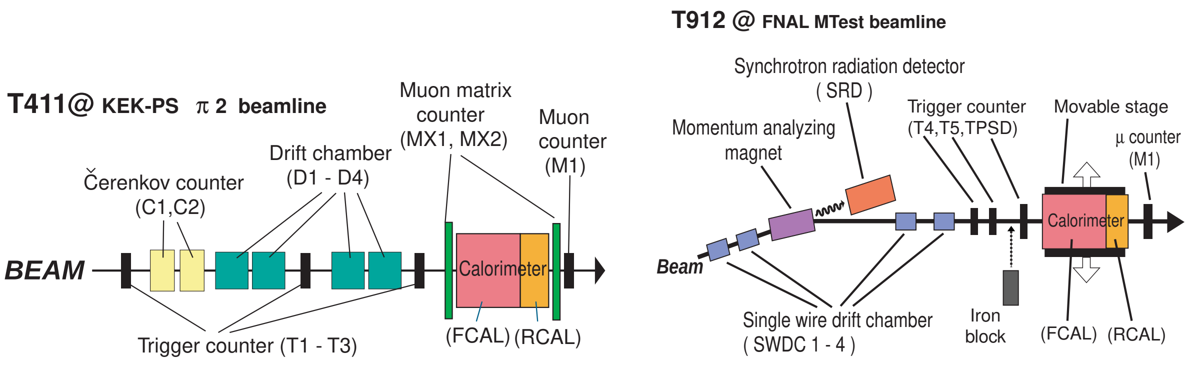

Figure 13.16: Setup of the beam test at KEK (left) and at FNAL (right).

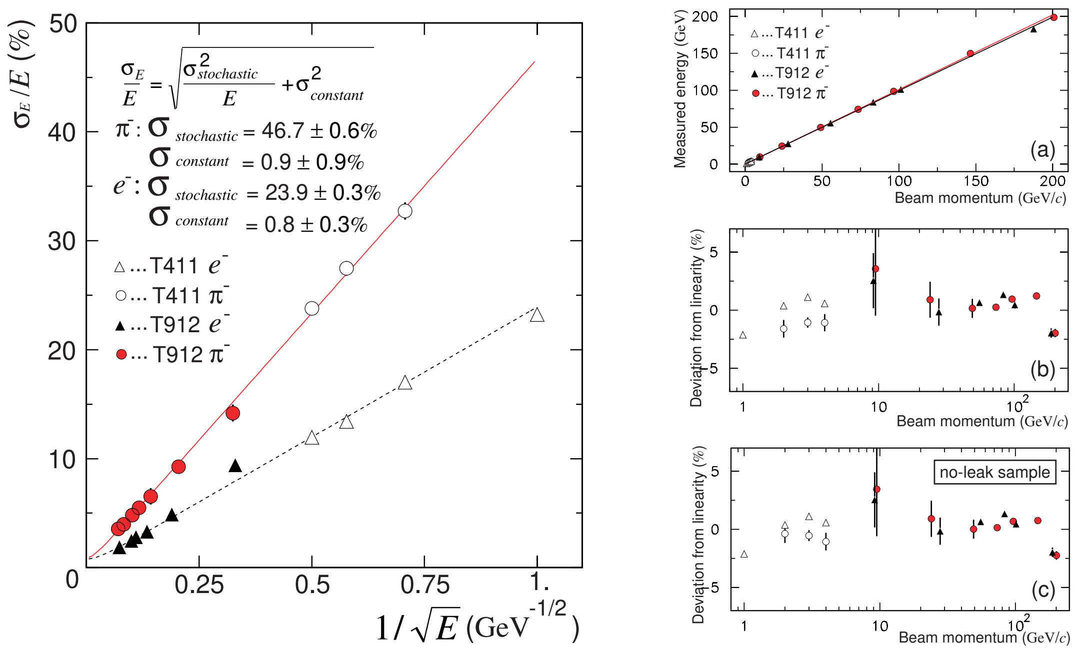

Figure 13.17: Energy resolution (left) and linearity (right) of the tile/fiber test module.

in the case of compensating EMC, and needs further improvement. However, if software compensation is possible even with the orthogonal $\theta - \varphi$ strip layout, thicker strips can be used, and photo-electron yield will not be a problem. Detailed full simulation studies are again needed to examine apllicability of software compensation for this scheme.

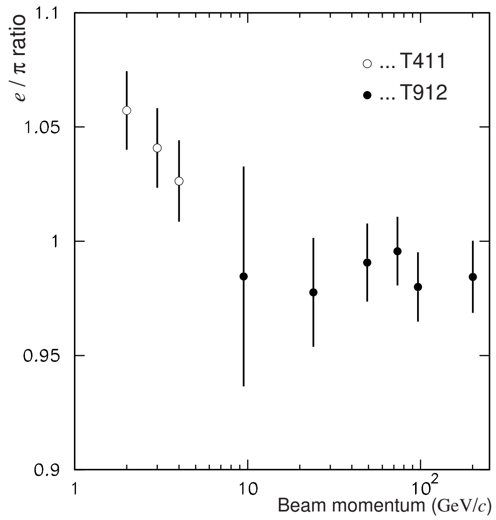

Figure 13.18: e/π response ratio of the tile/fiber test module.

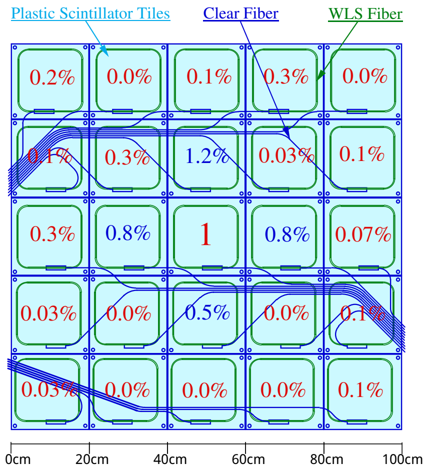

Figure 13.19: Cross talk between towers for the tile/fiber test module.

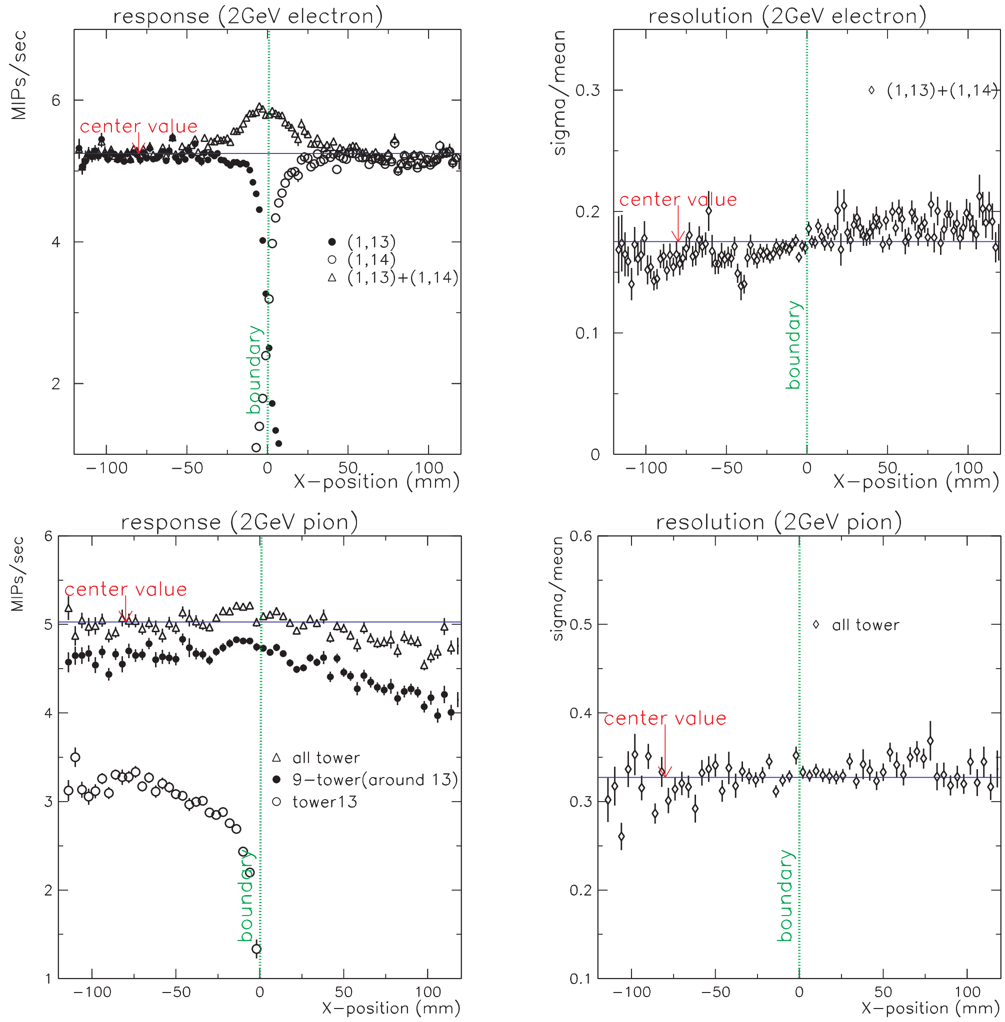

Figure 13.20: Tower boundary response of the tile/fiber test module. Top figures are responses for electrons, and bottom ones are for pions. Left figures are energy measurement, while right ones are energy resolutions.

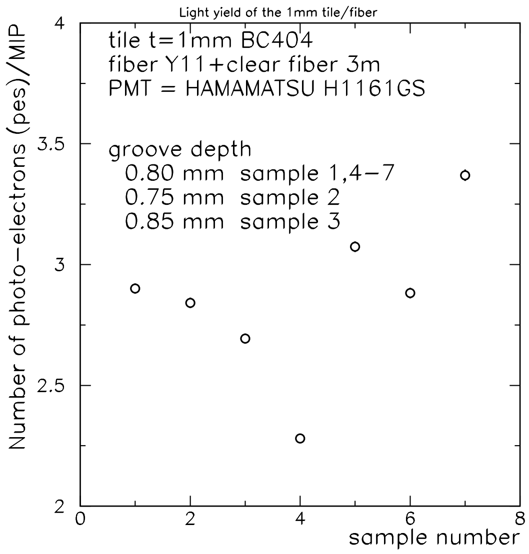

Figure 13.21: Photo-electron yield of 10cm×10cm×1mm-thick tiles.

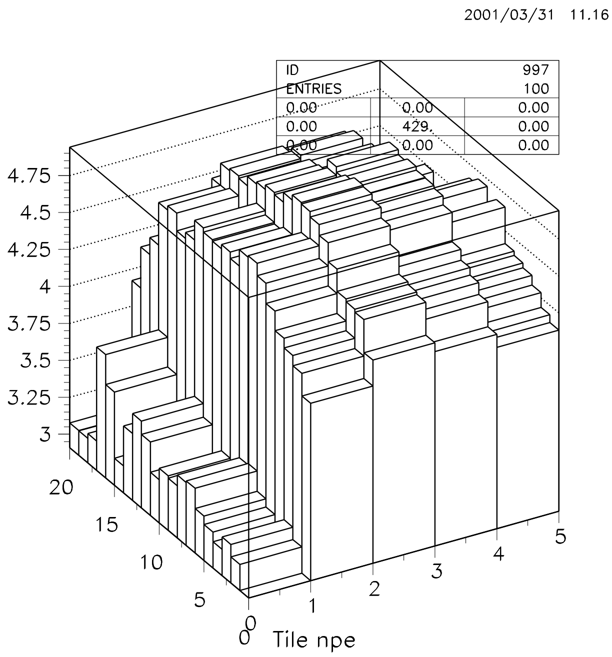

Figure 13.22: Photon yield uniformity over a 1cm-wide strip.

13.3.4 Preshower and Shower-max detectors

The purpose of PSD and SMD are to identify $e/\pi^{\pm}/\gamma/\pi^0$, and improve cluster separation and track-cluster association. For this purpose, fine segmentation is necessary for SMD. First we studied SMD of Si-pad array as HES[14] of ZEUS. Test modules were made with Si-pad array firstly with pad size of 1cm×1.5cm and array size of 18×12, then secondly with pad size of 1cm×1cm and array size of 16×16 with improved readout electronics. Beam tests were carried out in combination with PSD and hadron calorimeter modules[15].

Later on, we moved to the scintillator-strip option since:

- Si-pad SMD was thought to cost too much;
- Scintillator-strip SMD used the same technique as the tile/fiber calorimter, and was easily integrated with calorimeter.

Since the size of the 3Tesla-version baseline JLC calorimeter is now much smaller than the previous one, the first reason may be no more true. However re-examination of the possibility of Si-pad option has not yet started.

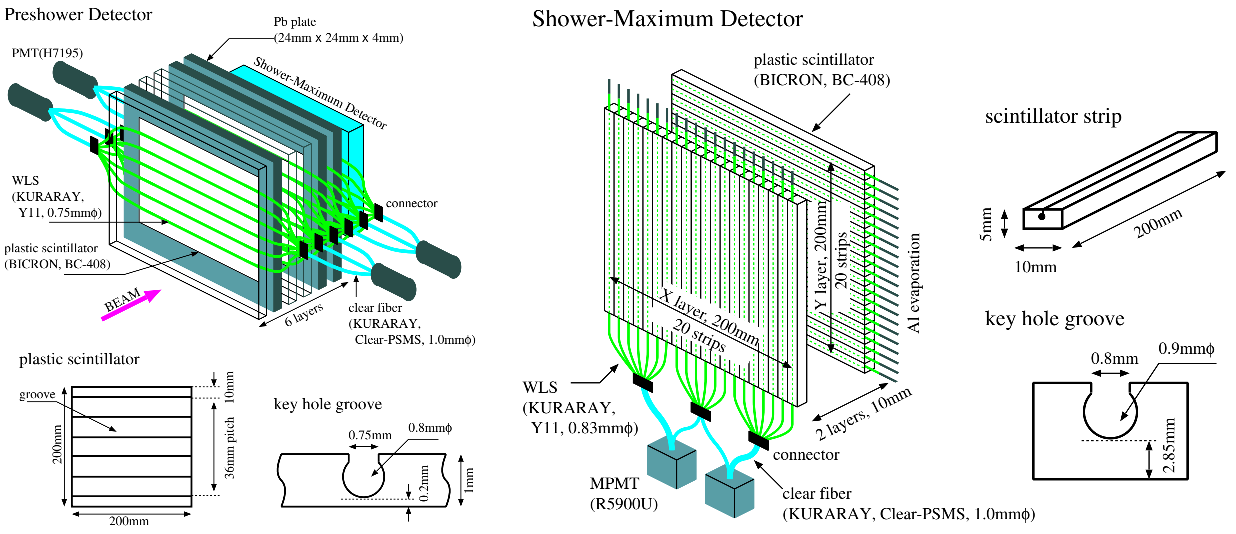

Figure 13.23: Schematical drawing of PSD (left) and SMD (right).

According the the baseline design, we built test modules of PSD and SMD, and carried out a beam test at FNAL in combination with the tile/fiber hadron calorimeter [16]. The designs of PSD and SMD modules are schematically shown in Fig. 13.23. Photons from scintillators were read out by WLS fiber assembly in both PSD and SMD. In the case of SMD, fibers were connected to multi-channel PMTs, and each strip was read out separately.

In order to separate electrons from pions, three variables are defined:

- S is a measure of lateral shower spread defined as $S = \sqrt{\sum_i d_i^2 E_i / E_{tot}}$
- D is a measure of longitudinal shower distribution defined as $D = \sum_j z_j E_j / E_{tot}$
- R is a ratio of energy in PSD to total energy.

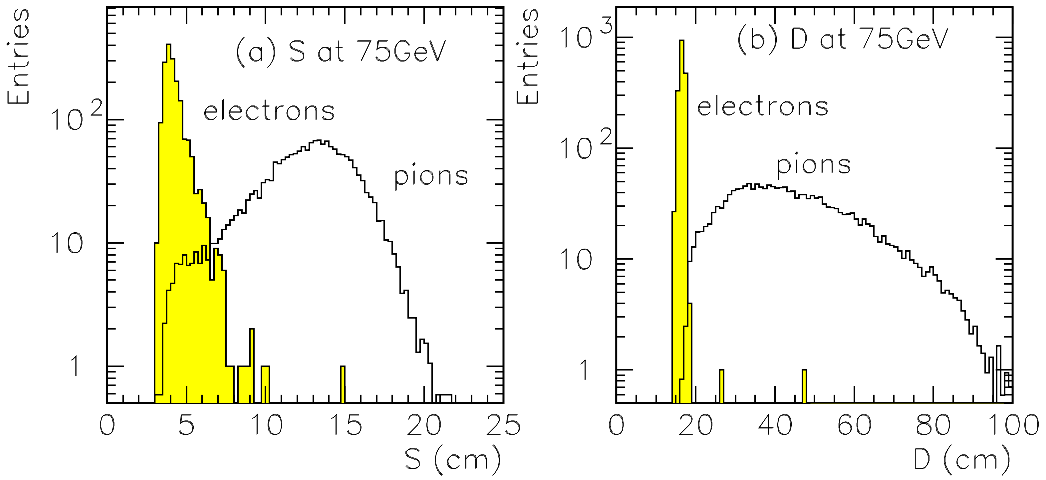

Figure 13.24: e/π separation capability of S-variable (left) and D-variable (right).

Examples of e/π separation capability of S and D variables are shown in in Fig. 13.24. It is seen that D-variable has excellent performance in e/π separation, and thus that longitudinal segmentation is quite important. Measured e/π separation capabilities are shown in Fig. 13.25 and summarized in Table 13.5. Obtained score of mostly bettern than 1/1000 are comparable to other measurements [17], and is satisfactory.

Hit multiplicity of SMD can also be used to identify electrons. By requiring more than 10 hit-strips out of 40 strips, pion rejection factor of about 10 can be achieved with electron efficiency of 98%. However this has strong correlation with R-value, and is not included in the table 13.5.

Method	S value and R_{PS2}			D value and R_{PS2}			D and S values		
ϵ_e (%)	90	95	98	90	95	98	90	95	98
r_π at 50 GeV	473	312	180	1274	1104	720	1183	828	753
r_π at 75 GeV	657	487	343	1258	1162	944	1510	1162	888
r_π at 100 GeV	984	656	281	1640	1406	1406	984	820	656

Table 13.5: Pion rejection factors with the combinations of R_{PS2}, S and D values.

Measured position resolution is shown in Fig. 13.26. Present result is much worse than the baseline requirement of better than 1 mm for energies higher than several GeV. This is due to saturation and cross talk of PMTs, and should be solved before going to the next step.

The WLS fiber assembly costs significant amount of the total cost of scintillator-array SMD. In order to reduce the total cost of SMD, an option which use photo-diodes (PDs) instead of WLS fiber assembly are being studied. Silicon PIN PDs or APDs are attached at the both end of the strips, and photons are directly read out by the PDs. Direct punch-through of charged partilces will be identified by double-layer scheme; a blind PD is pasted behind the detector PD.

Studies so far indicates that PIN PDs do not have enough sensitivity, and studies

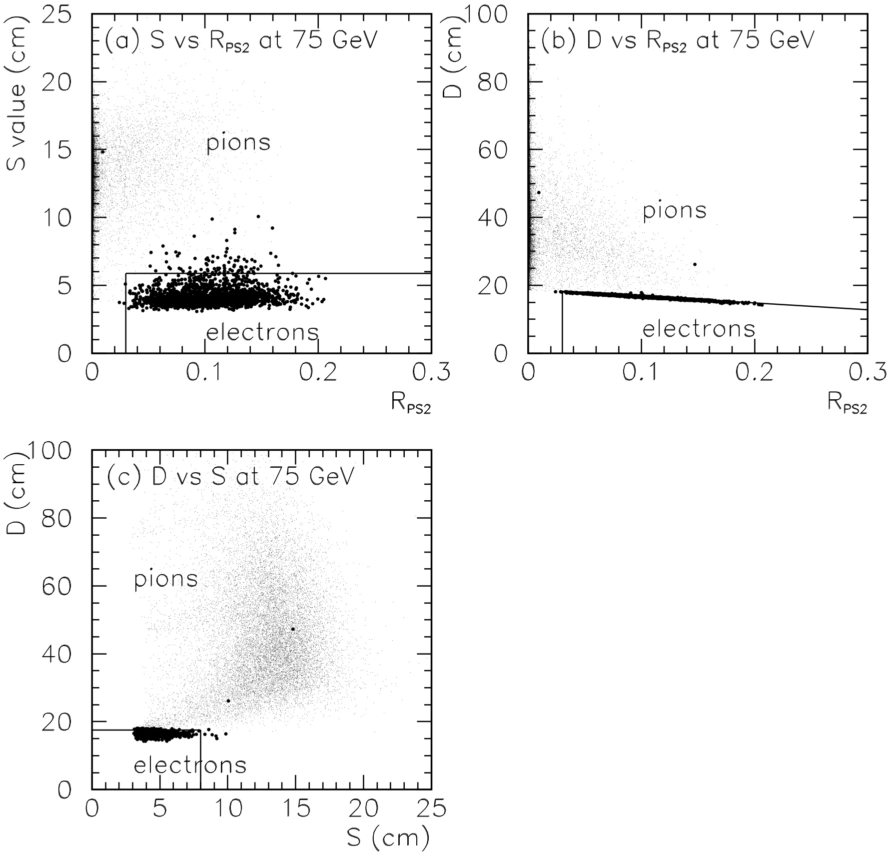

Figure 13.25: e/π separation capabilities using combinations of S, D, and R variables..

with APDs are in progress. Much more studies are needed to get some conclusion on this option.

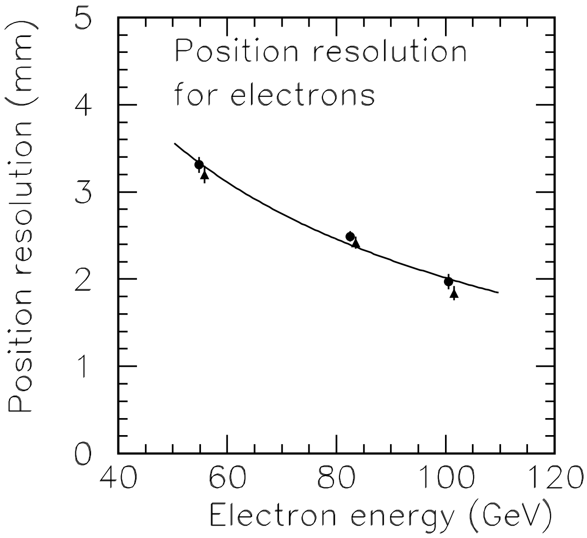

Figure 13.26: Position resolution of SMD.

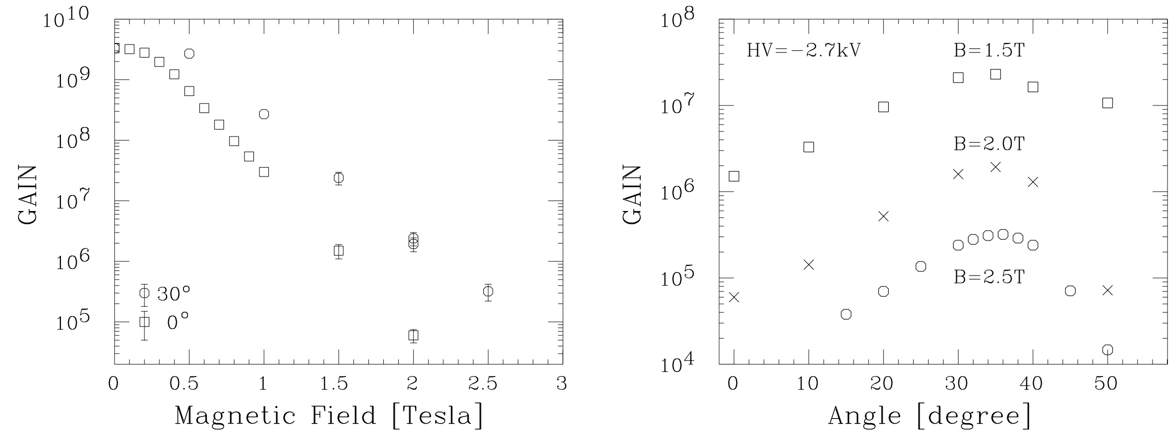

Figure 13.27: Magnetic field dependence of FMPMT gain. Horizontal axes are magentic field strength (left) and angle between magentic field and PMT axis (right).

13.3.5 Photon Detectors

The whole calorimeter system is designed to be located inside the superconducting solenoid. Thus photon detectors operational in strong magnetic field are needed. In the case of crystal calorimeter, the light yield is large and popular PIN silicon photodiode or APD can be used. On the other hand, in the case of sampling calorimeters, especially compensating calorimeters, the light yield is relatively poor and high-gain high-sensitivity photo-detector is needed.

One conventional solution is fine-mesh photomultiplier tubes (FMPMTs). This has been widely used for magnetic field below 1 Tesla. Possibility to improve its performace at higher magnetic field was first investigated.

Another option is hybrid devices such as Hybrid Photodiodes (HPDs) or Hybrid Avalance Photodiodes (HAPDs). Performances of such devices have been extensively studied so far. As the result, these hybrid devices are thought to be the best option at present.

1) FMPMT

In order to keep high gain even in the magnetic field of higher than 1 Tesla, high-gain FMPMTs with 24-stages of dynodes (Hamamatsu H2611SXA) were made and tested with magnetic field up to 2.5 Tesla using SKS spectrometer at KEK [18]. Fig. 13.27 shows magnetic field dependence of the gain. It still had gain of 3×10^5 at 2.5 Tesla when the angle bwtween the PMT axis and magnetic field was 30° even after rapid drop of gain with magnetic field. By extrapolation, it was expected to have gain of 3×10^4 at 3 Tesla. However the gain variation with respect to field strength and PMT angle to the field direction is quite steep. This feature is not disireble, though is not fatal. We therefore concluded that FMPMT can not be the primary solution.

2) Hybrid Devices

HPD consists of a photo-cathode and a PIN photodiode facing to each other with a narrow vacuum gap in between. This is essentially insensitive to the axial magnetic field as is easily seen from the structure shown in Fig. 13.28. High-voltage is applied between the photocathode and the PIN silicon diode. Emitted photoelectrons are accelerated by this field, and injected to the PIN diode. Those photoelectrons deposits their energy when they pass the depletion layer and create electron-positron pairs. Roughly speaking, since excitation energy of one electron-position pair is 3.6 eV, gain of 3000 is expected with photo-cathode voltage of -11 kV. Actual gain is slightly lower due to the surface layer of the diode.

HAPD uses APD instead of PIN photodiode, and has higher gain due to the gain of APD itself. With an APD of gain 100, HAPD would achieve total gain comparable to PMTs.

Properties of HPDs and HAPDs have been extensively studied so far [18, 19]. Gains of an HPD (Delft PP350F) in and out of magnetic field are shown in Fig. 13.29. The gain in the magnetic field with V_{PC}=-15 kV was measured to be 4000. If we assume the photo-electron yield of EMC to be 260 p.e./GeV, preamp noise to be 1000 e^-, and HPD gain of 4000, we can achieve readout noise of about 1MeV.

Though the gain of HPDs is high enough for calorimetry, it is not high enough for PSD and SMD. We therefore studied performances of HAPDs. The gains of HAPDs were measured for 748-73-75-631 made by Advanced Photonix and for Hamamatsu R7110U in magnetic field. The results are shown in Fig. 13.30. It is clearly seen that HAPDs are operational in a magnetic field with high gain. It was aslo established that HAPDs had sensitivity to measure single photon as shown in Fig. 13.31. Therefore HAPDs can be a good candidate for PSD readout.

Scintillator-strip SMD requires ultra-multi-channel photon detectors. Though once Advanced Photonix made 9-pixel HAPDs, it is not so easy to make multi-pixel HAPDs. Multi-channel HPDs are available with order of 100 channel/device at present. However sensitivity of HPDs are not high enough to use for SMD. Recently developed EBCCDs are ultra-multi-pixel devices naturally, and can achieve single-photon sensitivity [20, 21]. This is thought to be the best candidate for SMD, and basic surveys have been initiated.

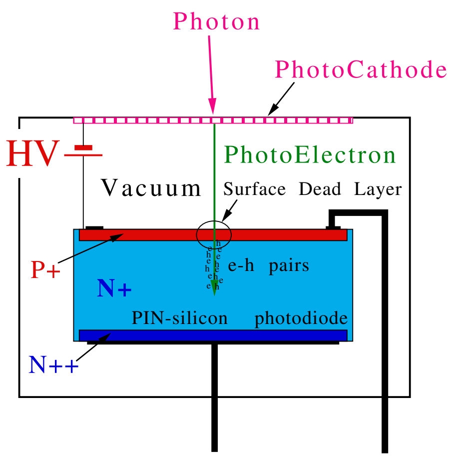

Figure 13.28: Schematic view of the HPD structure.

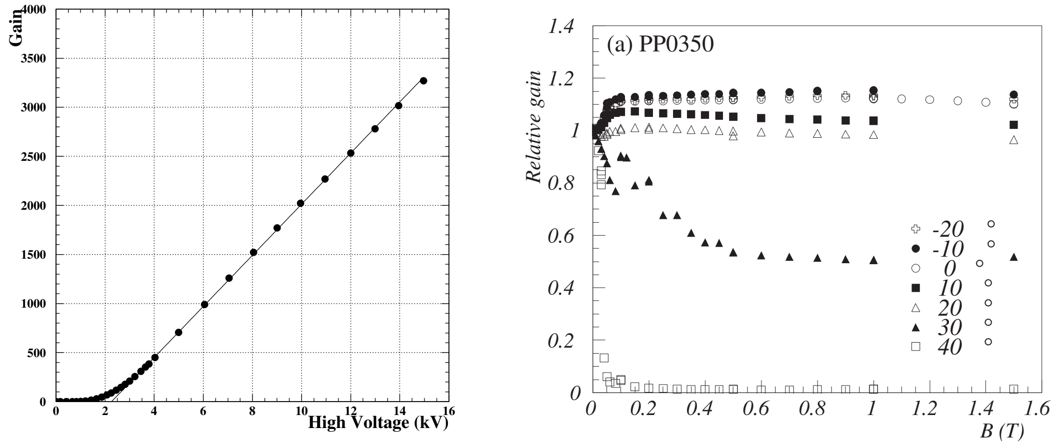

Figure 13.29: Gains of high-gain HPD out of (left) and in (right) a magnetic field.

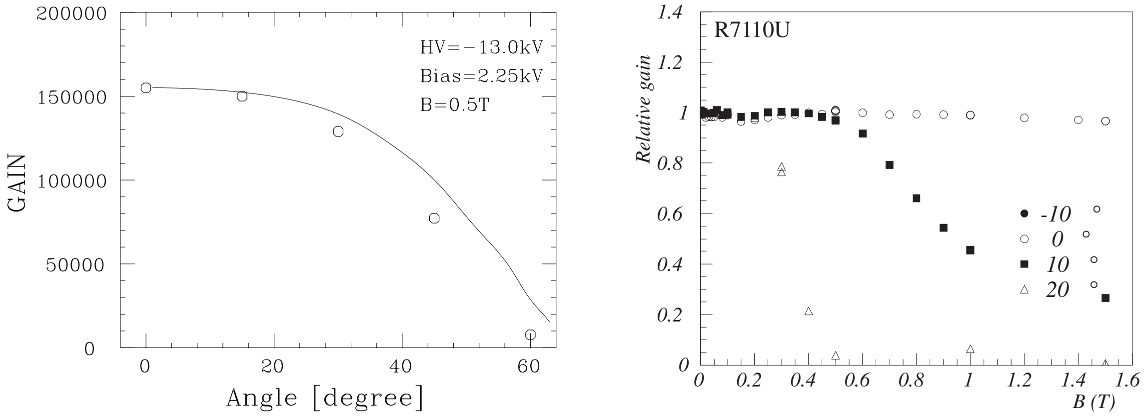

Figure 13.30: HAPD gain in a magnetic field for API 748-73-75-631 (left) and for Hamamatsu R7110U. Solid line in the left figure is result of calculation.

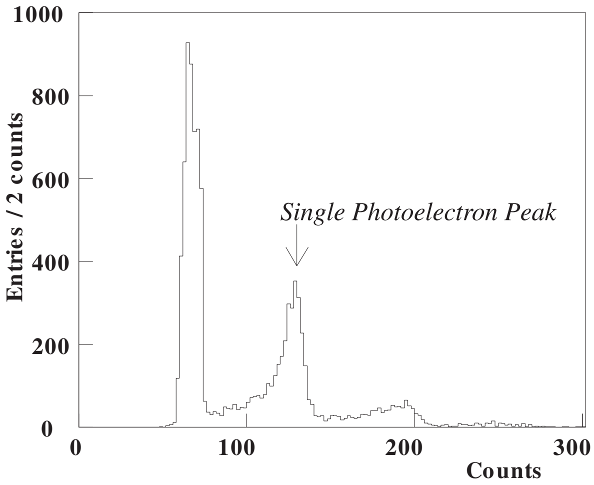

Figure 13.31: Single photo-electron peak measured outside of magnetic field by Hamamatsu R7110U.

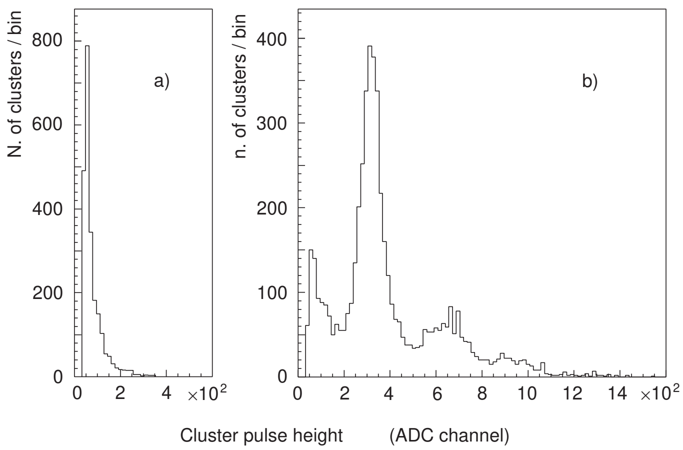

Figure 13.32: Single-photo-electron peak measured with electro-focus EBCCD by RD46.

RD46 collaboration has succeeded to observe single photo-electron peak with an EBCCD as shown in Fig. 13.32. However it is an electro-focus type like image intensifiers, and can not be used in a magnetic field. We therefore started performance study on proximity-focused EBCCDs[20]. Structure of proximity-focused EBCCD is quite similar to that of HPDs shown in Fig. 13.28, replacing PIN silicon photodiode by a CCD. Photo-electrons bombard back-side of CCD, where substrait is thinned to enable photo-electrons to reach to the epitaxial layer. Fiber bundle with appropriate fiber spacing is attached to the photocathode window, and hits are reconstructed by clustering algorithm. Fig. 13.33 shows gain curve with respect to the applied photo-cathode voltage and noise vs. temperatire. Measured sensitivity is yet unable to detect single photon, and further studies are in progress.

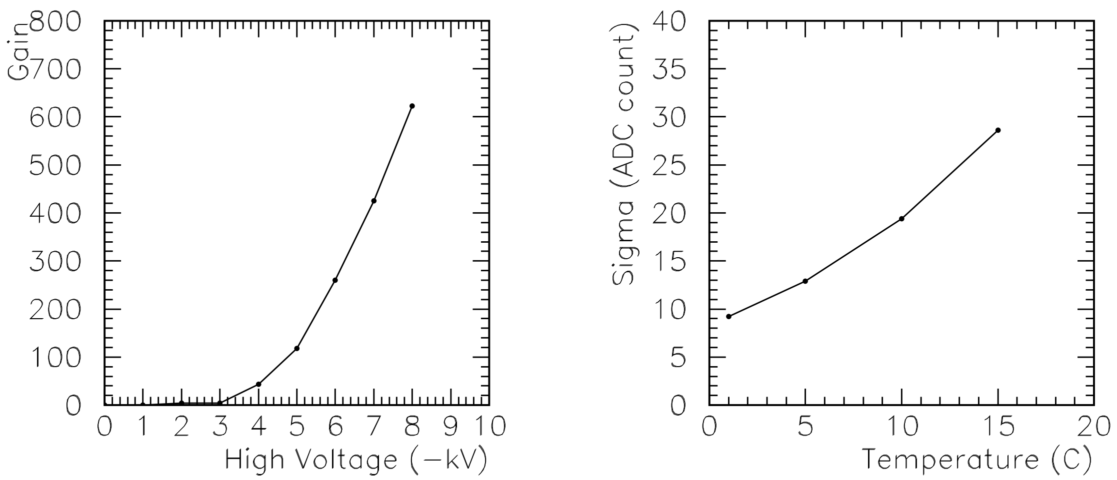

Figure 13.33: Gain vs. photo-cathode voltage (left) and noise vs. temperature (right) for proximity-focused EBCCD N7220.

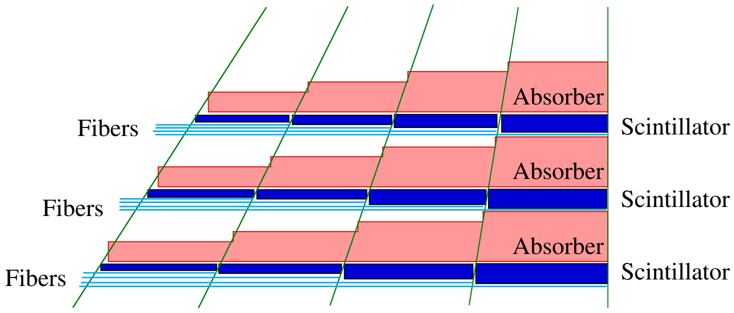

Figure 13.34: Conceptual layout of constant-sampling barrel calorimeter.

13.3.6 Engineering R&Ds

There are several engineering issues related to the actual construction of the calotrimeter system:

- Rigid and strong lead alloy;
- Mass production scheme and cost of tiles;
- Mass production scheme and cost of WLS assembly;
- Overall structure.

Most of these are yet open questions.

Our baseline design is to use lead alloy as absorber material. Test pieces made of Pb(Ca/Sn) alloy of several different concentrations have been made, and measurement of strength, Young's modulus, and creep are to be done soon. Feasibilities of other options such as tungsten, copper, stainless steel or hybrid material such as CFRP-sandwiched lead are yet open questions. However, copper or stainless steel would not be a solution if we stick to the baseline hadron energy resolution.

Machining of σ-grooves on tiles costs about \$10.00/tile for fabrication scale of a few thousand pieces. Since there are 2.2 million tiles in total, machining cost is significant. This can be solved by making tiles with casting. However, casting of tiles with σ-grooves seems very complicated, though is not impossible. On the other hand, the strip EMC option enables quite easy casting. Drastic cost reduction is expected by mega-strip casting ; casting of the strip array as a whole. This possibility should seriously be pursued.

Cost reduction of WLS assemly is totally an open question. Direct readout by attached photo-diode may eable us to avoid this problem.

There are two major ways to build the barrel calorimeter assembly. One is a stack of doughnuts, and the other is an assembly of orange sectors. Orange sector assembly is a natural solution for z-insertion of mega-tiles. In this case, however, absorber plate orientation can not be perpendicular to the polar angle direction. Therefore sampling frequency, and accordingly energy resolution, becomes θ-dependent. One way to avoid this problem is to make a structure as shown in Fig. 13.34. This layout enables constant sampling frequency and at the same time reserving room for clear fibers, which increases as θ increases. However mechanical strength should be a very difficult problem.

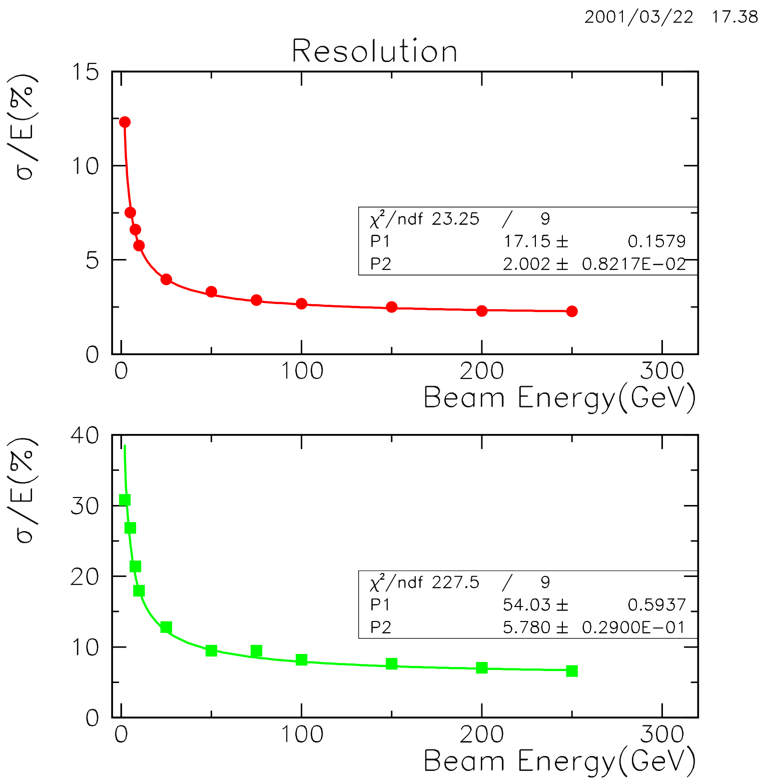

Figure 13.35: Energy resolution of barrel calorimeter implemented in a full simulator. Top is for electrons, and bottom is for pions

13.4 Simulation Study

A full simulator (named JIM) based on GEANT3 was constructed for detector parameter optimization and performance study. Calorimeter geometry and parameters listed in the Table 13.2 are implemented, together with all other detectors and structural components. Calorimeter signal normalization, response mapping, linearity and energy resolution examinations are inprogress, by comparing with the beam test results.

Fig. 13.35 shows full simulation result of the energy resolution of barrel calorimeter for electrons and for pions. Obtained hadron energy resolution of $54\%/\sqrt{E} \oplus 5.8\%$ is much worse than our beam test results shown in Fig. 13.17, and more tuning of detailed geometry and/or cross section of physics processes are necessary.

Response mapping was also done using electrons with respect to the azimuthal angle as shown in Fig. 13.36. We observe a dip in energy measurement at the super-tower boundary. The beamtest data, on the other hand, shows enhancement rather than dip as shown in Fig. 13.20. This difference is considered to be caused by two reasons: 1)tile non-uniformity is not implemented into the full simulator, and 2)there exists unexpected gap between supertowers in the geometry definition. The latter was found by difference of response map between electron injection and positron injection, and should be fixed. Impact of non-uniformity on physics analysis should be investigated to know necessity to implement non-uniformity into the full simulator.

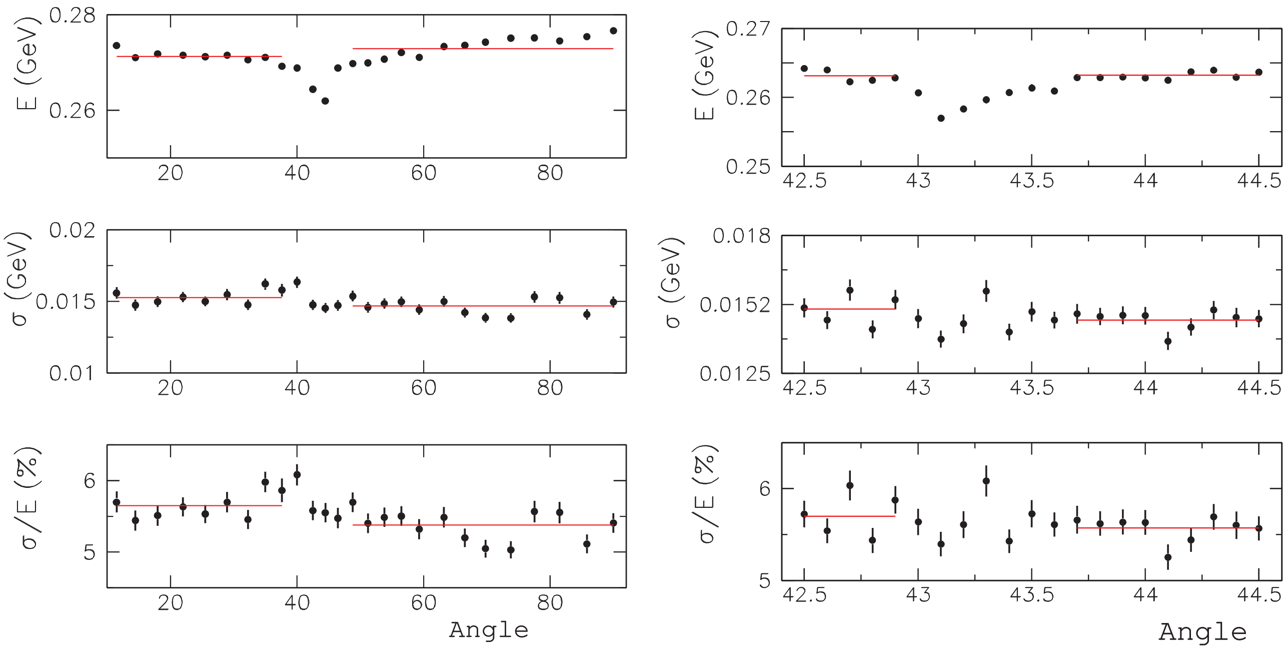

Figure 13.36: Calorimeter response vs azimuthal angle obtained by 10 GeV electron injection. Dips in the left and right figures show boundary between the endcap and barrel calorimeters and boundary between barrel super-towers, respectively.

13.5 Future Prospect

Results of quick simulation for various physics processes have demonstrated that the baseline calorimeter system can realize excellent physics sensitivity. However, validation with a full simulation is essentially important, especially for optimization of granularity. This must be completed urgently.

Extensive hardware studies have proven the technical feasibility and performance of tile/fiber scheme with hardware compensation. There are still open questions in high-granularity EMC option and in photon detector options. These issues are also related to the total cost, and thus should be solved before moving to the proto-type R&D stage. Engineering studies including the heavy metal choice should also be finished before the proto-type stage.

Bibliography

[1] H.P.Wellisch, J.P.Kubenka, H.Oberlack and P.Schacht, MPI-PhE/94-03

[2] E.Bernardi et.al., Nucl.Instr.Meth.A262(1987)229

[3] K.Ishii et.al., Nucl.Instr.Meth.A385(1997)215

[4] SDC Technical Design Report, SDC-92-201, April 1992

[5] The CDF-II Detector Technical Design Report, Fermilab-Pub-96/390-E, November 1996

[6] The Compact Muon Solenoid Technical Proposal, CERN/LHCC 94-38, December 1994

[7] Conceptual Design Report for the Solenoidal Tracker at RHIC, LBL Pub-5347, June 1992

[8] R.Wigmans, Nucl.Instr.Meth.A259(1987)389

[9] D.Acosta et.al., Nucl.Instr.Meth.A308(1991)481

[10] T.Suzuki et.al., Nucl.Instr.Meth.A432(1999)48

[11] G.Drew et.al., Nucl.Instr.Meth.A290(1990)335

[12] H.Miyata, Ph.D. thesis, University of Tsukuba (1984)

[13] S.Uozumi et.al., Submitted toNucl.Instr.Meth.

[14] DESY-ZEUS-Note-91, June 1991

[15] F.Kajino et.al., Nucl.Instr.Meth.A383(1996)260

[16] K.Kawagoe et.al., Submitted toNucl.Instr.Meth.

[17] D.Acosta et.al., Nucl.Instr.Meth.A302(1991)36-46

[18] Y.Fujii et.al., Nucl.Instr.Meth.A366(1995)71

[19] N.Kanaya et.al., Nucl.Instr.Meth.A421(1999)512

[20] S.Suyama et.al., SPIE Vol.3173(1997)422
EB-CCD N7220 Data Sheet, Hamamatsu Photonix Inc.

[21] S.Buontempo et.al., Nucl.Instr.Meth.A413(1998)255

Chapter 14

Muon detector

14.1 Introduction

The muon momentum can be precisely measured by the inner tracking detectors. Therefore the muon detector should only have many position measurements to obtain good matching with the tracks, where modest position resolution is required. Modest timing resolution is also required to reject cosmic ray backgrounds. As the requirements are much looser than those for the LHC experiments, we think that we can construct the muon detector with existing detector technologies. We may apply new technologies developed for LHC if required.

Fig. 14.1 is a cross sectional view of the standard detector, where the muon detector layout is shown. In the barrel region the solenoid magnet is surrounded by one layer of plastic scintillator counters, followed by six muon detector layers; one layer just inside the return yoke, four layers in the return yoke, and one layer just outside the return yoke. The endcap muon detectors have a similar detector configuration. The total area of the muon layers amounts to about 4,000 m^2.

14.2 Material Effect

We studied the effect of the detector material to the muon detector. Table 14.1 summarizes the amount of material of the standard JLC detector in front of the return yoke and in the return yoke itself at $\theta = 90°$. The muon momentum is required to be more than 2.2 GeV to reach the return yoke, and to be more than 5.2 GeV to fully penetrate the return yoke.

Table 14.1: Material thickness of the detector at $\theta = 90°$. Those in front of the return yoke, in the return yoke itself, and the total thickness are listed.

	In front	Return Yoke	Total
Weight	1.09 kg/cm^2	1.51 kg/cm^2	2.60 kg/cm^2
Radiation length	158 X_0	109 X_0	267 X_0
Interaction length	5.6 λ_0	11.2 λ_0	16.8 λ_0

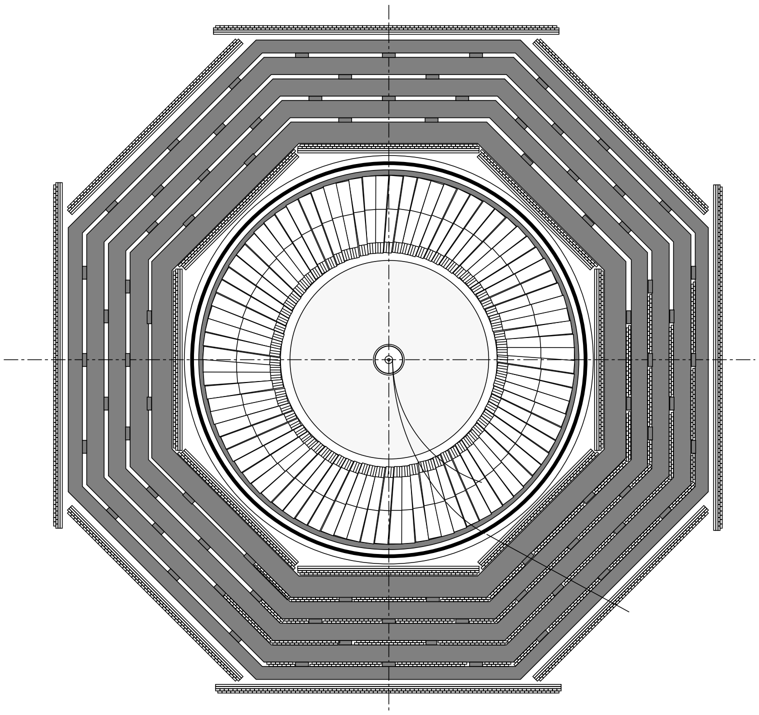

Figure 14.1: Layout of the muon detector.

Multiple scattering due to the material in front of the muon detector is simulated by JIM [2], the full simulation program of the JLC detector. In the simulation, muons are generated at the interaction point with a momentum of $(p_x, 0, 0)$ where the $+z$ direction is along the electron beam. The hit positions at the inner surface of the return yoke ($x = 500$ cm) are recorded.

Fig. 14.2 shows the distributions of the z-coordinate for muons with initial momentum of 5, 10, 20, and 50 GeV. The distributions of the y-coordinate are very similar to those of the z-coordinate. Fig. 14.3(a) shows the standard deviation of the z-coordinate (σ_z) due to multiple scattering as a function of the muon momentum. This result is similar to that obtained for the TESLA detector [3]. Fig. 14.3(b) shows the momentum distribution of muons in the b-quark pair production at $\sqrt{s} = 500$ GeV. As seen in this histogram the majority of muons have momentum below 50 GeV, for which σ_z is larger than 1 cm. We thus conclude that the position resolution of about 1 cm is sufficient for the muon tracking device.

14.3 Detector Options

The JLC muon detector should have position resolution of 1 cm or better, and should be constructed with a well-established technology. In addition, as the muon detector covers a very large area, the technology must be inexpensive. Single-cell drift chambers, resistive plate chambers, and thin gap chambers are currently considered as the candidates.

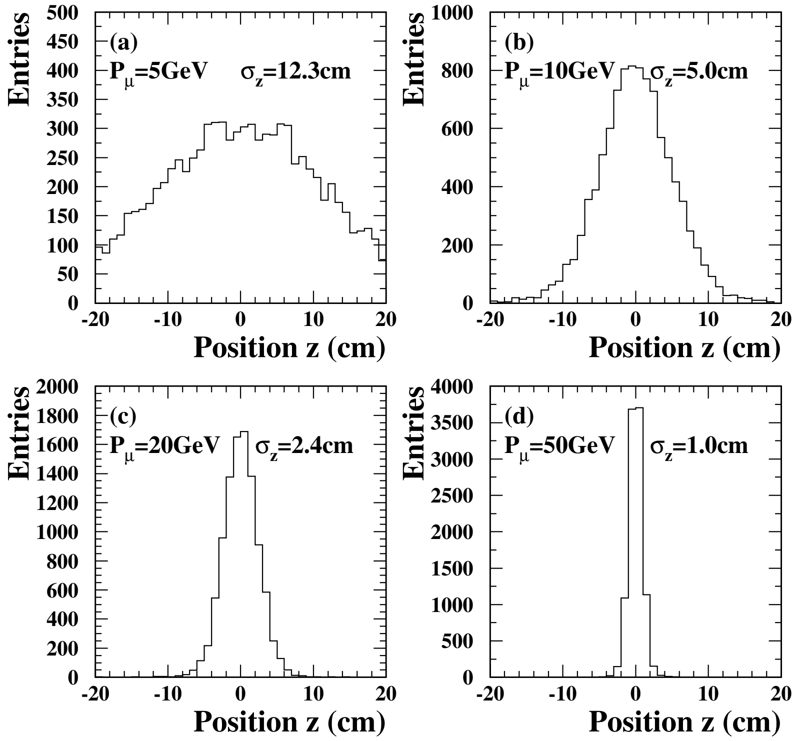

Figure 14.2: Distributions of the z-coordinate at the return yoke surface (a) $p_\mu =$ 5 GeV, (b) $p_\mu = 10$ GeV, (c) $p_\mu = 20$ GeV, and (d) $p_\mu = 50$ GeV.

14.3.1 Single Cell Drift Chambers

The first candidate, single-cell drift chambers (SCDCs), is described in the JLC-I report [1]. A SCDC super-layer has four layers with xx'yy' wire configuration to measure both ϕ and z coordinates. The cell size of the SCDC is 10×5 cm^2, and the wire length is $10 \sim 15$ m. A wire support is located at the middle of the wire to reduce the wire sag. The expected position resolution is about 500 μm dominated by the gravitational wire sag. Once the hit coordinate along the wire is known, the position resolution can be much improved. The number of readout channels is relatively small, about 10,000 in total.

14.3.2 Resistive Plate Chambers

The second candidate is resistive plate chambers (RPCs). Large area RPC systems are used by experiments at B-Factories [4, 5], and will also be used by experiments at LHC [6, 7]. Such a large area RPC system can be constructed with a very low cost, because of their simple structure with no wires. The RPC can be very thin, for example, the total thickness of an RPC doublet for the BELLE KLM detector is only 3.2 cm. The position resolution is determined by the dimensions of readout cathode strips, and a resolution of 1 cm can easily be achieved. RPC is a very promising candidate for the JLC muon detector.

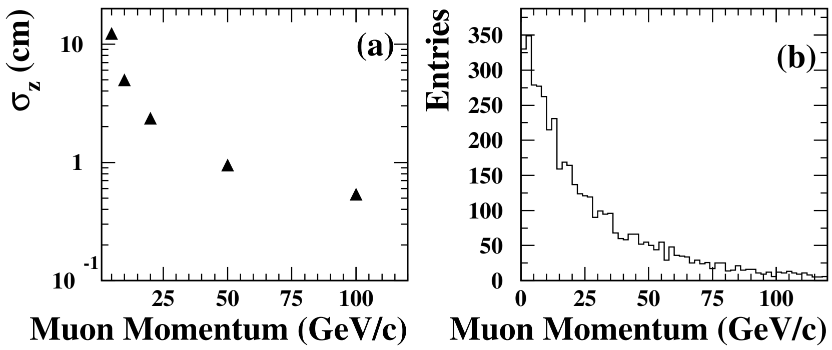

Figure 14.3: (a) The standard deviation of the z-coordinate at the return yoke surface as a function of the muon momentum, and (b) the distribution of the muon momentum in the b-quark pair production at $s = 500$ GeV.

14.3.3 Thin Gap Chambers

The third candidate is thin gap chambers (TGCs), a kind of MWPC with a very thin gap ($\sim$ 3 mm). TGC is highly efficient except for the dead space due to wire supports. The signal is fast enough for our purpose. The position resolution of 1 cm is easily achieved, similar to the case of RPC. TGC can be operational at a very high particle rate of 1 kHz/cm^2. The only demerit is the higher construction cost than that of RPC, as TGC uses a huge number of wires.

The endcap muon trigger system for the ATLAS experiment uses the TGC technology [6]. To this purpose intensive R&D works were performed in Israel and Japan. Production of a total of 1,000 large TGC doublets/triplets are in progress at KEK. According to the ATLAS TGC schedule, the production will be completed in 2003, and then installed at the LHC experimental hall by the end of 2004. Through the TGC production we will at least gain an excellent experience to construct a large area muon detector system.

14.4 Summary

A simulation study is made to investigate the effect of the detector material to the muon detector. The position resolution required for the muon tracking device is found to be about 1 cm.

The detector technology is still to be determined, We have currently three possible candidates for the muon tracking device; single-cell drift chambers, resistive plate chambers, and thin gap chambers. The technology will be determined by further simulation studies, together with experiences obtained at B-factories and LHC.

Bibliography

[1] JLC Group, JLC-I, KEK Report 92-16, December 1992.

[2] URL=http://www-jlc.kek.jp/subg/offl/jim/index-e.html

[3] TESLA Technical Design Report, PART IV A Detector for TESLA, March 2001.

[4] K. Abe *et al.*, IEEE Trans. Nucl. Sci. **45**, 322 (1998);
A. Abashian *et al.* [BELLE Collaboration], Nucl. Instrum. Meth. A **449**, 112 (2000).

[5] F. Anulli *et al.*, Nucl. Instrum. Meth. A **409**, 542 (1998);
P. Paolucci *et al.*, Nucl. Instrum. Meth. A **379**, 472 (1996).

[6] ATLAS Collaboration, ATLAS Muon Spectrometer: Technical Design Report, CERN-LHCC-97-22, June 1997.

[7] CMS Muon Technical Design Report, CERN-LHCC-97-32, December 1997.

Chapter 15

Detector Magnet

15.1 Superconducting coil

15.2 Iron structure

15.2.1 Introduction

An iron structure for the JLC detector has been studied and designed. Figure 15.1 shows the basic configuration of the JLC iron yoke structure. The structure consists of the barrel and two end-yoke sections. The overall height is about 16m from the floor level; the depth is about 13m. The iron structure will be made from low-carbon steel (JIS-S10C: 0.008 0.012 wt% carbon). The total weight except for sub-detectors is approximately 11,000tons, and it will be placed on a transportation system for roll-in/out. Assembling of the iron yoke and installation of the sub-detector will be carried out at the roll-out position and then move to the roll-in position for the experiment. The end-yoke separates at its center and then opens to access to the sub-detectors.

Some kinds of design studies are required to optimize the iron yoke configuration. Those are the influence of the magnetic field, stability against the acted forces such as self-weight of iron yoke (mechanical design) and assembling/maintenance consideration. In the magnetic field study, the iron yoke is acted on the magnetic field of 3T from the JLC solenoid magnet, amount of iron have to be determined for improving the field uniformity in the CDC volume, and leakage field outside of the iron yoke is kept minimize by absorbing the flux return. In the mechanical design, it is required to study on the deformation and stress level against heavy self-weight of iron yoke and strong magnetic force. As the other important issue for the mechanical design, an earthquake resistant design is required. In these studies, way of iron yoke assembling, access to the sub-detectors and cables pass have to be taken into account.

15.2.2 Magnetic Field Design

The criteria for the magnetic design to determine the iron yoke structure are around field uniformity of 1% in the CDC volume, and an allowable leakage field at 10m far from the solenoid center is less than 100 gauss. To set the tolerance against leakage field, an important criterion is to work an electromagnetic valve. With keeping these requirements, thickness of the iron plates were tried to minimize as possible. Permeability of iron plate

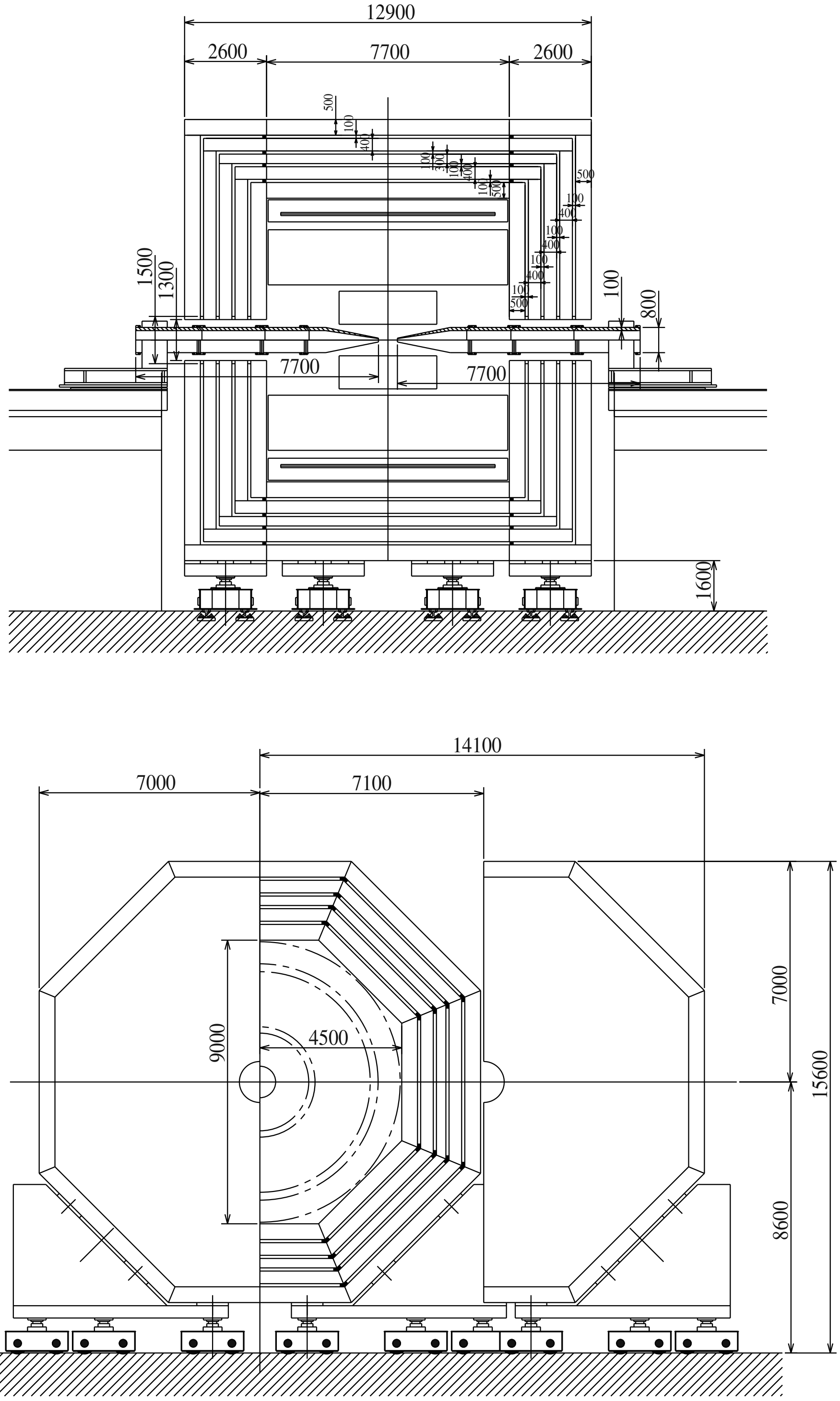

Figure 15.1: Basic configulation of the JLC iron yoke.

for calculation is shown in Fig. 15.2. This is the measurement data of the BELLE iron yoke, which is the same material as the planning JLC iron yoke. The ways to improve the field uniformity without increasing the amount of iron are coil thickness at the end of the solenoid is thicker, and the inner diameter of the end-yoke is smaller. The results of magnetic field calculation when the central magnetic field of 3T is shown in Fig. 15.3. In this calculation, the end part of the coil is two times thicker than the other part. The maximum magnetic field in the iron yoke is to be 3.3T. The field uniformity is to be 1.2% as show in Fig. ??. The magnetic field along the beam line is shown in Fig. 15.5. The leakage field was calculated to be XX.

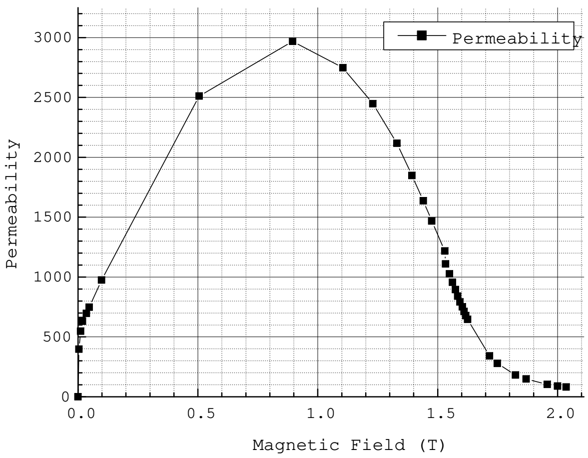

Figure 15.2: Permeability of iron material (JIS-S10C), which was used for the magnetic field calculation.

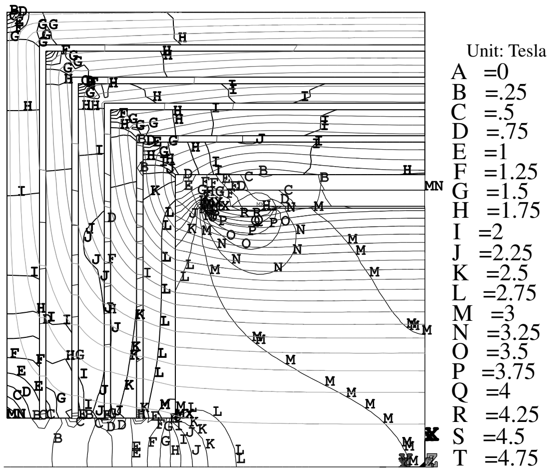

Figure 15.3: Calculated magnetic field at the central magnetic field of B=3 T.

From this calculation, iron plate thicknesses of barrel and end-yoke were optimized. Innermost and outermost layers of yokes are understood to require a thicker iron plate of 50cm-thick than other layers plates of 30cm-thick and 40cm-thick.

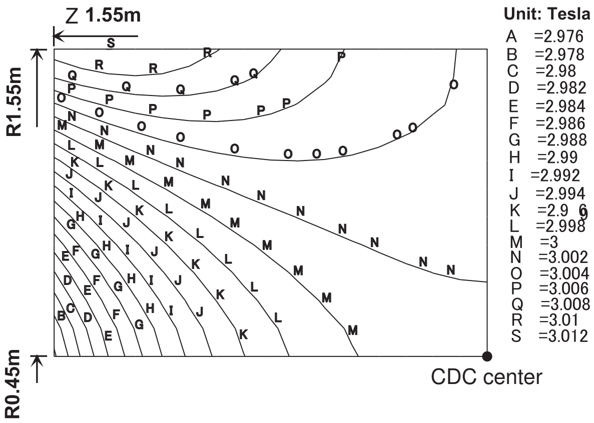

Figure 15.4: Field uniformity in the CDC volume at B=3T. The uniformity is simply calculated from the ratio of the minimum and maximum fields.

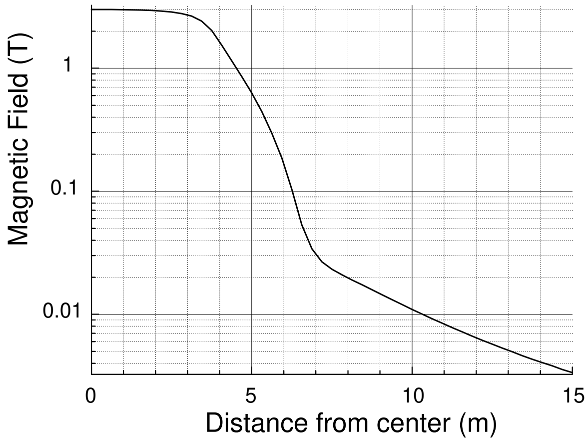

Figure 15.5: The magnetic field along the beam axis at B=3 T.

15.2.3 Mechanical Design

Load conditions of iron yoke are self-weight of 11,000tons. The barrel-yoke is about 5,000 tons and the end-yoke is 6,000 tons, respectively. The magnetic force was calculated to be 18,000 tons. The mechanical design will be followed to the design guideline for construction of nuclear power plant in Japan. In this reference, the safety margins for various stresses are indicated and load conditions are also indicated at the various situations. At the earthquake resistant design, an input acceleration will be 0.2G or 0.3G. Earthquakes of this magnitude are expected to occur in the Tsukuba area with a frequency of once per year of 30 years. Figure 15.6 shows the deformation of the outermost layer of the barrel-yoke due to self-weight. The self-weight of the outermost layer is approximately 1,352 tons. The maximum deformation was calculated to be 3.1mm. However, it should be noticed that this assumption is ideal conditions. The practical situation is each octagonal section will be assembled by bolted joints, so its stiffness must be lower than the complete octagonal shape. It is important to assemble with keeping the rigid structure. The gravitational sag of end-yoke due to the self-weight will be neglected. Because the self-weight is acted on the vertical direction, the end yoke is the rigid body in this direction.

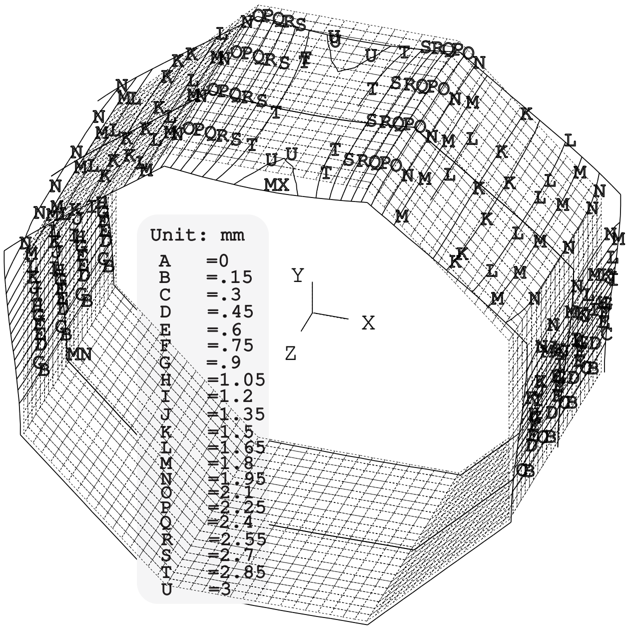

Figure 15.6: Deformation of the outermost layer of the barrel-yoke due to self-weight of 1,352 tons.

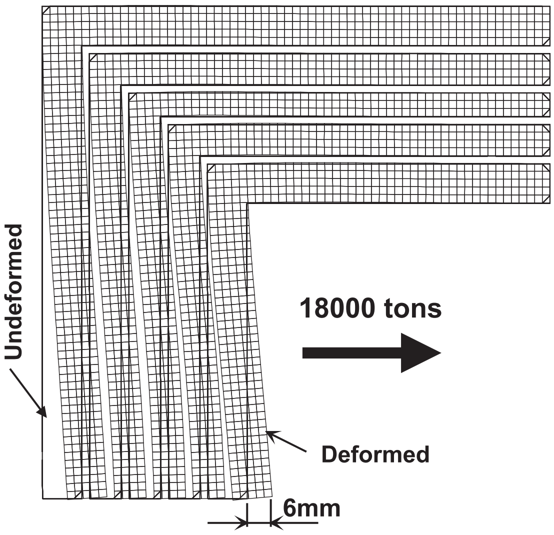

Figure 15.7: Deformation of the end-yoke due to magnetic force of 18,000 tons.

The deformation of the end-yoke due to the magnetic force of 18,000 tons is shown in Fig. 15.7. The maximum deformation was calculated to be 6mm. The end yoke will be assembled from 4 sections from the viewpoint of crane capacity and easy assembling, it will not be able to expect to the stiffness as the completed octagon. At the earthquake resistant design, the natural frequency of iron yoke is calculated as the first step. If this value is lower than the 10Hz, the reinforcement of the iron yoke structure is required due to avoid to resonant with earthquake. As the next step, various earthquake waves those maximum magnitudes are corresponding to 0.2G or 0.3G are input to the iron yoke, then get the responded magnitude. If the magnitude is 0.4G, this value is applied to the horizontal direction as the static load. At the final step, the deformation and stress level will be calculated using 0.4G.

15.2.4 Configurations

The barrel-yoke structure is constructed from eight flux-return and eight Muon detector modules. Each barrel Muon module consists of 5 layers with 100mm thick instrumental gaps. Thicknesses of steel plates are 500mm, 400mm, 300mm, 400mm and 500mm from innermost layer, respectively. Few millimeters of flatness of steel plate has to be taken into account on the Muon detector design. To improve the stiffness of the barrel-yoke, some support structures will be necessary.

Each end-yoke is planned to separate into four quadrants containing five iron plates. Each thickness is the same as the corresponding plate of the barrel-yoke. The inner diameter of 1,300mm is required for th e support tube. The end-yoke must slide out to provide access to the inner detector. An end-yoke transport system has to be studied.